FINAL TECHNICAL REPORT

FOR NASA GRANT NAG3-1501

Entitled

OSCILLATORY/CHAOTIC THERMOCAPILLARY FLOW INDUCED BY RADIANT HEATING

Prepared for

NASA Lewis Research Center
Cleveland, Ohio 44135

by

Principal Investigator: Kenneth J. De Witt
Kenneth J. De Witt
Distinguished University Professor
Department of Chemical Engineering
The University of Toledo
Toledo, Ohio 43606

Submitted January, 1998
for the period
6-1-93 to 11-30-96

THE UNIVERSITY OF TOLEDO

COLLEGE OF ENGINEERING

December 4, 1997

I HEREBY RECOMMEND THAT THE THESIS PREPARED UNDER MY SUPERVISION BY RICHARD M. FUCHS, JR.

ENTITLED OSCILLATORY THERMOCAPILLARY/BUOYANT CONVECTION INDUCED BY RADIANT HEATING

BE ACCEPTED IN PARTIAL FULFILLMENT OF THE REQUIREMENTS FOR THE DEGREE OF MASTER OF SCIENCE IN CHEMICAL ENGINEERING

Kwang-Chung Hsieh Thesis Advisor Kenneth J. DeWitt

Chairman of Discipline Steven E. LeBlanc

Recommendation concurred in

S. Varanasi

K. C. Hsieh

K. J. De Witt

Committee on Final Examination

Oscillatory Thermocapillary/Buoyant Convection Induced by Radiant Heating

by

Richard M. Fuchs, Jr.

Submitted as partial fulfillment of the requirements for
the Master of Science Degree in Chemical Engineering

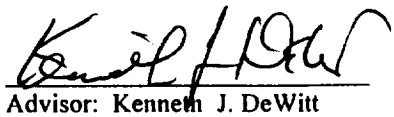

Advisor: Kenneth J. DeWitt

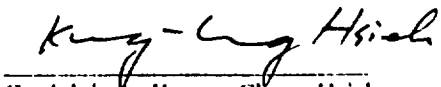

Co-Advisor: Kwang-Chung Hsieh

Graduate School

The University of Toledo
December 1997

An Abstract of

Oscillatory Thermocapillary/Buoyant Convection Induced by Radiant Heating

Richard M. Fuchs, Jr.

Submitted in partial fulfillment of
the requirements for the
Master of Science Degree

The University of Toledo
December, 1997

There is a continuing need to understand the fluid physics occurring under low gravity conditions in processes such as crystal growth, materials processing, and the movement of bubbles or droplets. The fluid flow in such situations is often caused by a gradient in interfacial tension. If a temperature gradient is created due to a heat source, the resulting flow is called thermocapillary flow, a special case of Marangoni Convection. In this study, an experimental investigation was conducted using silicone oil in cylindrical containers with a laser heat source at the free surface. It was desired to determine the conditions under which steady, axisymmetrical thermocapillary flow becomes unstable and oscillatory three-dimensional flow states develop. The critical Marangoni number for each observed oscillatory state was measured as a function of the container aspect ratio and the dynamic Bond number, a measure of buoyant force versus

thermocapillary force. Various oscillatory modes were observed during three-dimensional convection, and chaotic flow was reached in one test condition. The critical Marangoni numbers are compared with those measured in previous studies, and the power spectra and phase trajectories of the instantaneous surface temperature distributions are used to characterize the routes of transitions to the chaotic flow state. Results show that only superharmonic modes appear in the routes to chaos while infinite number of subharmonic modes occur in flow transitions for pure Rayleigh convection.

ii. Acknowledgements

I would like to thank my fiancée Lynn, my parents, and the rest of my family, whose support and encouragement made this long and sometimes difficult journey toward my degree possible. I would also like to thank my advisors Dr. DeWitt and K.C. Hsieh, the University of Toledo Chemical Engineering Department staff, and the people at NASA Lewis Research Center, especially Dave VanZandt, for their expertise, guidance, and assistance with this research.

iii. Table of Contents

iv. List of Tables and Figures

v. Nomenclature

1. Experimental Variables

Cp	Specific heat capacity	$\frac{J}{kg \cdot K}$
D	Test chamber diameter	m
D_b	Laser Beam Diameter	m
g	Gravitational acceleration	$\frac{m}{s^2}$
H	Test chamber height	m
k	Thermal conductivity	$\frac{J}{m \cdot s \cdot K}$
Q	Laser Power	W
R	Test Chamber Radius	m
ΔT	Temperature difference	°C
α	Thermal diffusivity	$\frac{m^2}{s}$
β	Thermal expansion coefficient	$\frac{1}{K}$
γ	Temperature Coefficient of surface tension	$\frac{N}{m \cdot K}$
μ	Dynamic viscosity	$\frac{N \cdot s}{m^2}$
ν	Kinematic viscosity	$\frac{m^2}{s}$
ρ	Density	$\frac{kg}{m^3}$

2. Dimensionless Variables

AR	Aspect Ratio	$\frac{H}{R}$
Bo	Bond Number	$\frac{\rho \cdot g \cdot \beta \cdot H^3}{\gamma \cdot R}$
Br	Beam Ratio	$\frac{D_b}{D}$

Ma_Q	Marangoni number based on Q	$\frac{\gamma \cdot Q \cdot R}{2 \cdot \pi \cdot k \cdot \mu \cdot \alpha \cdot H}$
Ma_t	Marangoni Number based on T	$\frac{\gamma \cdot \Delta T \cdot R}{\mu \cdot \alpha}$
Pr	Prandtl Number	$\frac{C_p \cdot \mu}{k}$
Ra	Rayleigh Number	$\frac{g \cdot \beta \cdot \Delta T \cdot H^3}{\alpha \cdot \nu}$

I. Introduction

Interest in the study of surface tension driven flows has increased in recent years, as researchers have realized the importance of surface tension forces in crystal growth processes and microgravity fluid experimentation. An intense effort is underway to determine when surface tension forces and the resulting flows are important, and to attain a quantitative description of the flow mechanisms involved. By eliminating or reducing surface tension driven forces in crystal melts, the high quality crystals demanded by the industrial sector can be produced. Surface tension driven flows also have a major impact on microgravity fluid experiments performed in space, where fluid flow is mostly unaffected by gravity-induced buoyancy forces, but is dominated by the effects of surface tension. The movement of bubbles or droplets through an immiscible fluid can also be achieved by surface tension driven flows. By gaining a better understanding of this type of flow, scientists hope to gain more control over microgravity fluid experimentation.

Surface tension is a function of the temperature, composition, and electrical potential in a fluid system. A variation in any of these fields along the fluid interface causes a gradient in surface tension, which can induce fluid flow at that interface. Surface tension driven flows are observed in the spread of flames over a pool of liquid fuel, in containerless material processing, and in the movement of an oil droplet in a non-uniform temperature field where surface tension forces are present at the droplet

interface. A surface tension driven flow induced by a temperature gradient is known as thermocapillary flow.

In the case of thermocapillary flow caused by a radiant heat flux, the center of a fluid surface is heated, and the fluid interface at the chamber wall is cooled. An outward heat flux occurs, and the difference in temperatures between the hot center and the cool outer walls causes a surface tension gradient in the fluid, resulting in thermocapillary flow. The surface tension is higher in the cooler regions, as is expected in a liquid system. The hot fluid is then "pulled" outward by the cooler fluid near the walls. As the hot fluid flows away from the center, colder fluid from below flows upward, and the steady flow shown in Figure 1 develops. This steady, axisymmetric flow is known as Marangoni flow.

The steady axisymmetric flow continues until the heat flux reaches a critical value. At and above this critical value, small fluctuations in the flow will grow and eventually form a limit-cycle oscillation. In this way, the flow patterns become oscillatory and three-dimensional. An example of the oscillatory patterns observed at the fluid surface during the experiment can be seen in Figure 2. In the oscillatory flow, the temperature gradient across the fluid surface will oscillate with time, causing surface velocity components in both the radial and circumferential directions. As the fluid oscillates, the free surface also deforms and oscillates, which can have detrimental effects on fluid processes. As the temperature gradient is increased by changing the heat flux, the oscillations in the fluid may change from one organized oscillatory flow pattern to another. At a higher critical value, the flow may develop into a chaotic or aperiodic state.

In the chaotic flow regime, the fluid motion and the free surface shape are random, and the changes in the temperature distribution are non-periodic.

Surface tension driven flows are a major concern in the area of crystal growth technology. The main concerns in crystal growth processes are to minimize contamination, producing a pure and homogeneous product. Containerless processes are frequently used for crystal growth, as the transfer of impurities from the walls is eliminated. Czochralski, floating zone, liquid bridge (half float zone), and open boat zoning growth techniques are different methods of producing crystals. These techniques have a free fluid surface and are susceptible to the detrimental effects of thermocapillary flows. For example, under normal gravitational conditions, surface tension is used to hold the crystal melt between two cylinders in float zones and liquid bridge processes. Because the effect of gravity can cause surface deformations in the melt, these crystal growth processes are performed in microgravity conditions, where minimizing the thermocapillary effects is even more important. When the effect of gravity is decreased during space flight, the effects of buoyancy forces decrease, and surface tension driven flow dominates, adversely affecting crystal growth processes. By reducing surface tension driven flows in the crystal melt, higher quality crystals can be produced under microgravity conditions.

Once thought to be a negligible surface effect, thermocapillary flow dominates crystal growth processes even in a normal gravitational environment. The domination by thermocapillary flows is due to the large surface area to volume ratios and the high temperatures encountered in crystal growth processes. Surface tension driven flows

directly affect the shape of the solid-liquid interface, the growth speed, and the impurity distribution in the crystal melts. Oscillatory thermocapillary flow causes temperature fluctuations in the melts, which in turn leads to oscillatory crystal growth speeds. The unstable growth speeds cause bands of impurities to form in the crystals. Therefore, to improve crystal growth techniques, researchers are searching for ways to control or eliminate the effects of surface tension driven flows in microgravity and normal gravitational settings.

Interest in the capillary motion of bubbles and droplets is resulting in more theoretical investigations of surface tension driven flows, which play an important role in the movement of a droplet or bubble through a host fluid due to a temperature gradient. By imposing a temperature gradient across the liquid medium, surface tension forces develop at the interface between the droplet and the medium. The droplet then travels in the direction of decreasing interfacial tension through the medium. The movement of the droplet is an example of thermocapillary flow, and can be predicted by studying the surface tension forces.

By experimentally determining the critical points at which oscillations and chaotic flow occur, a better understanding of the conditions that cause fluid flow to become unstable is gained. With this understanding, it is then possible to minimize surface tension forces in fluid systems in which instabilities are undesirable, or to use the surface tension forces to control the behavior of fluid interfaces. With the ability to minimize the effects of surface tension driven flows, higher quality crystals can be produced for industrial applications. Reducing the surface tension driving force can also improve

control over fluid experiments during experiments conducted in space. Understanding surface tension can also aid in predicting and controlling the movement of a droplet through an immiscible fluid medium. Although the understanding of surface tension driven flows has many applications in microgravity conditions, research during space flights is difficult to achieve because of the limited availability and the high costs associated with space research. Therefore, it is necessary to conduct thermocapillary experiments under normal gravitational conditions while minimizing the effects of buoyancy, as has been done in this investigation.

II. Historical Notes

1. Early Benard Flow Discoveries

The first observations of surface tension driven flow occurred in 1901, when Benard [1,2] observed hexagonal cells of fluid on a horizontal liquid surface heated from below. This convective flow pattern, which became known as Benard flow, was not immediately attributed to surface tension forces. Rayleigh [3] credited buoyancy forces as the driving factor behind Benard flow, since a vertical temperature gradient was induced in the liquid by heating from below.

It wasn't until 1958 that surface tension forces were suspected as the primary cause of Benard flow. While observing the drying patterns of layers of paint, Pearson [4] noted that Benard cells formed on the liquid paint surface even when the paint covered the underside of a surface. The orientation of the fluid surface in such a case negates any effects from buoyancy while the liquid surface is being cooled by evaporation. From these observations, Pearson concluded that Benard cells could not be caused purely by buoyancy forces.

New properties for Benard flow were examined in 1964, when Scriven and Sternling [5] proposed two modes of instabilities for the flow pattern. The first mode put forth was that of a stationary disturbance steadily increasing over a period of time. The second mode of instability considered for Benard flow exhibited temporal periodicity.

The periodicity of the flow was caused by overstabilization of the fluid system. Scriven and Sternling also proposed four interface models for the fluid free surface. The models proposed were a completely rigid surface, a laterally rigid but flexible surface, a surface that was inflexible but laterally free, and a completely free surface. They also observed that in smaller scale experiments, fluid behavior at the interfaces tended to dominate over the bulk flow behavior.

More work was done in 1964 by Neild [6]. It was Neild's belief that buoyancy and surface tension forces causing instabilities reinforce each other. For buoyancy driven flow, it was known that a critical value existed for a quantity known as the Rayleigh number. The Rayleigh number is defined as follows:

$$Ra = \frac{g \cdot \beta \cdot \Delta T \cdot H^3}{\alpha \cdot \nu} \qquad (1)$$

where g is gravitational acceleration, β is the thermal expansion coefficient, ΔT is the temperature difference, H is the height of the vessel, α is the thermal diffusivity, and ν is the kinematic viscosity. The Rayleigh number is the ratio of buoyancy forces and convective heat transfer to viscous forces and conductive heat transfer for a fluid. Since a critical value existed for the Rayleigh number, it was reasonable to assume that there was also a critical value for the Marangoni number for surface tension driven flows. The Marangoni number is defined as follows:

$$Ma = \frac{\gamma \cdot \Delta T \cdot R}{\mu \cdot \alpha} \qquad (2)$$

In Equation (2), γ is the temperature coefficient of surface tension, R is the radius of the chamber, and μ is the dynamic viscosity. The Marangoni number is a relationship similar

to the Rayleigh number, applying to Benard flow rather than buoyancy driven flows. The Marangoni number is defined as the ratio of surface tension forces and convective heat transfer to viscous forces and conductive heat transfer. Because Neild believed that the two mechanisms driving the flow complimented each other, he proposed that the value of the critical Marangoni number required for Benard flow decreases as the Rayleigh number increases.

The existence of the critical Marangoni number wasn't proven until 1966, when Smith [7] found that by assuming a non-deformable free surface, the critical value could almost always be determined. Smith based his findings on Benard flow for two immiscible liquid phases, each infinitely deep. Assuming a critical Marangoni number and accounting for the effect of gravity, he studied the instability of fluids with steady one-dimensional heat transfer. Smith also discovered that although the effects of surface waves are negligible for most cases, they dominate experiments involving thin layers of viscous fluids.

2. Thermocapillary Flow

The rapid growth of technological industries in the 1970s led to increased interest in crystal growth processes, shifting scientific research away from Benard-Marangoni convection problems. Instead, researchers began to focus on the phenomena related to steady thermocapillary flows often observed in crystal growth melts. Investigators concentrated their experimental and numerical work on proving the existence of surface tension driven flows, the relative magnitude of these flows to those driven by buoyancy

forces, and the interactions of the two driving forces of fluid motion. Others began to investigate the effect of the shape of the free fluid surface on the flow patterns.

In 1976, Chang and Wilcox [8] experimented with floating zone configurations, a common method for crystal growth processes. Attempting to estimate the magnitude of surface tension driven flow, they solved the steady state equations for heat and mass transfer. Part of their work focused on laminar flow regimes for fluids of different Prandtl numbers. They found that the dominant mode of heat transfer for a fluid system can be related to the size of the Prandtl number of the fluid. Convective heat transfer has a relatively minor role for fluids with low Prandtl numbers; however, convection becomes an important heat transfer mechanism for fluids with Prandtl numbers above 1. They also found that buoyancy forces had a negligible effect during their experiment compared to surface tension forces.

Schwabe, Scharmann, Preisser, and Oeder [9] in 1978 were possibly the first investigators to observe thermocapillary flow. They tried to determine the magnitude of surface tension driven flows and to study the oscillatory states in experiments involving $NaNO_3$ float zones. During their investigation, they observed vortex flows in the lower half of the float zones. The flows were inconsistent with the expected flow patterns caused by natural convection. They also observed upper level vortex flows occurring below the critical Rayleigh number for convection. After these phenomena were observed, surface tension forces were eliminated in the setup by confining the melt within a quartz cylinder. Without the effects of surface tension, the vortex flows failed to develop. The flows that had been observed earlier were therefore attributed to a surface

tension driving force. During the experimentation, Schwabe et al. also observed oscillations of temperature and the vortices. The oscillations which were proportional to the temperature gradients across the fluid surface indicated thermocapillary flows present. From this experiment, the researchers proved the existence of thermocapillary flow, and that such flow was not negligible in crystal growth processes. They also proposed that there existed a critical value for the Marangoni number at which oscillatory behavior will begin in a system.

Schwabe and Scharmann [10] continued their experimentation with $NaNO_3$ float zones, and in 1979 proved that there was a critical value of the Marangoni number for the onset of oscillatory flow. They also found that the critical Marangoni number varied for different zone lengths, and concluded that the aspect ratio of the zone was an important parameter in determining flow behavior. They reasoned that by coordinating this with the critical Rayleigh number for the onset of oscillatory natural convection, it would be possible to avoid oscillatory flow by changing the temperature gradient across the fluid and the dimensions of the zone.

Thermocapillary flow was also observed in 1979 by Chun and Wuest [11], who worked with a half float zone process, using methyl alcohol as a test fluid. To explain the oscillatory flow, they credited the behavior of temperature disturbances on the free fluid surface. The growth or damping of the temperature disturbances depends on the ratio of conductive heat transfer to that of Marangoni convection. They found that in cases where there is a high rate of convective heat transfer and low conduction, the temperature disturbances are held relatively steady. In all other cases, however, the temperature

disturbances move in all directions at various rates, interfering with each other. The continuous interference causes the disturbances to amplify over time. Chun and Wuest believed that oscillations also occur as a fluid system attempts to balance the dissipation of energy by viscosity with the rate of energy liberated by surface tension forces. Finally, they observed what they believed to be a growth period for disturbances, occurring between detectable temperature fluctuations and distinct oscillatory motion.

Schwabe and Scharmann [12] again made important contributions to the understanding of thermocapillary flow in 1981, in experiments with an open boat crystal growth experiment. When they covered the free surface of the crystal melt with a thin film of viscous oil, the flow in the melt zone was greatly reduced. In this way, they echoed the findings of Chang and Wilcox in 1976, and proved that thermocapillary flow was a dominant driving force in processes other than float zone configurations.

Investigation into float zone flow patterns continued in 1984, when Kamotani, Ostrach, and Vargas [13] experimented with systems of hexadecane and Fluorinert FC-43. Their work proved that the Marangoni number and aspect ratio alone are not enough to characterize the stability of flow; rather, the flexibility of the free surface and the time lag associated with it are also important in determining flow stability. The time lag is defined as the length of time required for a fluid particle to flow along the surface, travel into the fluid volume, and move back to the surface by means of return flow. They determined that the time lag associated with the free surface flexibility contributes weak and strong periods of convective heat transfer in the fluid. Oscillations are then caused by a combination of factors, including the flexibility and velocity of the surface, and the

temperature distribution across the surface. On a final note, the researchers observed an S-shaped temperature profile on the free surface.

Another set of experiments were conducted in 1984 during a TEXUS 7 rocket flight. Chun [14] investigated a high range of Marangoni numbers, 9.4×10^4 to 1.24×10^5, looking for turbulence. During his experiments, he noted oscillatory and turbulent motion for a variety of flows, and also discovered a transition region between the first noticeable oscillatory motion and fully developed oscillations.

Although crystal melts have relatively low Prandtl numbers, most investigators use fluids with high Prandtl numbers in their experiments because they are easier to use. Many high Prandtl number fluids are transparent, allowing better flow visualization. In 1990, however, Jurisch [15] worked with molten metals having Prandtl numbers below 1. He investigated and observed different modes of oscillations on the fluid surfaces, but saw no S-shaped temperature profiles.

Velten, Schwabe, and Scharmann [16] experimented with high Prandtl number fluids in liquid bridge configurations in 1991. They noted that the critical Marangoni number for oscillatory motion had a strong dependence on the aspect ratio. While studying the modes and frequencies of the oscillations on the surface, they found that thermocouples placed on the surface to record temperatures strongly affected the stability of the flow.

A different experimental method was employed in 1992, when Kamotani, Lee, Ostrach, and Pline [17] investigated flows in circular containers with a wire heater along the axes. They found that the critical temperature difference was independent of chamber

diameters for cases with fixed aspect ratios; therefore, the onset conditions for oscillations could not be specified by the Marangoni number alone. They proposed that a surface deformation parameter, S, be used in addition to the Marangoni number to predict flow stability. The S parameter represents the time lag between flow at the surface and the return flow in the fluid container. They also noted that the flow can be considered to have boundary layer characteristics when the aspect ratio is greater than $Re_\sigma^{-1/2}$, the Reynolds number based on surface tension. The Reynolds number based on surface tension is given by $\frac{\gamma \cdot \Delta T \cdot H}{\mu \cdot \nu}$, where γ is the temperature coefficient of surface tension, ΔT is the temperature difference, μ is the viscosity, ν is the kinematic viscosity, and H is the height of the test chamber. This relationship is derived from a standard form of the Reynolds number, $\frac{V \cdot H}{\nu}$ where V is the velocity, and substituting the relationship $\frac{\gamma \cdot \Delta T}{\mu}$ for V.

In 1993 Lee [18] investigated circular containers filled with 2 and 5 centistoke silicon oil, using a constant heat flux as the driving force. Lee used alpha-alumina particles to allow visualization of the flow patterns, and had thermocouples on the fluid surface for temperature measurement. In addition to the thermocouples, he used an infrared imager to give a complete picture of the temperature distribution on the surface of the fluid. Like previous researchers, he found that the presence of thermocouples at the surface interfered with the flow stability, and that the readings provided by the thermocouples were unreliable. The unreliability of the thermocouple readings occurred because the thermal boundary layer was thinner than the width of the thermocouple

junctions. Lee found that by increasing the ratio of the diameter of the heat source on the fluid surface to the chamber diameter, he could reduce the critical Marangoni number for the onset of oscillations. He concluded that for a given aspect ratio, onset conditions could be predicted from the Marangoni number and the S parameter proposed by Kamotani et al. [17]. For large test chambers, Lee found that the S parameter plays the dominant role in determining flow stability.

More investigations into thermocapillary flow were performed in 1994 by Nash [19]. Nash repeated Lee's method of subjecting circular containers of silicon oil to a radiant heat flux. He determined that there was a definite relationship between the critical Marangoni number and aspect ratio in cases with constant Bond numbers. He also found that the Bond number is an important parameter in thermocapillary flow stability. During his experiment, Nash identified six distinct oscillatory modes, from a simple spinning motion, to complex beating patterns. The oscillatory modes exhibited either radial or tangential periodic motion. Nash also investigated the surface phenomena that occurred at values of the Marangoni number beyond the onset of oscillations. Nash found that as the Marangoni number was increased, the patterns of the surface oscillations changed from one identifiable mode to another.

3. Chaotic Flow Regimes

In addition to examining the onset of oscillatory motion in thermocapillary flow systems, investigators are interested in the fluid behavior after the oscillations have been

initiated. Many of these investigations focus on the transition of surface flow from oscillatory motion to turbulent flow regimes, also known as chaotic flow.

In 1979, Gollub and Benson [20] determined that the flow patterns on a fluid surface changed according to one of four distinct mechanisms during the transition to turbulent flow. In some of the cases, they observed that oscillations of different frequencies became "phase-locked" or entrained. A loss of this entrainment led to the development of non-periodic flow. Another route to turbulence was provided by the successive subharmonic bifurcations of a periodic flow. In a third method, chaotic motion was caused by three incommensurate frequencies coexisting in a well defined flow regime. Lastly, they observed the intermittent turbulence seen by Libchaber and Maurer [21,22] as the behavior of the fluid alternated between periodic and non-periodic cycles. Gollub and Benson also found that the sequence of time dependent instabilities depended on the mean flow of the fluid, and that several mean flows are stable over a wide range of Rayleigh numbers.

In 1984, Wolf, Swift, Swinney, and Vastano [23] developed the first algorithms to estimate non-negative Lyapunov exponents. They believed Lyapunov exponents to be the most useful diagnostic tools for chaotic systems, providing qualitative and quantitative characterization of the fluid behavior. Systems that have one or more positive Lyapunov exponents are chaotic in nature. The group proved that given accurate data about a system, deterministic chaos could be distinguished from external noise and topological complexities.

Chaotic fluid flow was observed in 1994 by Nash [19], while he was investigating the surface behavior of silicon oil past the conditions for the onset of oscillations. Nash observed non-periodic flow once, while investigating surface flow in a small diameter circular chamber, 0.5 cm diameter, with an aspect ratio of 2.0 and 5.88 as the value for the Bond number.

III. Experimental Parameters

In the experiment, a laser beam was used as a source of radiant heat to induce a temperature gradient on the surface of a volume of oil in a chamber with cooled walls, as shown in Figure 3. In such a setup, there are many test condition settings that can be adjusted in order to perform a parameter study of the fluid physics. The researcher is able to change the test chamber shape and dimensions, the cooling bath temperature, or the test fluid used in order to achieve the desired experimental conditions. Even the attributes of the laser are variable -- the ratio of beam diameter to the test chamber diameter, the shape of the beam, and the type of beam can be adjusted. Before beginning the experiment, it is therefore necessary to decide what values or ranges will be studied for each parameter in order to obtain a fluid physics map.

The objective of this experiment was to study the transition from organized oscillatory flow to chaotic motion in circular test chambers with a radiant heat source. The temperature of the test chamber walls was fixed at 20° C, and maintained at this value through the use of a cold water bath. The only fluid used during the experiment was 2 centistoke silicon oil. The laser beam used as the radiant heat source had a Gaussian shape, and a 90° angle of incidence with the fluid surface. The diameter of the beam is non-dimensionalized to give the beam ratio, Br, which is defined as

$$Br = \frac{D_b}{D} \tag{3}$$

where D is the diameter of the test chamber studied and D_b is the diameter of the beam. The effects of varying the beam ratio in thermocapillary flow experiments have been studied by Nash [19], who found that large beam ratios produced a destabilizing effect on the fluid flow. In order to compare the results of this investigation directly with Nash's results, the beam ratio was fixed at a value of 0.2, which was a test condition also used by Nash, throughout the experiment.

The ratio of momentum diffusivity to thermal diffusivity in a fluid is known as the Prandtl number and is expressed by

$$Pr = \frac{C_p \cdot \mu}{k} = \frac{\nu}{\alpha} \tag{4}$$

where C_p is the specific heat capacity, μ is the dynamic viscosity, k is the thermal conductivity, ν is the kinematic viscosity, and α is the thermal diffusivity. Since the only test fluid used in the experiment is 2 centistoke silicon oil, the value for the Prandtl number is fixed at 27 at 25°C. This high Prandtl number means that the rate of viscous diffusion is much greater than that of thermal diffusion in the silicon oil. The Prandtl numbers for fluids in crystal growth processes are generally lower than this value.

The aspect ratio, AR, was used to describe the inner dimensions of the test chambers. Defined as a ratio of the height, H, to the radius, R, of the test vessels,

$$AR = \frac{H}{R} \tag{5}$$

the aspect ratio is an important parameter in determining the stability of thermocapillary flows in a system. The aspect ratio describes the shape of a container. A test chamber with a large aspect ratio has a tall, cylindrical shape, while one with a small aspect ratio is

shaped like a flat dish. The effects of bulk fluid flow are reduced for the flat vessels with small aspect ratios, as the end effects of the system tend to dominate the flow. Therefore, the large surface area to volume ratio of the dish-shaped test chambers exhibit surface tension driven flow rather than flows driven by the effects of buoyancy.

A non-dimensional representation of the temperature gradient across the free fluid surface is given by the Marangoni number based on temperature, Ma_t,

$$Ma_t = \frac{\gamma \cdot \Delta T \cdot R}{\mu \cdot \alpha} \tag{2}$$

where γ is the temperature coefficient of surface tension, R is the test chamber radius, and ΔT is the temperature difference between the center of the fluid and the wall. The Marangoni number also represents the product of two ratios, surface tension forces to viscous forces, and convective to conductive heat transfer in the fluid, as shown by Shen, Neitzel, Jankowski, and Mittlemann [24].

The Marangoni number can be based on laser power rather than the temperature difference. By assuming a fully insulated chamber bottom and then performing an energy balance on the test chamber, temperature change and laser power can be related by $\Delta T = \frac{Q}{2\pi \cdot k \cdot H}$, where Q is the measured laser power. After substituting this into Equation (4), the following relation for the Marangoni number is obtained as

$$Ma_q = \frac{\gamma \cdot Q \cdot R}{2\pi \cdot k \cdot \mu \cdot \alpha \cdot H} \tag{6}$$

Because this experiment was performed under normal gravitational conditions, bouyancy forces caused by gravity still affect the stability of thermocapillary flows. The impact that the buoyant forces will have on the flow patterns can be observed by looking

at the ratio of the Rayleigh number and the Marangoni number based on temperature, which is the ratio of the buoyancy forces to the surface tension forces. This ratio is known as the dynamic Bond number, Bo, and is expressed as

$$Bo = \frac{Ra}{Ma_t} = \frac{\rho \cdot g \cdot \beta \cdot H^3}{\gamma \cdot R} \qquad (7)$$

where β is the thermal expansion coefficient, ρ is the density of the test fluid, and H is the height of the chamber. From this expression, it is clear that the Bond number is directly proportional to the cube of the test chamber height. For shallow test chambers the effects of gravity can become small compared to the surface tension forces, and microgravity conditions can be approximated.

The dimensionless numbers were used as controlled parameters in the experiment. The values for these parameters were chosen to allow thermocapillary flow to be studied in cases with constant aspect ratios as well as cases with constant Bond numbers. The test matrix examined in this experiment is shown in Table 1. The range of parameters used in this experiment are as follows:

1. Test Chamber Diameters used (in centimeters): 0.5, 1.0, 1.2, 2.0, 3.0
2. Constant Aspect Ratios studied: 0.5, 1.0, 1.5, 2.0
3. Constant Bond Numbers studied: 0.13, 0.54, 1.54

This test matrix was studied by Nash [19]; Nash determined relationships between the aspect ratio and the critical Marangoni number, and identified the effects of the dynamic Bond number on the critical Marangoni number in an experiment using a beam ratio of 0.2. Using this test matrix allows the results of this experiment to be compared directly

with Nash's findings. All values in the ranges for Bond numbers and aspect ratios were examined for each test chamber diameter.

IV. Experimental Setup

The purpose of this experiment is to study the fluid physics of thermocapillary flow and the transition from organized oscillatory motion to chaotic motion. Flow is induced in a circular container by subjecting the test fluid to a constant surface heat flux of radiant energy. The radiant energy is provided by a carbon dioxide laser directed normal to the fluid surface, causing a temperature gradient along the fluid surface. A Ronchi imaging system is used to ensure that the fluid surface is level. The top edges of the circular test chamber are treated with a barrier coating to prevent wetting. Thermistors placed at various depths within the walls of the test chamber record the temperature of the fluid at the wall interface. An infrared imaging system is used to observe and record the surface temperature gradient.

After the laser is turned on, the first phase of fluid motion established is steady and two-dimensional. This flow is caused by the surface temperature gradient resulting from the radiant heat source and the cooler chamber walls. As the laser power is increased, the surface flow becomes unstable and three-dimensional oscillatory motion develops. At the onset of the oscillatory motion, the laser power, wall temperature, and center temperature of the fluid are recorded to be analyzed later. The laser power is then again gradually increased, until a different mode of instability or oscillation is observed. Each time a new instability develops, the data are again recorded. This procedure is

repeated until chaotic motion is observed, or until evaporation of the fluid becomes a major factor.

This brief synopsis of the procedure allows the reader to become familiar with the experiment before a detailed explanation of the equipment is given. Rather than introduce the equipment as part of a single system, it is easier to break the setup into five subsystems - the fluid system, the laser system, the thermal imaging system, the free surface deformation system, and the data acquisition system. The following sections will provide greater detail about the components of these systems. The test procedure will be explained in greater detail in the section entitled "Experimental Procedure and Data Acquisition."

1. The Fluid System

The aluminum test chambers used in the experiment are shown in Figure 4. There are five test chambers used in the experiment, having diameters of 0.5, 1.0, 1.2, 2.0, and 3.0 centimeters. The bottom of each test chamber is sealed with an aluminum disc that has been secured in place with model cement to prevent loss of the test fluid. The depth of a chamber is adjusted by stacking Plexiglas discs inside the chamber. Each disc is machined to a specific thickness, and different combinations of the discs are used to produce a range of aspect ratios for that chamber. The discs are slip fit to the chamber diameters, allowing them to be easily added or removed. The thermal conductivity of the aluminum chambers is approximately six times that of the test fluid. The discs provide an insulated base for the chamber, so that the heat is dissipated through the walls of the

chamber, thus preventing axial heat loss. One-sixteenth inch holes are bored through the centers of the aluminum bases and the Plexiglas discs to allow oil to pass through them and into the test chambers. A piece of 1/16 inch stainless steel tubing is cemented into the aluminum base and acts as a feed tube.

The test fluid used in this experiment was 2 centistoke Dow Corning 200 silicone oil, a polydimethylsiloxane polymer. The properties of silicone oil are listed in Table 2. Silicone oil was chosen for many reasons - it is essentially non-toxic, has a low reactivity, is nonbioactive, and is not a threat to the environment. The non-toxicity is especially important during space flights, where safety is a major priority. Silicone oil also has a low rate of evaporation and a relatively flat temperature-viscosity slope. However, one of the most important attributes of silicone oil is its insensitivity to surface contamination. It has been shown that free surface contamination can inhibit thermocapillary flows. In addition, silicone oil is a clear fluid, and is often used in experiments utilizing particle image displacement velocimetry. The frequent use of silicone oil as a test fluid in other investigations, especially the work of Lee [18] and Nash [19], allows for direct comparisons with the results of the current experiment.

The silicone oil used in experimentation was stored in a plastic fluid reservoir. A length of neoprene tubing connected the oil reservoir to the stainless steel feed tube at the base of the test chambers. Oil was forced into the chamber by a piston driven by a large knurled knob on the reservoir. In this way it was possible to exercise a great deal of control over the amount of fluid added to the test chamber from the reservoir. It was also possible to add additional oil during the experiment if small amounts of fluid were being

lost due to evaporation. However, excessive oil loss changes the parameters of the experiment.

The sharp pinning edge at the top of the test chamber is designed to prevent the silicone oil from escaping the chamber. To keep the surface of the fluid flat, a barrier coating is applied to the pinning edge with a small brush. When the coating dries to a transparent film, it prevents wetting, ensuring that the fluid surface is flat. The barrier coating used is Fluorad Surface Modifier FC-723, produced by 3M.

The test chamber is mounted in a circular water bath and secured by 6 screws. A pair of O-rings between the test chamber and the aluminum water bath prevent water leaks from the apparatus, as shown in Figure 3. A GTE Sylvania Model 750 heat exchanger pumps water through the water bath/test chamber assembly at a rate of 57 liters per hour. The residence time of water within the bath is approximately 30 seconds. The cooling water is held at a constant 20° C by means of a temperature dial on the heat exchanger. The water bath apparatus is attached to an adjustable mount on a leveling table. Micrometers on the mount move the water bath assembly in two directions on the horizontal plane. Knurled screws on the underside of the mount allow the assembly to be tilted. In this way, it is possible to position and level the test chamber.

Thermistors mounted within the walls of the test chambers are used to measure the fluid temperature at the wall. The thermistors used are Thermometrics P-20 thermoprobes, having a tolerance of ±1% over the full temperature range. The P-20 thermoprobes have excellent stability at temperatures up to 300° C, which is well above the range encountered during this experiment. The thermistors are individually calibrated

at 10°, 25°, and 100° C. One thermistor is mounted on the outer surface of the test chamber, 0.65 millimeters from the inner wall, as shown in Figure 4. A hole is bored 1 centimeter into the test chamber at a distance of 0.65 millimeters from the inside wall. A second thermistor is placed in the hole at a depth of 5 millimeters, while a third thermistor is also placed in the hole at a depth of 1 centimeter. Before the thermistors are in place, they are coated with a high temperature thermally conductive paste. The thermistor wires are glued to the test chamber surface with model cement several centimeters away from the pinning edge. This positioning of the glue insures that the pinning edge is not insulated. The thermistors are then attached to a signal conditioner.

Most of the equipment used in the experiment is mounted on a pressurized automatic leveling optical table from Newport Corporation, as shown in Figure 5. The table isolates the experiment from most external vibrations and automatically levels itself when additional equipment is added to the table. The heat exchanger is located on the floor rather than on the optical table to prevent unwanted vibrations. Many components of the laser system and free surface deformation systems are also located on the optical table.

2. The Laser System

The laser heating system induces a constant heat flux at the center of the oil surface, as shown in Figure 1. A diagram of the laser system is shown in Figure 6. The beam emanates from a Synrad 25 Watt carbon dioxide laser, which has a maximum power output of 25 Watts. The laser produces a Gaussian shaped beam with a

wavelength of 10.5 to 10.7 microns. The beam diameter is 3.5 millimeters, and the beam divergence is 4 milliradians. Both the beam diameter and the beam divergence are measured at the $1/e^2$ point in the Gaussian beam distribution. At this point, 86% of the laser power is within the measured beam diameter.

An LFS-46-28 power supply by Lambda Electronics powers the laser. The power supply has an output of 28 volts with 5% variance. The laser power is controlled by a Synrad UC-1000 universal laser controller. The controller has settings that allow the operator to run the laser in standby mode, as a closed loop operation, by remote voltage or current control, or in manual mode. During the experiment, the laser controller was set to operate in manual mode, so that the laser power could be adjusted with the power control knob on the front of the Synrad controller. Changes to the laser power using the Synrad controller cause the power to fluctuate for a period of about 15 to 30 minutes, while the laser stabilizes by line-jumping. Therefore, the controller is only used to set the laser power to the maximum level needed for the experiment.

The laser power striking the fluid surface was actually controlled using a model PAZ-15-AC-6 6 plate polarizer-attenuator manufactured by II-IV Incorporated. The attenuator has a transmission rating of 99.0% at 10.6 micrometers, and produces a beam deviation of less than two milliradians at a distance of one meter from the attenuator. The extinction ratio of the polarizer-attenuator is 750:1, also measured at 10.6 micrometers. The attenuator was mounted on an aluminum wall that was attached to the optical table at a 90° angle. The attenuator is operated by rotating the lower section of the apparatus through a 90° path. When the marks on the mobile and stationary parts of the attenuator

are aligned, the attenuator is transmitting 100% of the beam. When the marks are 90° apart, the beam is fully blocked. The polarizer-attenuator is air-cooled, which is the recommended method of cooling for the laser power range being attenuated.

Heat produced by the laser during operation is dissipated by cooling water supplied by a Neslab RTE-111D heat exchanger. This model of heat exchanger is recommended by Synrad for maximum power stability from the laser. The RTE-111D has a cooling capacity of 500 watts at 20° C, and a pumping capacity of 15 liters per minute. The water from the chiller is kept at 20° C, with a variation of only ±0.01° C. This temperature stability is required to prevent the power level of the carbon dioxide beam from fluctuating during the experiment.

After the direction of the carbon dioxide beam is changed by a pair of mirrors, a 90/10 zinc-selenide beam splitter directs 10% of the beam to the detector head of a power meter, while allowing 90% of the beam to be transmitted. In this way, power readings could be taken continuously as the experiment was being conducted. A LabMaster Ultima power meter from Coherent with an LM3 detector head was used to monitor the power of the laser. The LM3 detector head, also manufactured by Coherent Instruments, can measure powers up to 3 watts. Since only 10% of the actual beam was directed to the detector, and the maximum power of the laser is 25 watts, the power striking the head was well within the operating range of the equipment. The detector head was calibrated to an accuracy of ±1%. The liquid crystal display of the LabMaster Ultima system shows the beam position on the detector head, as well as displaying the power striking the detector. The positioning feature on the LabMaster display informed the operator of any

deviations of the laser beam or obstructions in its path. By entering an attenuation factor for the beam, it was possible for the LabMaster Ultima to display the actual power striking the surface of the fluid in the test chamber. Using a second power meter to display the power levels at the surface of the test chamber, the attenuation factor was determined prior to experimentation.

An aluminum beam block is located directly below the 90/10 beam splitter. The aluminum was anodized to prevent beam reflection, and was attached to a mobile mount, allowing the experimenter to swing the beam block into the path of the carbon dioxide beam.

A pair of zinc-selenide lenses are used to focus the carbon dioxide beam to the desired diameter. By changing the distance between the lenses, the operator is able to change the diameter of the beam. The lenses are mounted on a movable platform, controlled by an Oriel motorized micrometer. An Oriel model 18002 controller is used to adjust the micrometer. The resistance of the motor micrometer is measured using a voltage divider, and fed to a conditioning board. Using the calibration curve shown in Figure 7, the beam diameter at the fluid surface is displayed by the Labtech software.

A zinc-selenide beam combiner is located below the movable lenses. The combiner transmits the carbon dioxide beam to the test chamber, while reflecting the helium-neon beam used in the free surface deformation system. The transmittance of the beam combiner is 98.5% according to the manufacturer.

Because of the dangers involved with operating a class IV laser, like the carbon dioxide laser used in this experiment, a number of safety measures must be in place.

Although the safety precautions are not exclusive to this experiment, they are an important aspect of an experiment requiring the presence of a laser. All laser operators must first pass a laser safety training course to become familiar with the hazards and precautions involved with laser operation. A baseline retinal scan performed by a opthamologist is also required of operators. In accordance with laser safety regulations, the doors are equipped with an interlock system connected to the power supply of the laser, regulating entrance to the lab. Safety warnings are posted outside of the laboratory. All personnel within the lab are required to wear protective eyewear when the laser is operating.

3. The Thermal Imaging System

Thermocapillary flow is driven by a constant heat flux, which produces a temperature gradient on the surface of the fluid. In a cylindrical chamber, this gradient is represented by concentric rings of constant temperature. Fluid begins to flow outward from the region of high temperature at the center of the chamber to the cooler walls. This fluid motion is an example of thermocapillary flow. When the flow becomes unstable, the temperature rings deform and begin oscillating. As the power level for the laser is increased, the oscillations change, and eventually progress into chaotic motion. By using an infrared imager to view the surface, it is possible to capture images of the fluid motion at the onset of these instabilities for later analysis.

The infrared imaging was performed using an Inframetrics model 600 infrared imager. The imager scans radiation in the field of view with wavelengths in the 8 to 12

micron range at a scanning rate of 60 Hz. The output rate of the imager is also 60 Hz. The temperature resolution of the imager is 0.1° C at 30° C. The image detector is cooled to 77 K before and during use by an Inframetrics cryocooler. The detector cool-down phase takes several minutes, after which the cryocooler motor slows down to the minimum speed needed to keep the detector at 77 K. Even when the motor is running in the energy conservation mode, however, it produces a tremendous amount of vibrations. Because of these vibrations, the detector is mounted on a nearby lab bench, rather than on the optical table, so that the motor vibrations will not affect the fluid behavior. The detector is attached to a lab jack on the bench, which allows it to be moved up and down to bring the test chamber surface into focus.

To focus on the surface of the fluid, the infrared imager was fitted with a 3x telescope lens and a 6 inch close up lens. A turning mirror at the end of the close up lens reflects the image of the fluid surface into the imager, which is mounted in the horizontal position. The turning mirror was positioned so that the viewing angle is slightly more than 90°, to keep the mirror out of the path of the carbon dioxide beam. During the cooling down period of the detector, the transmissivity of the additional optical components is entered into the setup of the imager controller. It is also necessary to enter the ambient temperature and the emissivity of the test fluid into the setup program. A value of 0.91 was used for the emissivity of the silicon oil, based on the investigation by Pline [25] into the use of infrared imaging systems to measure temperature distributions in 10 centistoke oil. The output from the imager controller is fed to a VCR and then to a color monitor. The VCR is used to record the images of the fluid surface during the

experiment. Using the imager controller, the temperature range displayed in the image can be changed, and different color patterns can be chosen to represent the temperature gradient. The point function on the controller can be used to determine the temperature at the center of the fluid surface.

Figure 8 shows the infrared image of the temperature distribution on the fluid surface during an oscillation.

4. The Free Surface Deformation Imaging System

Because it has been shown in other studies that the stability of thermocapillary flow partly depends on the shape of the fluid's free surface, it is critical that the shape of the fluid surface be known. In the present experiment, the Ronchi technique was used to observe the deformation of the free surface. By using the Ronchi system, the researcher can ensure that the test chamber is completely filled with the test fluid and that the surface of the fluid is flat.

In the Ronchi system used for this experiment, a collimated beam of light is reflected from the fluid surface and directed through a line grating onto a diffuse screen. This process produces a pattern of fringed shadows on the screen. The pattern is a sheared interferogram, also known as a Ronchigram. The relative distances between the shadow lines in the Ronchigram give an indication of the slope of the fluid surface in that direction. Therefore, to get a complete picture of the fluid surface, a grid with both vertical and horizontal lines is needed. The Ronchi system shows the slope of the fluid surface, but not the differences in height along the surface. Although regular

interferometry could be used to give an exact representation of the fluid surface, Meyers and Stahl [26] reported several advantages to using the Ronchi system over interferometry. Because the Ronchi system only measures the slope of the surface, it is relatively insensitive to g-jitter that occurs in microgravity environments. The fringe patterns produced in a Ronchigram are also much clearer than those produced by regular light interferometry, making analysis easier. More deviation in the alignment of optics is also allowed in the Ronchi system. For an interferometer to measure the heights on a fluid surface, the beam of light must be perfectly aligned. After reviewing these considerations, the Ronchi system was chosen as the preferred method to observe the fluid surface for this experiment.

The Ronchi system used in this experiment is shown in Figure 9. The beam of light is provided by a Siemans LGK 20 milliwatt helium-neon laser, with a power supply from the Raytheon Company. The beam produced by the laser is polarized linearly, and has a wavelength of 633 nanometers. The beam is collimated and then expanded by a 30x Galilean type telescope lens. Now that the beam is horizontally polarized, it passes through a cubic beam splitter. The cubic beam splitter is used because it produces less aberration in the beam than other types of splitters. After the beam splitter, the polarization of the beam is changed to right hand circular polarization by a quarter wave plate. The beam is then reflected by a zinc-selenide lens onto the test chamber. The free fluid surface reflects the beam back into its original path. The reflection from the fluid surface changes the polarization from right to left hand circular polarization. When passing back through the quarter wave plate, the reflected beam is changed to vertically

polarized light. Because it is now vertically polarized, the beam is reflected by the beam splitter, and directed toward a polarizing lens and the grating pattern. The polarizing lens improves the reflected image of the fluid surface by removing any ghost reflections from the beam.

After passing through the grating, the reflected beam of light produces a shadow pattern on a screen. The grating is attached to a movable mount between a pair of focusing lenses. In this way, the grating can be moved into the focal point of the lenses, changing the distance between the lines in the shadow pattern. When the grating is placed at the focal point and the fluid surface is flat, the shadow pattern is reduced to a single fringe. The image on the screen is recorded by a video camera, and passed to a video monitor. The display on the screen allows the researcher to observe the free surface of the fluid, and make corrections to the equipment as necessary to keep the fluid surface flat.

5. The Data Acquisition System

The leads from the thermistors mounted in the test chamber walls are attached to channels on a Keithly Metrabyte screw terminal, which passes the signal along to a 5B01 backplane signal conditioner from Analog Devices. The resistance from the motor micrometer is converted to a voltage signal using a 5 volt source and a voltage divider. This signal is passed to a 5B31 Series Module, also from Analog Devices, which is attached to the 5B01 backplane.

The signals from the backplane are then sent to a Keithly Metrabyte DAS-16F 12-bit high speed analog board inside an IBM compatible computer. The signals are processed using Labtech Control version 5.1 for Microsoft Windows. Before the program is used to display the temperatures and beam diameter, programming blocks are set up to convert the raw signals into meaningful data. The thermistor signals are converted to temperatures using the individual calibrations for each thermistor, and the signal from the motor micrometer is converted to the beam diameter using the correlation from the curve in Figure 7.

V. Experimental Procedure and Data Acquisition

1. Preparation

Before any data is collected, several steps need to be taken to ensure that a high degree of accuracy is maintained during the experiment. The stability of the carbon dioxide laser plays a large role in the experiment. When the internal components of the laser are subjected to temperature changes, they are affected by thermal stresses, changing the sizes of the parts. As the components within the laser change, the power output of the laser fluctuates. To minimize the fluctuation of the laser power, it is important to allow the laser to warm up before experimentation begins. First, the heat exchanger which cools the laser is activated, allowing time for the cooling water to reach a temperature of 20° C. The power meter is also turned on, so that laser power can be adjusted as soon as the laser is activated. The polarized attenuator is opened to 100 percent transmittance. After ensuring that a beam block is in the path of the carbon dioxide beam, the laser is armed and activated. The power level of the laser is adjusted to the desired output using the Synrad controller. The laser is then allowed to stabilize for 45 to 60 minutes.

Once a test chamber has been selected, the desired aspect ratio is obtained by placing a stack of clear plastic discs into the chamber to a predetermined depth. The working depth of the chamber is then checked using a digital caliper. After greasing the O-rings in the water bath apparatus, the test chamber is set in place, and the six holding

screws are used to seal the chamber and bath together. The pinning edge and the inside of the chamber are then cleaned with isopropyl alcohol and lint free towels to remove impurities. Compressed air is used to dry the cleaned surfaces, and a barrier coating is carefully applied to the pinning edge of the chamber. The heat exchanger tubing is attached to the water outlet tube on the test chamber, and the water bath heat exchanger is started. Trapped air is bled out of the water bath to ensure good cooling around the walls of the test chamber.

The test chamber is mounted on a moveable base on the air table and secured by a pair of holding screws. A digital protractor is used to measure the level of the test chamber. The screws on the underside of the water bath mount are adjusted until the top of the test chamber is level. Once the chamber is leveled, it is filled with silicon oil from the oil reservoir. The 3x magnification lens is attached to the infrared imager after the chamber is in place, and the imaging system is turned on. The infrared imager must be turned on at least fifteen minutes prior to its use to allow the cryogenic pump to cool the detector to 77 K. Once the infrared lens is in place, the ZnSe beam combiner is placed at a 45° angle above the test chamber. The helium-neon laser used in the Ronchi system and the free surface deformation camera are then activated. The angle and height of the beam combiner are adjusted until a clear picture of the oil surface is shown on the monitors. This image is used to insure that the oil surface is flat. If the surface is not flat, the screws on the water bath mount are again adjusted until the surface is level.

The thermistor wires leading from the test chamber are attached to the appropriate terminals on the signal conditioning board. Because the thermistors are individually

calibrated, the identification number for each thermistor is entered into the Labtech program. Once the thermistor numbers have been entered, the program is run to display the temperatures recorded by the thermistors. If the bath temperature is not 20° Celsius, the setting on the water bath heat exchanger is adjusted accordingly.

A motor micrometer is used to change the distance between the two ZnSe lenses. This distance determines the beam diameter. A plot of the beam diameter versus the internal resistance of the motor micrometer, shown in Figure 7, is used to develop a correlation between the two values. This correlation is then used in Labtech to process the signal obtained from the micrometer, allowing Labtech to display the beam diameter in addition to the water bath temperatures. While Labtech is running, the motor micrometer control unit is used to adjust the carbon dioxide beam to the appropriate diameter.

After the beam diameter is set, the test chamber needs to be centered under the laser beam. Before this can be done, the infrared imager needs to be set up. Once the detector has cooled, the transmissivity of the external optics is set at 0.92, and the ambient temperature and emissivity are set. The desired temperature range and color scheme are then selected. The focus of the imager is changed by adjusting the height of the lab jack upon which it is mounted. Once the imager is ready, it is possible to center the chamber. The attenuator is closed partly to reduce the power of the transmitted beam. The beam block is removed, and the position of the beam is located by watching the infrared image on the television monitor. The micrometers on the water bath mount are

then adjusted until the test chamber is centered under the laser beam. After the beam has been centered, the beam block is again closed until data acquisition is ready to begin.

2. Data Acquisition

After the experimental setup is ready, data acquisition can begin. The Ronchi image is checked to ensure that the fluid surface is level, and that the test chamber is full. Additional oil is added as necessary from the oil reservoir. The polarized attenuator is rotated until the transmitted beam is at the desired initial power level. The beam block is removed from the path of the laser beam, allowing the beam to strike the fluid surface. The infrared image of the fluid surface is displayed on a video monitor, so that the experimenter may observe the surface phenomena. Instabilities in the fluid motion take several minutes to develop, so the infrared image is observed for at least ten minutes before any data collection occurs. If no instabilities develop, the laser power is increased slowly using the attenuator.

However, if oscillations do occur, additional action is taken. The infrared imager is used to display the temperature of the fluid at the center of the chamber. The center temperature and the power level displayed on the power meter are recorded. The infrared image of the fluid surface is recorded in color to videotape, allowing the oscillatory patterns to be easily observed visually at a later date. Using the imager controller, the display is then changed to black and white, and several minutes of the image are recorded for later analysis. While the images are being recorded, the Labtech program is started, recording the side wall temperatures in the chamber during the experiment.

After several minutes of recording the instability, the VCR is stopped. The laser power is then slowly increased with the attenuator, until a different oscillatory pattern is observed. When another pattern develops, all of the data is again recorded. This procedure is repeated until chaotic motion is reached, or until experimental limitations make further investigation for that case impossible. At high powers, evaporation of the oil becomes a noticeable factor, interfering with the behavior of the fluid surface. Also at high powers, surface wave motion of the fluid caused by the instabilities may become violent, spilling oil from the test chamber. In either case, the experiment is stopped, as sudden oil loss changes the parameters of the experiment.

During the experiment, small oil losses occasionally occurred due to evaporation. To counter these losses, small amounts of oil were added gradually from the oil reservoir. The addition of the oil kept the test chamber full and the oil surface level. However, when the evaporative losses became significant, the constant addition of oil to the test chamber changed the behavior of the fluid, and the data acquisition was discontinued.

3. Test Matrix Procedure

Because all other variables are held constant in this investigation, the dynamic Bond number and the aspect ratio are only functions of the chamber diameter and height. When keeping all variables except the height constant in Equations (5) and (6) and inserting the values of silicon oil listed in Table 2, it can be seen that the aspect ratio varies directly with height, while the Bond number varies proportionately to the height cubed:

$$AR = \frac{H}{R} \tag{5}$$

$$Bo = \frac{Ra}{Ma_t} = \frac{\rho \cdot g \cdot \beta \cdot H^3}{\gamma \cdot R} = 11.77 \cdot cm^{-2} \cdot \frac{H^3}{R} \tag{6}$$

The test matrix shown in Table 1 was completed by varying the height and the diameter of the test chamber. To complete the test matrix, a test chamber was chosen, and the height was varied to produce data points for the aspect ratio values of 0.5, 1.0, 1.5, and 2.0. The corresponding dynamic Bond numbers were then calculated for these aspect ratios using Equation 6. This procedure was then repeated for the remaining four test chambers, each having a different diameter.

In the same way, to produce data points at Bond numbers of 0.15, 0.54, and 1.54, a test chamber was chosen and the height was varied until the desired Bond numbers were produced. The corresponding values of the aspect ratio were then calculated for these dynamic Bond numbers using Equation 5. The procedure was again repeated for the other four test chambers.

VI. Results and Discussion

The goal of this work was to experimentally investigate the fluid physics of thermocapillary flow in a cylindrical container as a function of laser power. This included the initial steady two-dimensional motion, the onset of oscillation states, and the eventual transition to chaotic flow. The experimental data are comprised of measurements of the onset of oscillations and the measurements of flow transitions in the phase of post-onset oscillations. The data are then interpreted to describe the fluid behavior as a function of the system parameters and also to study the transition of the flow states in the system.

1. Onset of Oscillations

The critical points for each observed oscillatory mode were determined for the group of test cases listed in Table 1. At these critical points, the power of the laser providing the heat flux and the resulting temperature difference between the center of the fluid and the chamber wall were recorded. An infrared image of the fluid surface was also recorded for several minutes during the oscillation period. The calculated critical Marangoni numbers based on temperature obtained from the experimental data are listed in Tables 3 and 4. These tables show that some of the test cases yielded multiple oscillation states.

The time required for the development of oscillatory flow depended on the size of the test chamber used. Oscillations developed faster when a critical laser power was reached in chambers with small diameters than in the large diameter cases. The oscillations developed faster because the temperature gradient across the fluid surface reached equilibrium faster for the smaller diameter chambers The patterns in the smaller diameter chambers also tended to be more distinct. When the critical power for a new oscillatory pattern was reached in the smaller diameter chambers, one pattern quickly changed into the new pattern. In the larger diameter chambers, however, as the critical power was reached, the surface patterns made a very gradual transition to the new oscillation. The gradual change of the flow pattern in the large diameter chamber made it necessary to wait for a period of time between laser power increases during the experiment. This period of time allowed oscillations to fully develop.

During the experiment, it was also noted that evaporative losses were most noticeable in test cases characterized by a very small fluid volume. These cases occurred when the values for the aspect ratio and the Bond number were low. The evaporation of the test fluid occurs more rapidly in small diameter test chambers, as the small volume of fluid is heated very rapidly. Even with side wall cooling, the average temperature of the fluid increases dramatically. In a case with a large volume, heat is dissipated throughout the fluid, and eventually to the cooling water, resulting in a lower average temperature in the fluid. Data collection was stopped when loss of the test fluid became noticeable. In many of the small diameter cases, the evaporation of the test fluid ended the collection of

data. For larger diameter cases, data collection usually ended when the rapidly oscillating test fluid spilled out of the chamber.

Figure 10 illustrates the effects that changing the Bond number has on the value of the critical Marangoni number at the initial onset of oscillations for cases with fixed aspect ratios. For a given aspect ratio, increasing the dynamic Bond number results in a higher critical Marangoni number, indicating that a higher power is required to induce oscillatory flow. This suggests that buoyancy forces, which are more prevalent at higher dynamic Bond numbers, have a stabilizing effect on the fluid, effectively delaying the onset of flow instabilities. Figure 10 also shows that the critical Marangoni number is more sensitive to changes in the Bond number for small aspect ratios. This trend suggests that there is a critical limit for the aspect ratio, below which the Marangoni number needed to induce oscillations will require a power level that exceeds the parameters of the current experimental setup. In addition, for higher aspect ratios, there seems to be an asymptotic limit of the dynamic Bond number beyond which there us no onset of oscillations.

The dependence of the Marangoni number on the aspect ratio is shown in Figure 11. If the Bond number is held constant, decreasing the aspect ratio results in a high critical Marangoni number required to induce oscillatory motion. There is difficulty inducing oscillations in chambers low aspect ratios, even though the stabilizing effect of buoyancy forces is reduced. In these cases, the return flow to the surface is interrupted by the shallow bottom, which dampens the flow disturbance. The damping of the flow disturbance means that a higher power is required to induce instability in the fluid flow.

Because the critical Marangoni number increases quickly for small aspect ratios, it is possible that a lower limit exists for the aspect ratio, below which the stabilizing effects of the chamber bottom prevent any oscillations from occurring. This would agree with the conclusions drawn from Figure 10. Conversely, the critical Marangoni number for large aspect ratio cases is very low. In high aspect ratio cases, the depth of the fluid allows for fully developed return flow to the fluid surface, as shown in Figure 1. As the aspect ratio is continually increased, the critical Marangoni number also seems to reach a lower asymptotic limit. Below this limit, no oscillations were observed for any value of the Bond number.

The onset conditions for oscillatory flow have been measured previously by Nash [19,27]. The Marangoni numbers that he reported are listed in Table 5. The measurement of onset conditions was repeated in this experiment because of modifications made to the test equipment. The critical Marangoni numbers measured in this investigation were higher than the values that Nash reported, and this difference can be attributed to the different setups. The use of an enclosed cooling jacket around the test chamber maintained consistent side wall temperatures during the present experiment. The open cooling method employed by Nash may not have provided a constant wall temperature for the chamber, allowing the boundary conditions of the experiment to fluctuate. Such fluctuations would encourage the premature development of oscillations. The laser acting as a radiant heat source in the present investigation was also more stable than that used by Nash. An unstable heat source would have reduced the stability of fluid flows by inducing temperature fluctuations at the center of the fluid.

2. Oscillatory Modes

Five distinct oscillatory modes and one chaotic mode were observed during the experiment. These modes are consistent with those observed by Nash [19], which he reported andcharacterized. Nash also observed a sixth oscillatory mode which was not seen during this experiment. The sixth oscillatory mode was described by Nash as a five-lobed pattern which rotated around the center of the fluid. Nash observed the sixth mode while experimenting with a low beam ratio value of 0.05 and a small aspect ratio, 0.3. These conditions were not repeated in the current investigation. For each oscillatory mode observed in this experiment, three frames are presented, representing time elapsed images of the fluid surface. It should be noted that the modes exhibiting tangential motion rotated in both the clockwise and counterclockwise directions at different times during the course of the experiment.

Figure 12 shows Mode A oscillations, frequently referred to as the "swirling" oscillation. The temperature distribution in this mode forms an elliptical shape which rotates about the center of the fluid. The rotation of the elliptical form can occur in both the clockwise and counterclockwise directions. All fluid motion is purely tangential in this mode.

Figure 13 illustrates Mode B, the "twisting" motion. The temperature distribution once again is shaped like an ellipse, as shown in the first frame of Figure 13. The form rotates one direction to the position shown in the second frame, then reverses the

direction of rotation and returns to the original position, shown in the third frame. This oscillation is also comprised of purely tangential motion.

Mode C oscillations are characterized by a "sloshing" motion, as shown in Figure 14. As the oscillation begins to develop, the concentric circles of steady temperature distribution begin to move back and forth across the fluid surface along a single line of motion. The sloshing form is compressed and deformed at the walls of the chamber.

The fourth mode observed was Mode D, shown in Figure 15. As the fluid oscillates, it seems to possess a "beating" motion. The temperature distribution forms an ellipse, which shrinks down along its major axis toward the center of the chamber. As the first ellipse is shrinking, a second ellipse expands from the center of the chamber along a line perpendicular to the major axis of the first. The pattern then repeats, with the two ellipses alternately pulsing out from the center. When the ellipses encounter the chamber walls, the temperature distribution is deformed, causing the "hourglass" shape shown in Figure 15.

The final type of oscillatory motion observed in this investigation is shown in Figure 16. This pattern, the Mode E oscillation possess a three-lobed temperature distribution. The lobes either pulse like Mode D or rotate quickly about the center of the fluid. The speed of the oscillation makes it difficult to discern by which mechanism the pattern is moving.

In the following analysis, it is desired to find out if the route of the flow transitions is different from that occurring in pure Rayleigh convection which is buoyancy driven. While the transitions in Rayleigh convection involve an infinite

number of subharmonic modes, it is suspected that the transitions in combined thermocapillary and buoyant convection contain only superharmonic modes and no subharmonic modes. It is a conjecture that the property of the energy cascade in fully turbulent flow is also modified when thermocapillarity is significant in the flow configuration. Based on these findings the following discussion of the experimental results will be aimed at answering the critical questions listed below:

1. What are the characteristics of the Hopf bifurcation from the steady to the oscillatory state?
2. What is the route of the flow transitions from organized oscillations to chaos?
3. What are the characteristics of the power spectra and the phase trajectories at various transitional stages as functions of thermocapillarity and buoyancy?

3. Analysis of the Instabilities

Using the fluid surface temperature at the side walls and at the center of the fluid surface from the infrared images collected, the temperature gradient along the fluid surface was calculated. Before data analysis began, the infrared images of the fluid surface were transferred from videotape to laser disc. The laser disc provides immediate access to individual frames, making analysis of the video much more efficient.

The Tracker program for Windows was used to measure the gray scale at various points on the black and white surface image. The gray level at a point is a direct representation of the temperature at that point on the image. Twenty equidistant points on the fluid surface were selected for analysis. The points were located on a common

radius around the center of the test chamber. The Tracker program measured the gray scale intensity at these points for a large number of frames. By analyzing the gray scale representations of these temperatures from the infrared image, the behavior of the temperature oscillation at the surface could be observed.

The flow transitions were studied using power spectra and phase trajectories. There are other tools available for the investigation of the transitions of flow from organized oscillations to chaos, such as the bi-orthogonal decomposition (BOD) method [28], autocorrelation functions, and Lyapunov exponents. Due to time limitations for the present investigation, only the power spectra and the phase trajectories will be used to analyze the results.

3.1 Power Spectra

Using the temperature data obtained from the infrared imager, power spectra were plotted for each oscillatory pattern observed. The power spectrum for an oscillation is generated by performing a Fast Fourier Transform on a time history of a surface temperature at a fixed location. The power spectrums provide a number of important facts about the surface phenomena, including the frequency of the oscillatory motion, identification of oscillations caused by spinning or standing waves, and the intensity of each oscillatory mode. Power spectra can also be used as an indication of chaotic flow. As the flow pattern in a system approaches chaotic flow, the power spectra show increasing numbers of harmonic modes. The bases of the spikes representing the modes gradually widen as chaotic flow is approached, eventually forming a continuous pattern.

Another important characteristic of a typical power spectrum for chaos is that the continuous spectrum decays exponentially with respect to frequency.

The identification of an oscillatory mode is accomplished through the Fourier transformation of the time history of the infrared image of the oscillation. For a typical spinning sinusoidal wave with a single frequency at a fixed radial coordinate, the wave form is represented by:

$$\sin(\omega \cdot t - \alpha \cdot \theta) \tag{7}$$

where ω is the frequency, α is the wave number, and θ is the coordinate in the azimuthal direction. Conversely, for a typical standing sinusoidal wave with a single frequency at a fixed radial coordinate, the waveform is represented as:

$$\sin(\omega \cdot t) \cdot \sin(\alpha \cdot \theta) \tag{8}$$

When a Fourier transformation from the time domain to the frequency domain is performed on the waveform in Equations 7 and 8 at various angles θ, the spinning and standing modes can easily be distinguished. For a spinning wave, the spikes on the power spectra will have the same height at various angles; for a standing wave, the spikes will vary significantly. Using Figure 19 as an example, the spikes at different phase angles have the same height, indicating that the oscillation contains a spinning wave.

Before further explanation of the experimental data is given, the method of labeling oscillations must be presented. For each test case in the experiment, the laser power was increased until oscillatory motion was observed. Two minutes of oscillations were recorded, and the laser power was again increased. Another two minutes of oscillations were recorded when the pattern changed. This process was repeated until the

loss of test fluid due to evaporation or spills caused by vigorous fluid motion became noticeable. The initial oscillation recorded is termed the "first oscillation," with the second pattern being named the "second oscillation" and so forth. Analysis of the first oscillation yielded no spikes in the corresponding power spectrum. The lack of power spectrum spikes in these cases suggests that the first observed oscillations of the fluid surface were not fully developed oscillations, but were the first step in the transition to fully developed flow described by Chun [14]. Therefore, analysis of the collected data begins with the second observed oscillatory pattern, where it is believed that fully developed oscillations first appear.

Figures 17 and 18 show the modes of the second and third oscillations for all of the constant aspect ratio cases. In general, spinning waves occur when both the aspect ratio and the the bond number are low. It also seems that the regime of standing waves is bounded by the modes with a combination of standing and spinning waves. Beyond the boundary of the combined modes, spinning waves occur. Presently, there is no theory or physical model to explain these observations. Further study is needed to understand the fundamental mechanisms of the cause of this behavior.

Figure 19 shows the power spectra of the second oscillation of the test case with an aspect ratio of 1 and a Bond number of 2.94. The images from the infrared camera were digitized at r/R=0.25 (r is the radial coordinate and R is the chamber diameter) at three different phase angles. As can be seen in the power spectra, single dominant frequency exists at 0.93 Hz. Figures 20 through 24 show the power spectra for five consecutive stages of flow transition following the second oscillation. The power

spectrum clearly evolves when the state of oscillatory flow changes, In the fifth oscillation, shown in Figure 22, two superharmonic modes appear. This indicates an energy transfer from the first to higher harmonic modes. The spectrum becomes wide and loses the characteristics of organized oscillations in the sixth and seventh oscillations. As opposed to the characteristics of flow transitions for forced convection over a wavy wall [29,30] and natural convection in an enclosure [31,32] which involve an infinite number of subharmonic modes, the transitions in combined thermocapillary and buoyant convection contain no subharmonic modes but only superharmonic modes.

In the path to chaotic flow, the power spectra usually show increasing harmonic modes with the bases of the spikes widening to eventually form a continuous pattern. It can be seen that base widening started to occur in the fourth oscillation and that multiple spikes exist in the fifth sixth, and seventh oscillations. This indicates that the flow structures have undergone a series of transitions toward the chaotic state.

Another important characteristic of a typical power spectrum for chaos is that the continuous spectrum decays exponentially with respect to frequency. This pattern was not observed in the present set of data. Therefore, the flow state has not yet reached the chaotic state.

The dynamic Bond number for the case discussed above was 2.94, which indicates that there is a significant buoyancy effect. To limit the buoyancy effect, it is desirable to acquire data for a low Bond number case. In a ground-based experiment, this translates into using a small test chamber, which has the problem of strong oil

evaporation and thus allows investigation of only a limited range of laser powers (Marangoni numbers).

The power spectra for another case, aspect ratio of 0.5 and Bond number equal to 3.31, is included due to its peculiar characteristics. Immediately after the onset of oscillation, there exist two harmonic modes in the power spectra shown in Figure 25. One is a spinning mode and the other is a standing mode. Furthermore, the bases of the spikes are already fairly wide. This could imply that the flow structure is quickly approaching a chaotic state. However, in the higher transitions shown in Figures 26 and 27, no superharmonic modes can be observed. The question of whether it is possible for neither superharmonic nor subharmonic modes to occur when the flow structure undergoes a series of transitions to the chaotic state remains. System parameters that might characterize this phenomenon are also unknown.

3.2 Phase Trajectories

A phase trajectory is another useful tool to analyze oscillations. A phase trajectory is constructed by plotting the time history of the gray level of an infrared image at a specific point against the time history of the gray level at the same point but with a time lag. The periodic state, quasi-periodic, and aperiodic states can be clearly observed when phase trajectory is plotted. With further analysis, the number of dimensions of the strange attractors on a phase plot can be obtained. A strange attractor can be defined as a group of interconnected loops which have indefinite paths embedded for a particle to travel. For the test case discussed in the previous subsection with an aspect ratio equal to 1 and a Bond number of 2.94, the flow transitions involving periodic, quasi-periodic, and

chaotic modes can be observed in phase-trajectory plots as shown in Figures 28A through F. For a sinusoidal function with a single frequency such as Figure 19, the phase trajectory follows a simple loop in a circular or elliptical shape as shown in Fig. 28A. In Figures 28B through F, the phase trajectories become complicated strange attractors and have multiple loops. Specifically, in Figure 28F there are two main branches of loops which indicate the existence of a quasi-periodic state.

In the test case with the dynamic Bond number of 3.31 and an aspect ratio of 0.5, the phase trajectories are shown in Figures 29A through C. As implied in the corresponding power spectra shown in Figures 25 through 27, the multiple branches of trajectories could not appear since the number of harmonic modes did not increase from the second to the fourth oscillation. It is worthwhile to note that the data for the phase trajectory plots have been preprocessed with a narrow-band filter. The filtering process minimizes the effects of experimental noise. Without the narrow-band filter, the phase trajectories become very blurry, as shown in Figures 30A through C. Care must be taken to avoid over-filtering and distorting the critical characteristics of the oscillation mode.

4. The Chaotic Flow Regime

Although a large number of cases were investigated, chaotic flow was only observed for a single set of parameters. Random flow developed in the 0.5 cm test chamber during tests with the aspect ratio of the chamber set at 2.0. The Bond number for this setting is 5.88. Nash [19] also observed chaotic flow for these conditions in 1994. Infrared images of the flow surface for this set of test parameters are shown in Figure 31.

The power spectrum of the first fully developed oscillatory pattern for this case is shown in Figure 32. Similar to the case with a two harmonic modes appear in the power spectrum immediately after the onset of oscillations. Both are standing waves, and the spike associated with the lower frequency is shorter than that associated with the higher frequency. Higher transitions are shown in Figures 33 through 36. Laser reflections from the fluid surface created anomalies on the infrared images of the surface during data collection for the third observed oscillation. The unusual shape of the power spectrum for this pattern (Figure 33) proves that the surface data was distorted in this case. The fourth oscillation, Figure 34, has no unusual interference, and shows the addition of other modes of oscillation to the pattern. The increased background noise, the widening of the peak bases, and the overall choppy shape of the peaks in Figure 35 is an indication that the oscillatory pattern observed is nearing non-periodic flow. The sixth oscillation, shown in Figure 36, has power spectra that are close to a continuous pattern, indicating that the flow is nearly chaotic. This characteristic can be further confirmed in the phase trajectories generated from the data.

The phase trajectories in Figure 37 provide an clear picture of the transition of the flow structure from organized oscillatory flow (Figure 37A) through increasingly complex patterns achieving quasi-periodicity (Figure 37D) to chaotic behavior (Figure 37E). This was the only set of test parameters from Table 1 that exhibited near-chaos behavior.

For future work related to the current investigation, the experimental system will be modified to extend the operating range. The test cell will be capped and pressurized

so that the evaporation rate of the silicone oil will be reduced. The silicone oil will be distilled to separate and remove highly volatile components. The distillation process will also reduce the evaporation rate of the oil.

VII. Conclusions and Recommendations

The goals of this experiment were to investigate the oscillatory flow regimes that resulted from a combined thermocapillary and buoyant convection, and to characterize the oscillatory states leading to the transition to chaos.

For the range of aspect ratios and dynamic Bond numbers selected in this experiment up to five oscillatory modes were observed, which agreed qualitatively with previous measurements by Nash [19]. However, the critical Marangoni numbers were slightly lower due to refinements of the experimental apparatus. Among all test cases, only one condition gave rise to a fully developed chaotic flow.

The experimental results were analyzed using power spectra and phase trajectory plots of the observed oscillatory surface temperatures. It has been observed that in all test cases, the flow structures undergo a series of flow transitions and reach quasi-periodic or chaotic states when the limit of the experimental system is approached. The most significant finding is that while the transitions in Rayleigh convection involve an infinite number of subharmonic modes, the transitions in combined thermocapillary and buoyant convection contain no subharmonic but only superharmonic modes. In addition, there are certain cases in which two fundamental modes appear immediately after the onset of oscillation. Quite often one is a spinning mode and the other is a standing mode.

There are two factors limiting the range of laser power for heating the silicone oil. One is that evaporation rate becomes too strong when high laser power is reached. The

other one is that the oil spills over the pinning edge due to strong surface waves when the laser power is too high. The potential remedies are to enclose the top of the test cell and run the experiments with elevated pressure and to triple distill the silicone oil. These two steps could reduce the evaporation rate of the silicone oil and thus provide a wider test range in the future.

VIII. References

1. H. Benard, "Les Tourbillons Cellulaires dans une Nappe Liquide", Rev. Gen. Sciences Pure Appl., *11*, pg. 1261, 1309 (1900).

2. H. Benard, "Les Tourbillons Cellulaires dans une Nappe Liquide Transportant de la Chaleur par Convection en Regime Permanent", Ann. Chim. Phys., *23*, pg. 62 (1901).

3. L. Rayleigh, "On Convective Currents in a Horizontal Layer of Fluid When the Higher Temperature is on the Under Side", Phil. Mag., *32*, pg. 529 (1916).

4. J.R.A. Pearson, "On Convection Cells Induced by Surface Tension", J. Fluid Mech., *4*, pg. 489 (1958).

5. L.E. Scriven and C.V. Sternling, "On Cellular Convection Driven by Surface-Tension Gradients: Effects of Mean Surface Tension and Surface Viscosity", J. Fluid Mech., *19*, pg. 321 (1964).

6. D.A. Neild, "Surface Tension and Buoyancy Effects in Cellular Convection", J. Fluid Mech., *19*, pg. 341 (1964).

7. K.A. Smith, "On Convection Instability Induced by Surface-Tension Gradients", Int. J. Heat and Mass Trans., *22*, pg. 535 (1966).

8. C.E. Chang and W.R. Wilcox, "Analysis of Surface Tension Driven Flow in Floating Zone Melting", Int. J. Heat and Mass Trans., *19*, pg. 355 (1976).

9. D. Schwabe, A. Scharmann, F. Preisser, and R. Oeder, "Surface Tension Driven Flow in Floating Zone Melting", J. Crystal Growth, *43*, pg. 305 (1978).

10. D. Schwabe and A. Scharmann, "Some Evidence for the Existence and Magnitude of a Critical Marangoni Number for the Onset of Oscillatory Flow in Crystal Growth Melts", J. Crystal Growth, *46*, pg. 125 (1979).

11. C.H. Chun and W. Wuest, "Experiments on the Transition from Steady to Oscillatory Marangoni Convection in a Floating Zone Under Reduced Gravity Effect", Acta Astronautica, *6*, pg. 1073 (1979).

12. D. Schwabe and A. Scharmann, "Marangoni Number in Open Boat and Crucible", J. Crystal Growth, *52*, pg. 435 (1981).

13. Y. Kamotani, S. Ostrach, and M. Vargas, "Oscillatory Thermocapillary Convection in a Simulated Floating-Zone Configuration", J. Crystal Growth, *66*, pg. 83 (1984).

14. C.H. Chun, "Verification of Turbulence Developing from the Oscillatory Marangoni Convection in a Liquid Column", European Space Agency SP-*222*, pg. 271 (1984).

15. M. Jurisch, "Surface Temperature Oscillation of a Floating Zone Resulting from Oscillatory Thermocapillary Convection", J. Crystal Growth, *102*, pg. 223 (1990).

16. R. Velten, D. Schwabe, and A. Scharmann, "The Periodic Instability of Thermocapillary Convection in Cylindrical Liquid Bridges", Physics of Fluids, *A3*, pg. 267 (1991).

17. Y. Kamotani, J.H. Lee, S. Ostrach, and A. Pline, "An Experimental Study of Oscillatory Thermocapillary Convection in Cylindrical Containers", Physics of Fluids, *A4*, pg. 955 (1992).

18. J.H. Lee, "A Study of Oscillatory Thermocapillary Convection in Circular Containers with CO_2 Laser Heating", Ph.D. Thesis, Dept. of Mech. and Aerospace Eng., Case Western Reserve University, Cleveland, Ohio (1993).

19. J. Nash, "An Experimental Study of Thermocapillary Flow in Circular Containers with a Radiant Heat Flux", Master of Science Thesis, Mech. Eng. Dept., The University of Toledo, Toledo, Ohio (1994).

20. J.P. Gollub and S.V. Benson, "Many Routes to Turbulent Convection", J. Fluid Mech., *100* , pg. 449 (1980).

21. A. Libchaber and J. Maurer, "Local Probe in a Rayleigh-Benard Experiment in Liquid Helium", J. Phys. Lett., *39* , L369 (1978).

22. J. Maurer and A. Libchaber, "Rayleigh-Benard Experiment in Liquid Helium: Frequency Locking and the Onset of Turbulence", J. Phys. Lett., *40* , L419 (1979).

23. A. Wolf, J.B. Swift, H.L. Swinny, and J. Vastano, "Determining Lyapunov Exponents from a Time Series", Physica, *16D* , pg. 285 (1985).

24. Y. Shen, G.P. Neitzel, D.F. Jankowski, and H.D. Mittleman, "Energy Stability of Thermocapillary Convection in a Model of the Float-Zone Crystal Growth Process", J. Fluid Mech., *217*, pg. 639 (1990).

25. A. Pline, "Infrared Surface Temperature Measurements for the Surface Tension Driven Convection Experiment", NASA TM *101353* (1991).

26. W.S. Meyers and H.P. Stahl, "Contouring of a Free Oil Surface", private NASA report obtained by J. Nash (1994).

27. K.C. Hsieh, R.L. Thompson, K.J. DeWitt, J. Nash, D.M. VanZandt, "Oscillatory Thermocapillary Flows Induced by Radiant Heating", AIAA paper No. 95-0823, 33rd Aerospace Sciences Meeting (1995).

28. S. Slimani, N. Aubry, P. Kolodner, and R. Lima, "Biorthogonal Decomposition Analysis of Dispersive Chaos in Binary-Fluid Convection," Proceedings of the 113th ASME Winter Annual Meeting, HTD, *214* (1992).

29. P. Blondeaux and G. Vittori, "A Route to Chaos in an Oscillatory Flow: Feigenbaum Scenario," Physics of Fluids, *A3(11)*, pg. 2492 (1991).

30. P. Blondeaux and G. Vittori, "Vorticity Dynamics in an Oscillatory Flow Over a Rippled Bed," J. Fluid Mech., *226*, pg. 257 (1991).

31. I. Goldhirsch, R.B. Pelz, and S.A. Orzag, "Numerical Simulation of Thermal Convection in a Two-Dimensional Finite Box," J. Fluid Mech., *199*, pg. 1 (1989).

32. D. Mukutmoni and K.T. Yang, "Many Routes to Chaotic Raleigh-Benard Convection in a Small Aspect Ratio Box", Proceedings of the 113th ASME Winter Annual Meeting, HTD, *214*, pgs. 57-68 (1992).

33. D. Mukutmoni and K.T. Yang, "Bifurcation Phenomena and Chaos in Thermal Convection", ASME, *138*, (1992).

IX. Tables and Figures

Bond Numbers Tested for Fixed Values of the Aspect Ratio

Chamber Diameter	**Aspect Ratio**			
	0.5	**1.0**	**1.5**	**2.0**
0.5 cm	0.09	0.74	2.48	5.88
1.0 cm	0.37	2.94	9.92	23.5
1.2 cm	0.53	4.23	14.3	33.9
2.0 cm	1.47	11.8	39.7	94.1
3.0 cm	3.31	26.5	89.3	211.7

Aspect Ratios Tested for Fixed Values of the Bond Number

Chamber Diameter	**Bond Number**		
	0.13	**0.54**	**1.54**
0.5 cm	0.565	0.903	1.280
1.0 cm	0.356	0.569	0.807
1.2 cm	0.315	0.504	0.715
2.0 cm	0.224	0.358	0.508
3.0 cm	0.171	0.273	0.388

Table 1: Test Matrix

Property	Symbol	Value at 25° C
Specific Heat	C_p	$720 \frac{J}{kg \cdot °C}$
Thermal Conductivity	k	$0.1087 \frac{J}{m \cdot s \cdot °C}$
Thermal Diffusivity	α	$7.27 \times 10^{-8} \frac{m^2}{s}$
Volumetric Expansion Coefficient	β	$1.17 \times 10^{-3} \frac{1}{°C}$
Temperature Coefficient of Surface Tension	γ	$8.5 \times 10^{-5} \frac{N}{m \cdot °C}$
Dynamic Viscosity	μ	$1.74 \times 10^{-3} \frac{N \cdot s}{m^2}$
Density	ρ	$872 \frac{kg}{m^3}$
Surface Tension	σ	$0.0187 \frac{N}{m}$
Prandtl Number	Pr	27
Flash Point		189 °C
Refractive Index		1.3904

Table 2: Physical Properties of 2 centistoke Silicon Oil

Aspect Ratio	Bond Number	Critical Ma_t	Critical Osc. Mode	Ma_t for the 2nd Osc.	Ma_t for the 3rd Osc.	Ma_t for the 4th Osc.	Ma_t for the 5th Osc.	Ma_t for the 6th Osc.	Ma_t for the 7th Osc.
0.5	0.09	5.46×10^{4}	C	--	--	--	--	--	--
0.5	0.37	7.36×10^{4}	E	8.03×10^{4}	9.58×10^{4}	--	--	--	--
0.5	0.53	9.84×10^{4}	E	1.02×10^{5}	1.42×10^{5}	--	--	--	--
0.5	1.47	1.49×10^{5}	D	1.56×10^{5}	2.05×10^{5}	2.30×10^{5}	--	--	--
0.5	3.31	3.88×10^{5}	D	4.35×10^{5}	4.57×10^{5}	4.70×10^{5}	--	--	--
1.0	0.74	2.96×10^{4}	A	3.38×10^{4}	3.90×10^{4}	4.60×10^{4}	--	--	--
1.0	2.94	4.60×10^{4}	A	4.67×10^{4}	4.87×10^{4}	6.65×10^{4}	1.05×10^{5}	1.50×10^{5}	1.70×10^{5}
1.0	4.23	5.52×10^{4}	B	6.89×10^{4}	--	--	--	--	--
1.0	11.8	1.13×10^{5}	D	1.40×10^{5}	2.16×10^{5}	--	--	--	--
1.0	26.5	1.97×10^{5}	C	3.63×10^{5}	4.17×10^{5}	--	--	--	--
1.5	2.84	2.74×10^{4}	A	2.84×10^{4}	2.92×10^{4}	4.54×10^{4}	--	--	--
1.5	9.92	3.66×10^{4}	C	4.33×10^{4}	4.50×10^{4}	4.67×10^{4}	7.86×10^{4}	1.23×10^{5}	1.41×10^{5}
1.5	14.3	4.92×10^{4}	D	5.12×10^{4}	6.05×10^{4}	1.21×10^{5}	--	--	--
1.5	39.7	1.18×10^{5}	A&C	1.73×10^{5}	--	--	--	--	--
1.5	89.3	1.70×10^{5}	C	2.99×10^{5}	3.72×10^{5}	--	--	--	--
2.0	5.88	2.96×10^{4}	C	3.02×10^{4}	4.43×10^{4}	6.48×10^{4}	9.86×10^{4}	1.19×10^{5}	--
2.0	23.5	4.47×10^{4}	C	4.80×10^{4}	1.30×10^{5}	--	--	--	--
2.0	33.9	5.56×10^{4}	B	6.93×10^{4}	--	--	--	--	--
2.0	94.1	1.02×10^{5}	A&C	2.41×10^{5}	--	--	--	--	--
2.0	211.7	1.50×10^{5}	C	2.05×10^{5}	3.17×10^{5}	--	--	--	--

Table 3: Marangoni Numbers for Constant Aspect Ratio Cases

Bond Number	Aspect Ratio	Critical Ma_t	Critical Osc. Mode	Ma_t for the 2nd Osc.	Ma_t for the 3rd Osc.	Ma_t for the 4th Osc.	Ma_t for the 5th Osc.	Ma_t for the 6th Osc.	Ma_t for the 7th Osc.
0.13	0.565	4.30×10^{4}	E	4.72×10^{4}	--	--	--	--	--
0.13	0.356	1.05×10^{5}	E	1.16×10^{5}	--	--	--	--	--
0.13	0.315	--	--	--	--	--	--	--	--
0.13	0.224	1.77×10^{5}	C	--	--	--	--	--	--
0.13	0.171	--	--	--	--	--	--	--	--
0.54	0.903	2.96×10^{4}	A	3.38×10^{4}	3.90×10^{4}	4.10×10^{4}	--	--	--
0.54	0.569	7.83×10^{4}	E	8.00×10^{4}	9.64×10^{4}	--	--	--	--
0.54	0.504	9.80×10^{4}	E	1.02×10^{5}	1.42×10^{5}	--	--	--	--
0.54	0.358	2.10×10^{5}	D	2.26×10^{5}	2.60×10^{5}	--	--	--	--
0.54	0.273	--	--	--	--	--	--	--	--
1.54	1.28	2.79×10^{4}	A	2.86×10^{4}	4.10×10^{4}	--	--	--	--
1.54	0.807	5.24×10^{4}	A	7.73×10^{4}	--	--	--	--	--
1.54	0.715	6.77×10^{4}	A	1.06×10^{5}	--	--	--	--	--
1.54	0.508	1.49×10^{5}	D	1.57×10^{5}	2.05×10^{5}	2.30×10^{5}	--	--	--
1.54	0.388	3.51×10^{5}	D	3.77×10^{5}	--	--	--	--	--

Table 4: Marangoni Numbers for Constant Bond Number Cases

Aspect Ratio	Bond Number	Critical Ma_t	Critical Ma_t, Nash [19]
0.5	0.09	5.46×10^4	3.03×10^4
0.5	0.37	7.36×10^4	6.99×10^4
0.5	0.53	9.84×10^4	8.45×10^4
0.5	1.47	1.49×10^5	1.29×10^5
0.5	3.31	3.88×10^5	no data
1.0	0.74	2.96×10^4	1.76×10^4
1.0	2.94	4.60×10^4	2.42×10^4
1.0	4.23	5.52×10^4	3.85×10^4
1.0	11.8	1.13×10^5	1.10×10^5
1.0	26.5	1.97×10^5	no data
1.5	2.84	2.74×10^4	1.94×10^4
1.5	9.92	3.66×10^4	3.04×10^4
1.5	14.3	4.92×10^4	3.65×10^4
1.5	39.7	1.18×10^5	1.04×10^5
1.5	89.3	1.70×10^5	no data
2.0	5.88	2.96×10^4	1.67×10^4
2.0	23.5	4.47×10^4	2.28×10^4
2.0	33.9	5.56×10^4	3.21×10^4
2.0	94.1	1.02×10^5	9.17×10^4
2.0	211.7	1.50×10^5	no data

Aspect Ratio	Bond Number	Critical Ma_t	Critical Ma_t, Nash [19]
0.565	0.13	4.30×10^4	2.52×10^4
0.356	0.13	1.05×10^5	9.47×10^4
0.315	0.13	-	1.42×10^5
0.224	0.13	1.77×10^5	no data
0.171	0.13	-	no data
0.903	0.54	2.95×10^4	1.93×10^4
0.569	0.54	7.83×10^4	5.04×10^4
0.504	0.54	9.80×10^4	7.74×10^4
0.358	0.54	2.10×10^5	no data
0.273	0.54	-	no data
1.28	1.54	2.79×10^4	2.23×10^4
0.807	1.54	5.24×10^4	2.86×10^4
0.715	1.54	6.77×10^4	4.37×10^4
0.508	1.54	1.50×10^5	1.26×10^5
0.388	1.54	3.51×10^5	no data

Table 5: Critical Marangoni Values

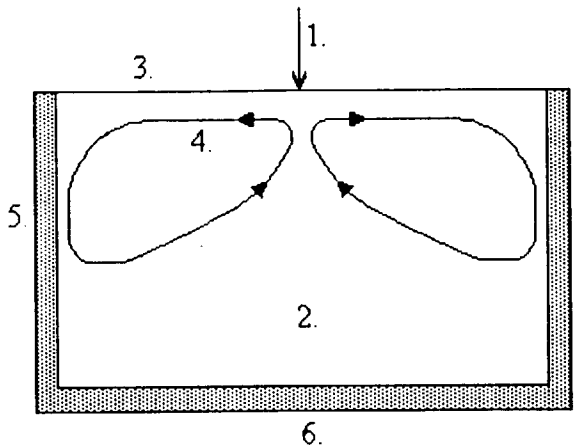

1. Radiant Heat Source
2. Test Fluid
3. Free Fluid Surface
4. Fluid Motion
5. Cooled Side Walls
6. Insulated Base

Figure 1: Marangoni Flow Caused by a Radiant Heat Source

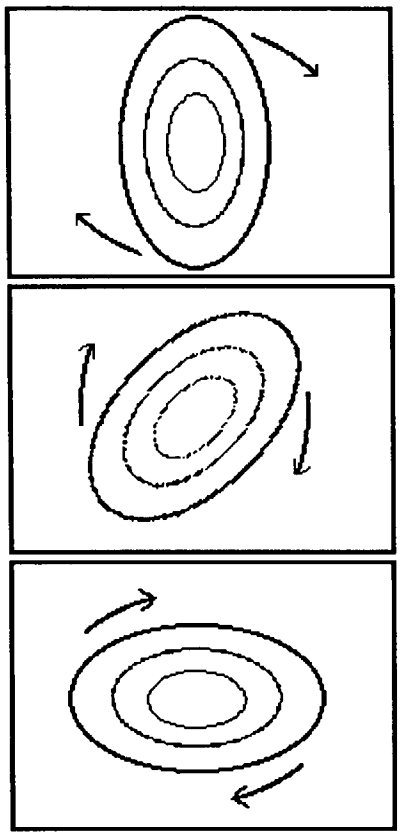

Figure 2: Oscillatory Motion

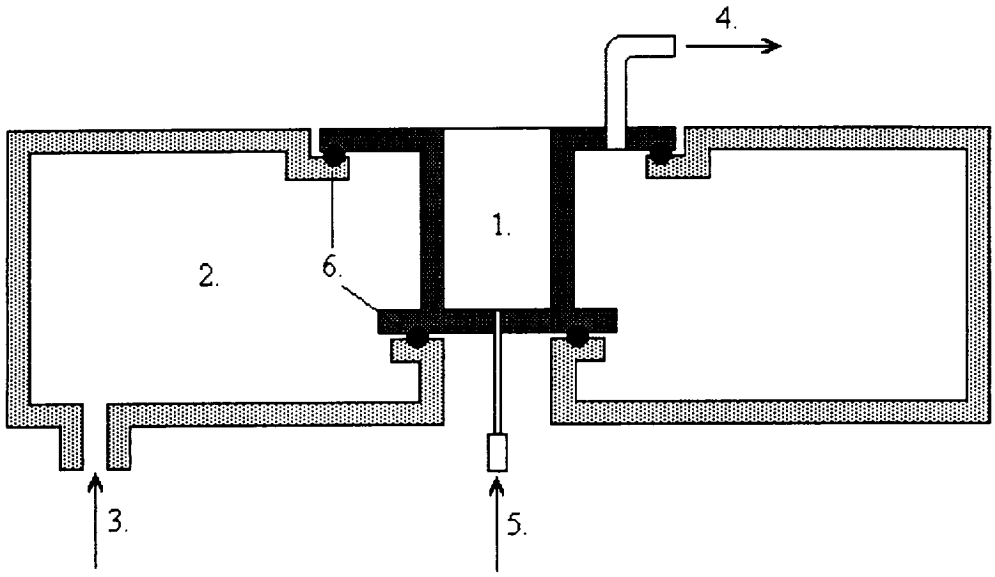

1. Test Chamber
2. Water Bath
3. Cooling Water Inlet
4. Cooling Water Outlet
5. Oil Feed
6. Rubber O-Rings

Figure 3: Test Chamber with Cooling Water Jacket

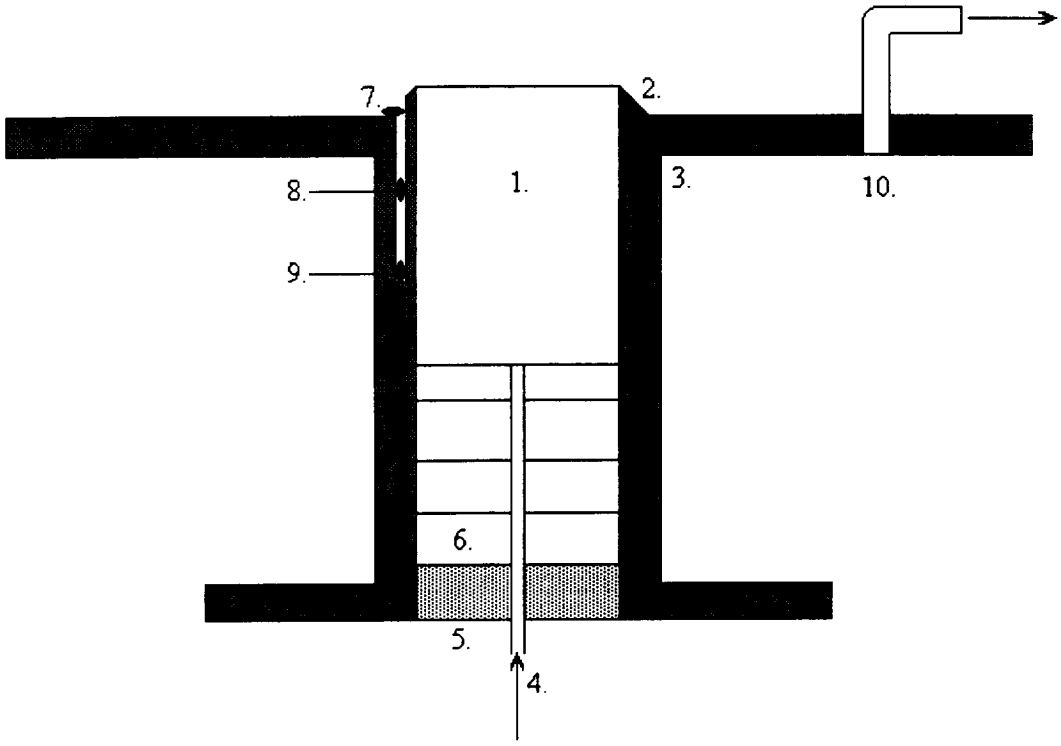

1. Test Fluid
2. Pinning Edge
3. Anodized Aluminum Walls
4. Oil Feed Inlet
5. Aluminum Base
6. Plexiglas Disc
7. Thermistor 1
8. Thermistor 2
9. Thermistor 3
10. Cooling Water Outlet

Figure 4: Test Chamber

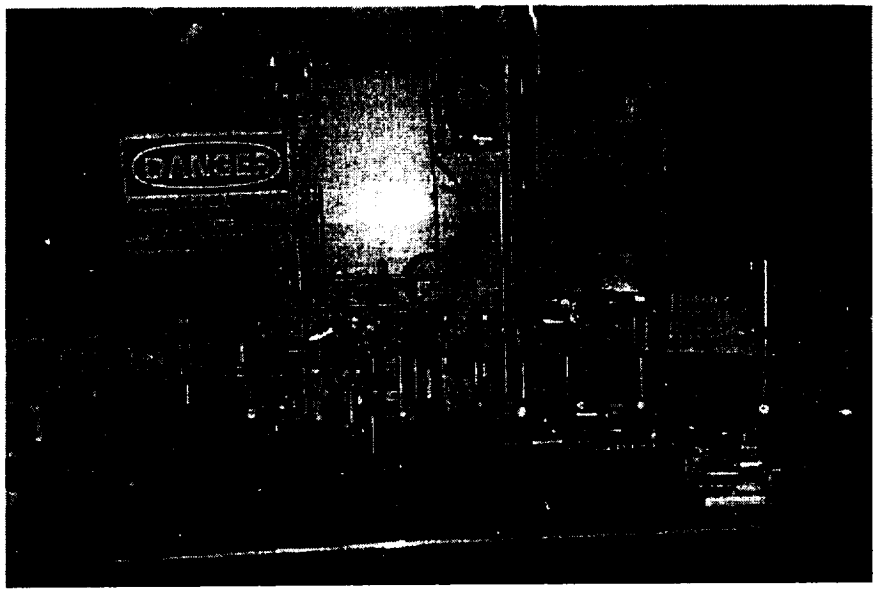

Figure 5: Experiment Setup

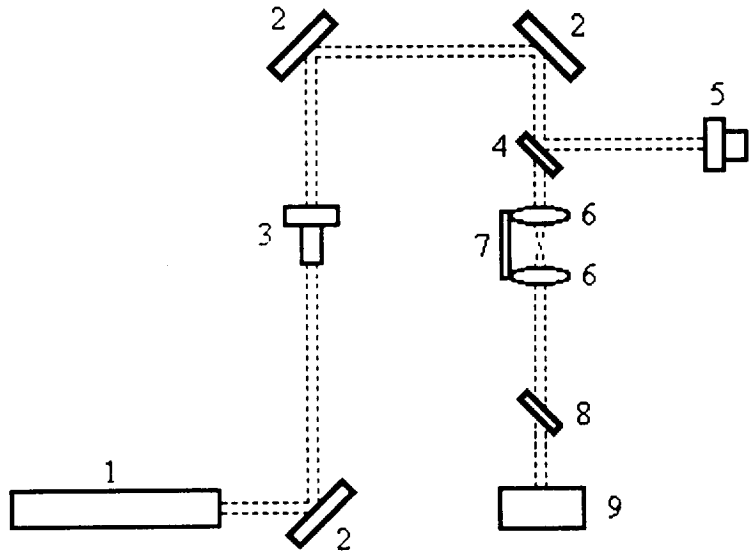

1. CO2 Laser
2. Flat Mirrors
3. Polarizer - Attenuator
4. 90/10 ZnSe Beam Splitter
5. Power Meter Detector Head
6. ZnSe Focusing Lenses
7. Motor-Micrometer
8. ZnSe Beam Combiner
9. Test Chamber/Water Bath

Figure 6: Laser System

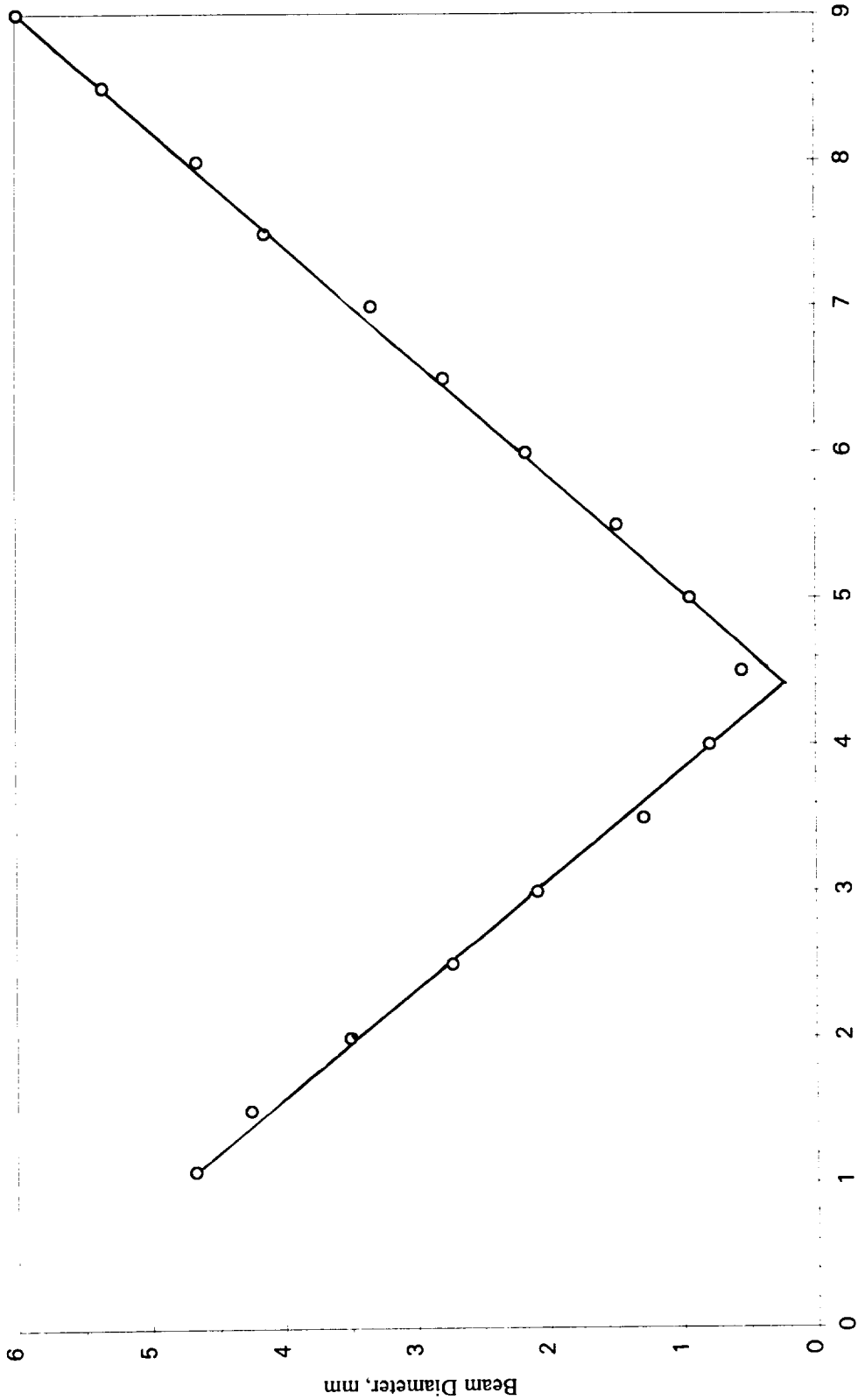

Figure 7: Beam Diameter versus Micrometer Resistance

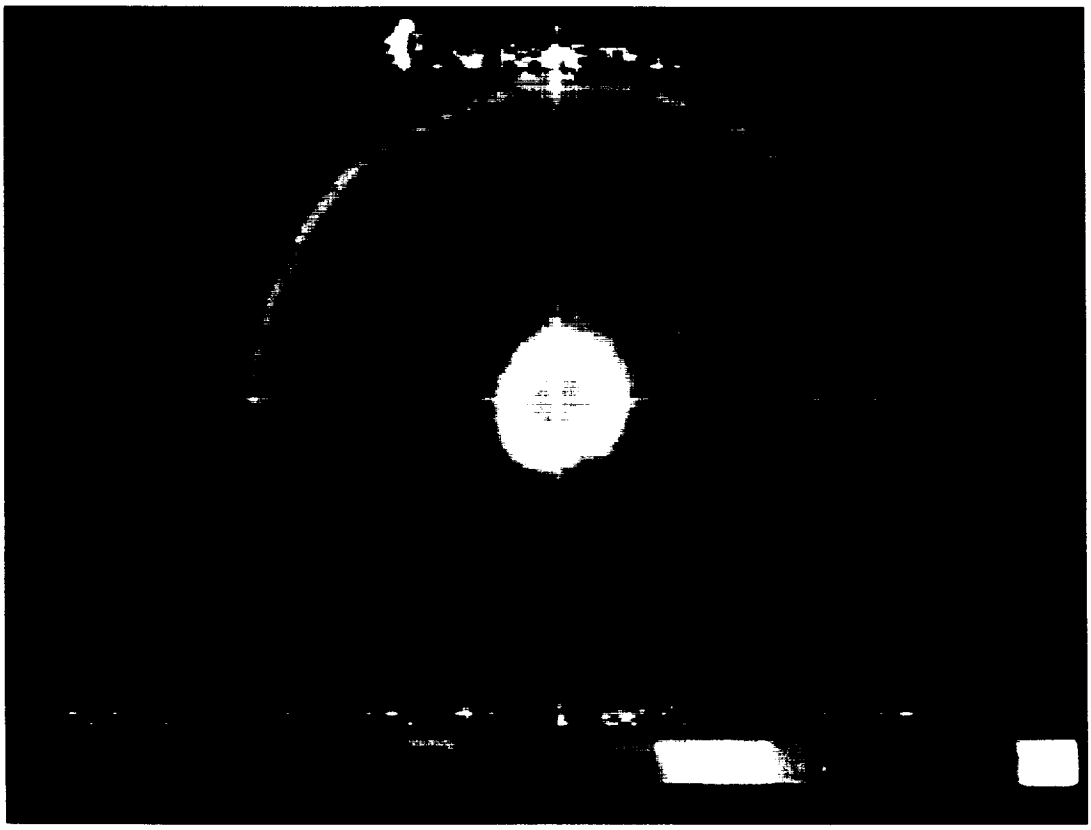

Figure 8: Infrared Image of a Temperature Gradient

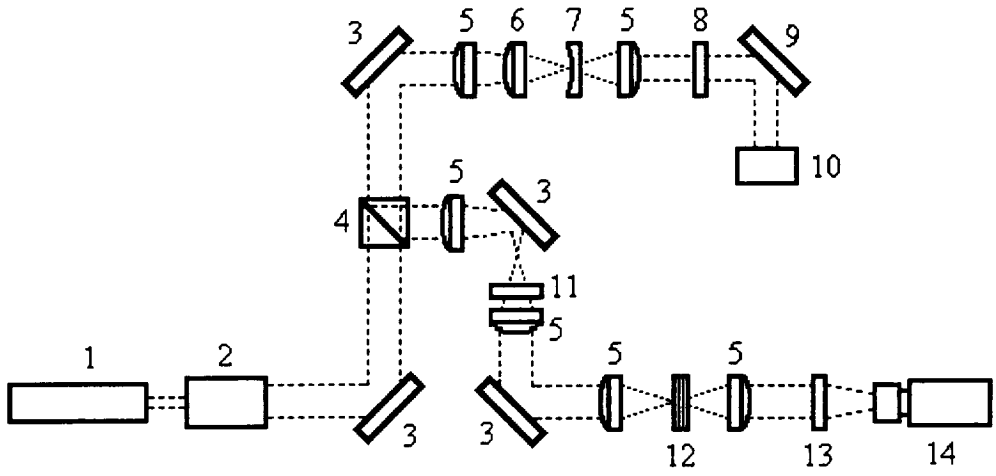

1. Helium-Neon Laser
2. Beam Expander
3. Mirror
4. Cubic Beam Splitter
5. 90 mm Focal Length Lenses
6. 90 mm Focal Length Flip Lens
7. -60 mm Focal Length Flip Lens
8. Quarter Wave Plate
9. ZnSe Beam Combiner
10. Test Chamber/Water Bath
11. Linear Polarizer
12. Diffraction Grating
13. Projection Screen
14. CCD Camera

Figure 9: Free Surface Deformation Imaging System

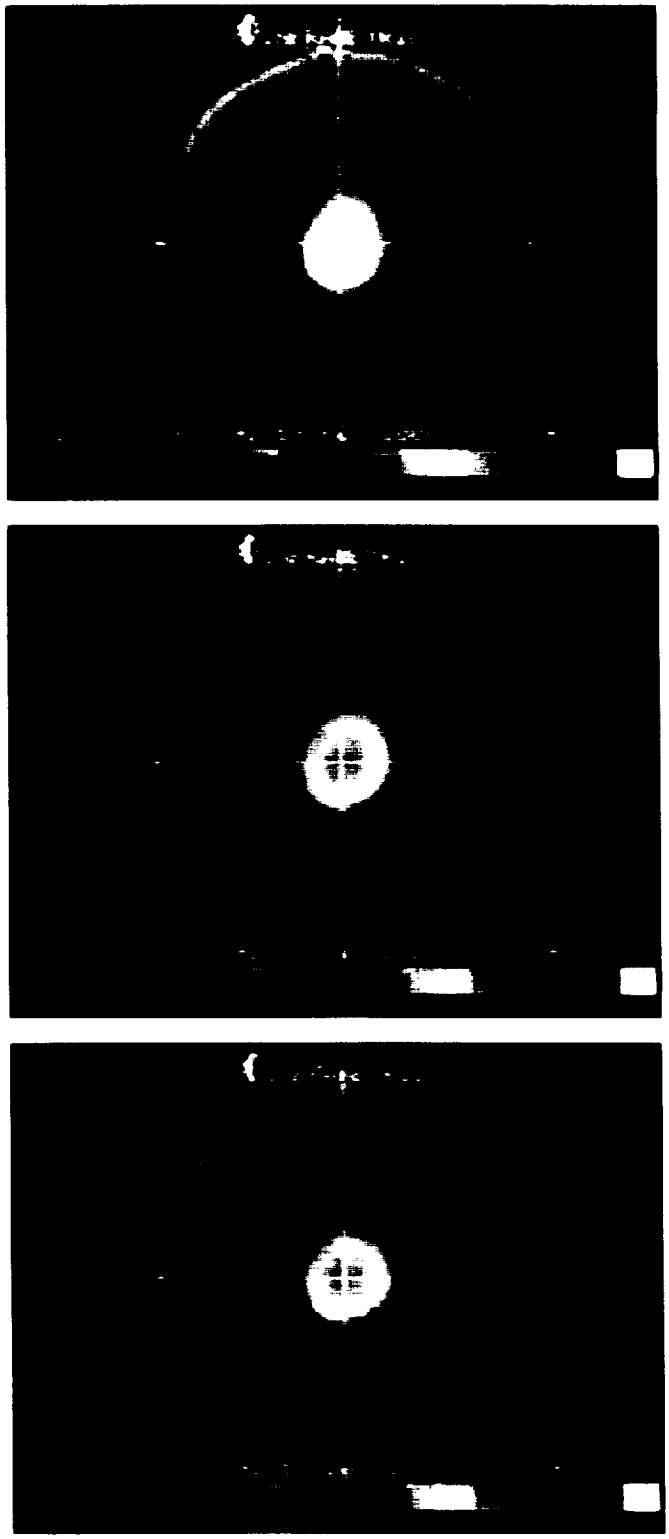

Figure 12: Mode A (Swirling) Oscillations

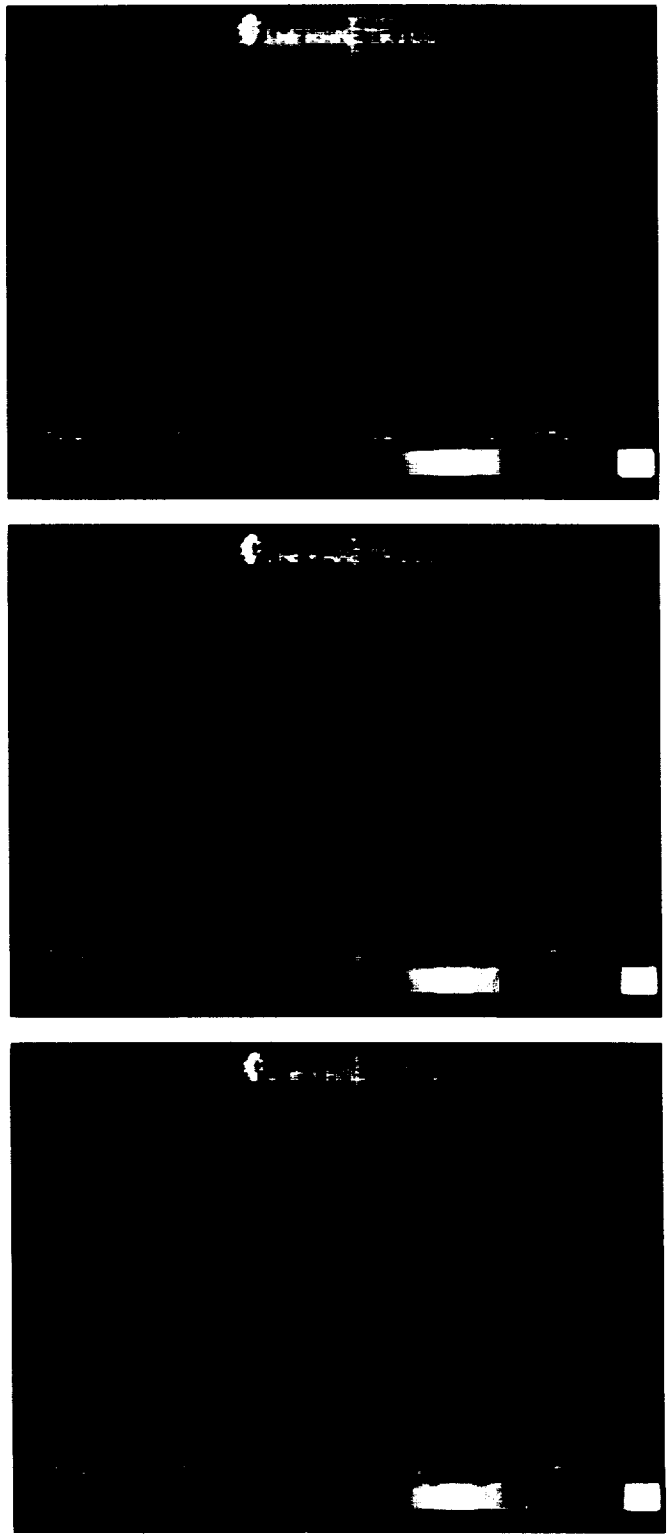

Figure 13: Mode B (Twisting) Oscillations

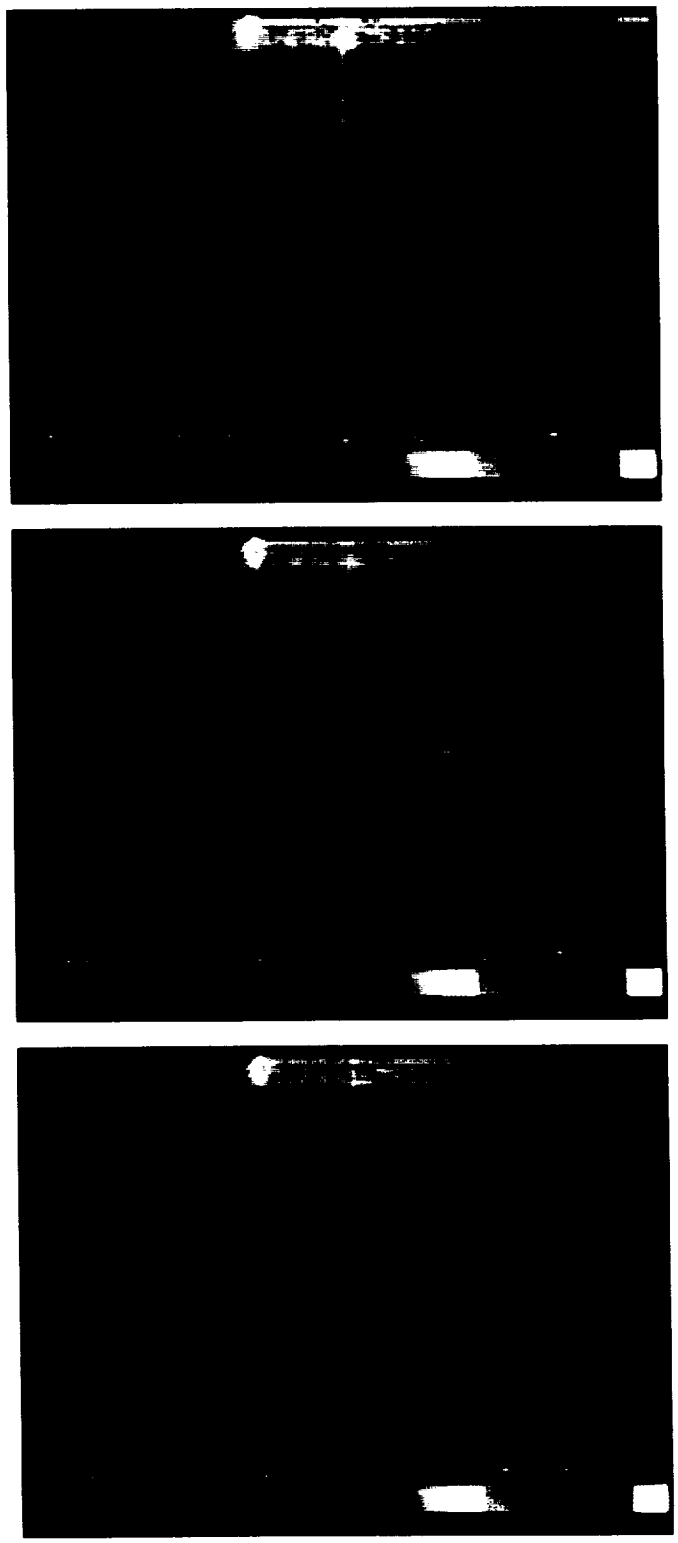

Figure 14: Mode C (Sloshing) Oscillations

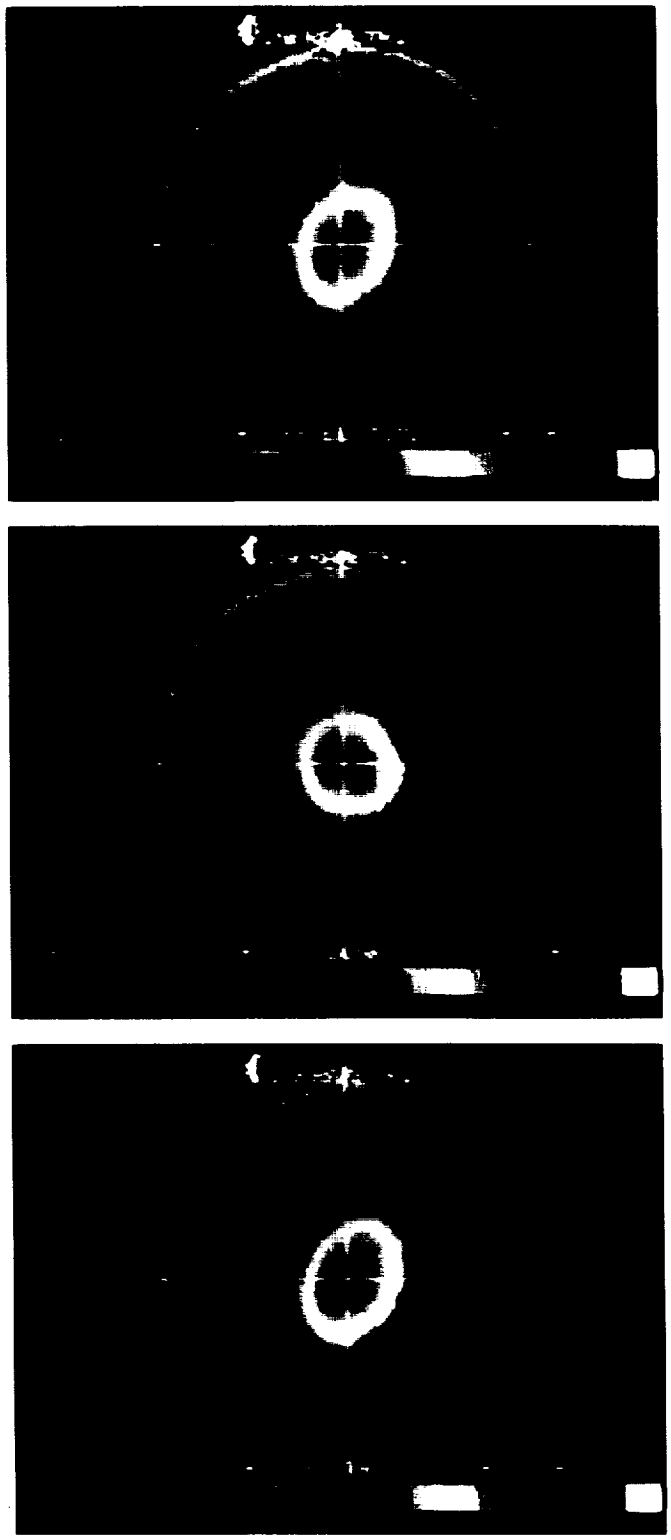

Figure 15: Mode D (Beating) Oscillations

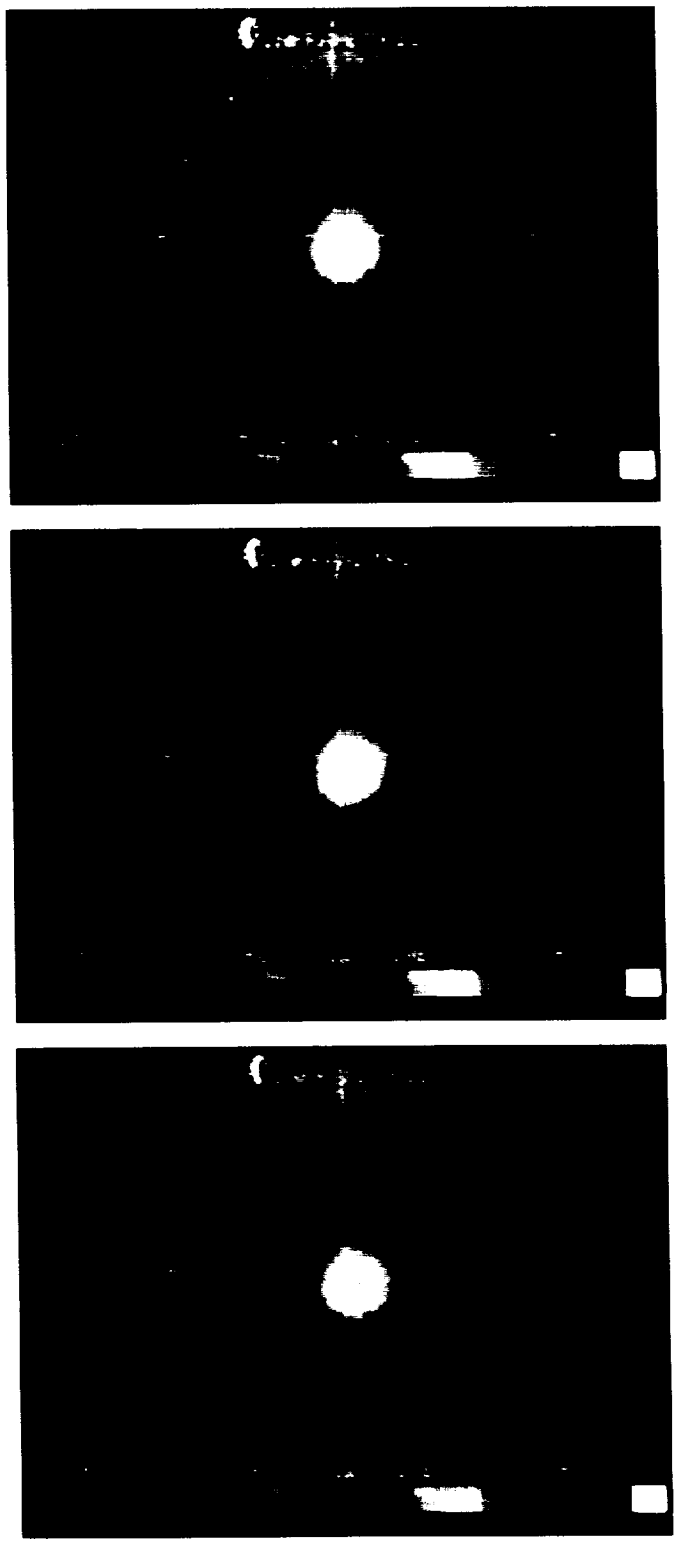

Figure 16: Mode E (3-Lobe Beating) Oscillations

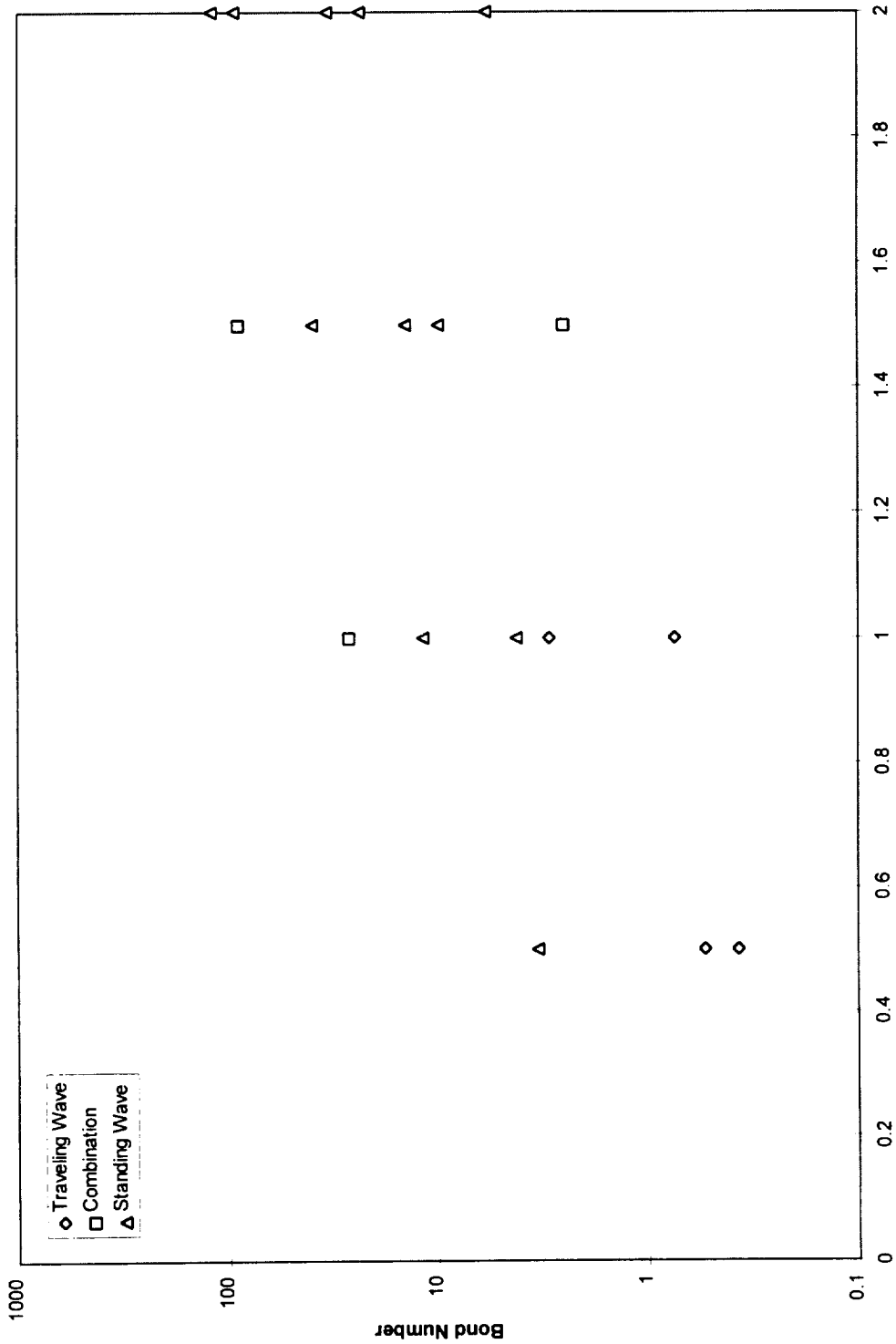

Figure 17: Wave Forms Observed During the Second Oscillatory Pattern

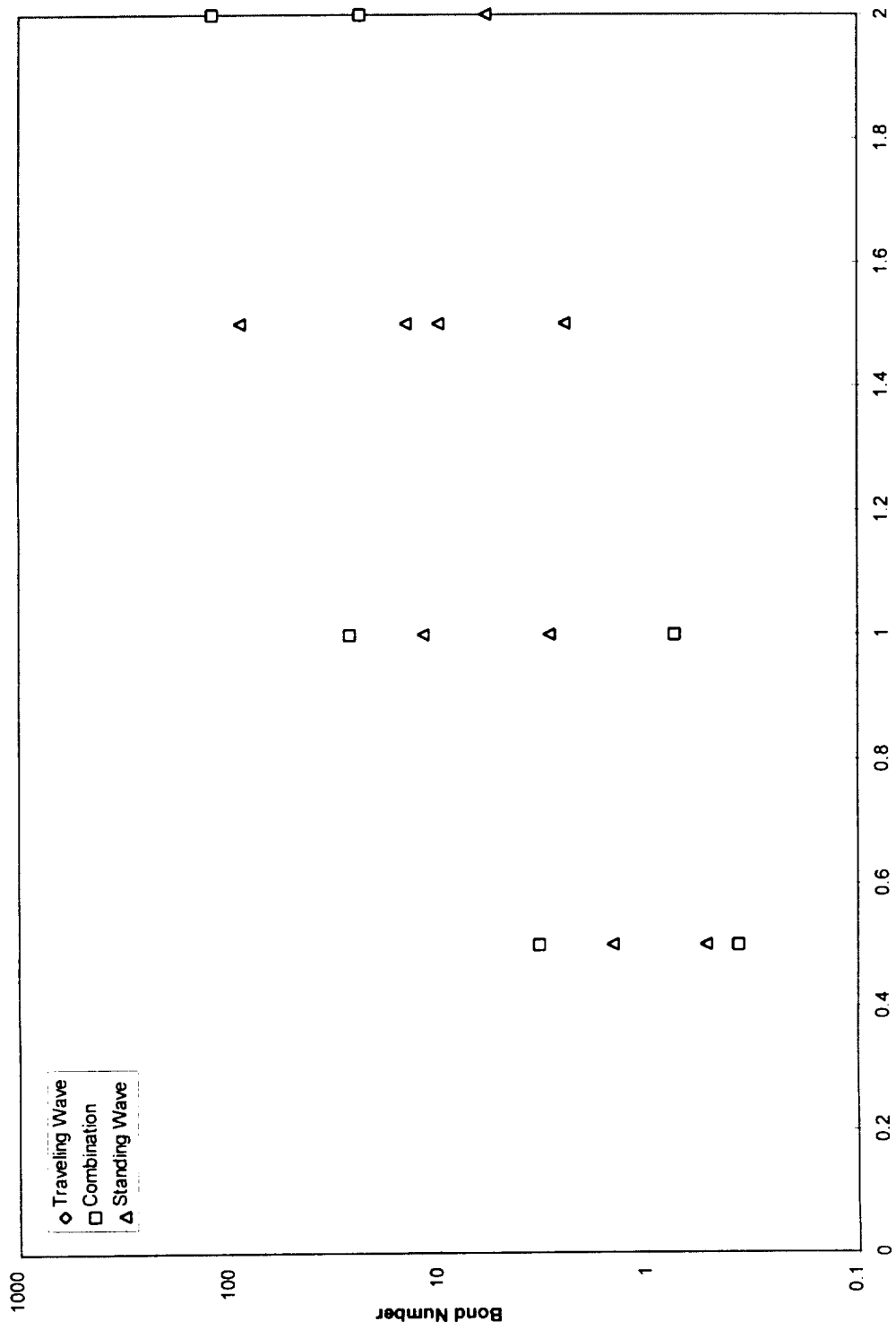

Figure 18: Wave Forms Observed During the Third Oscillatory Pattern

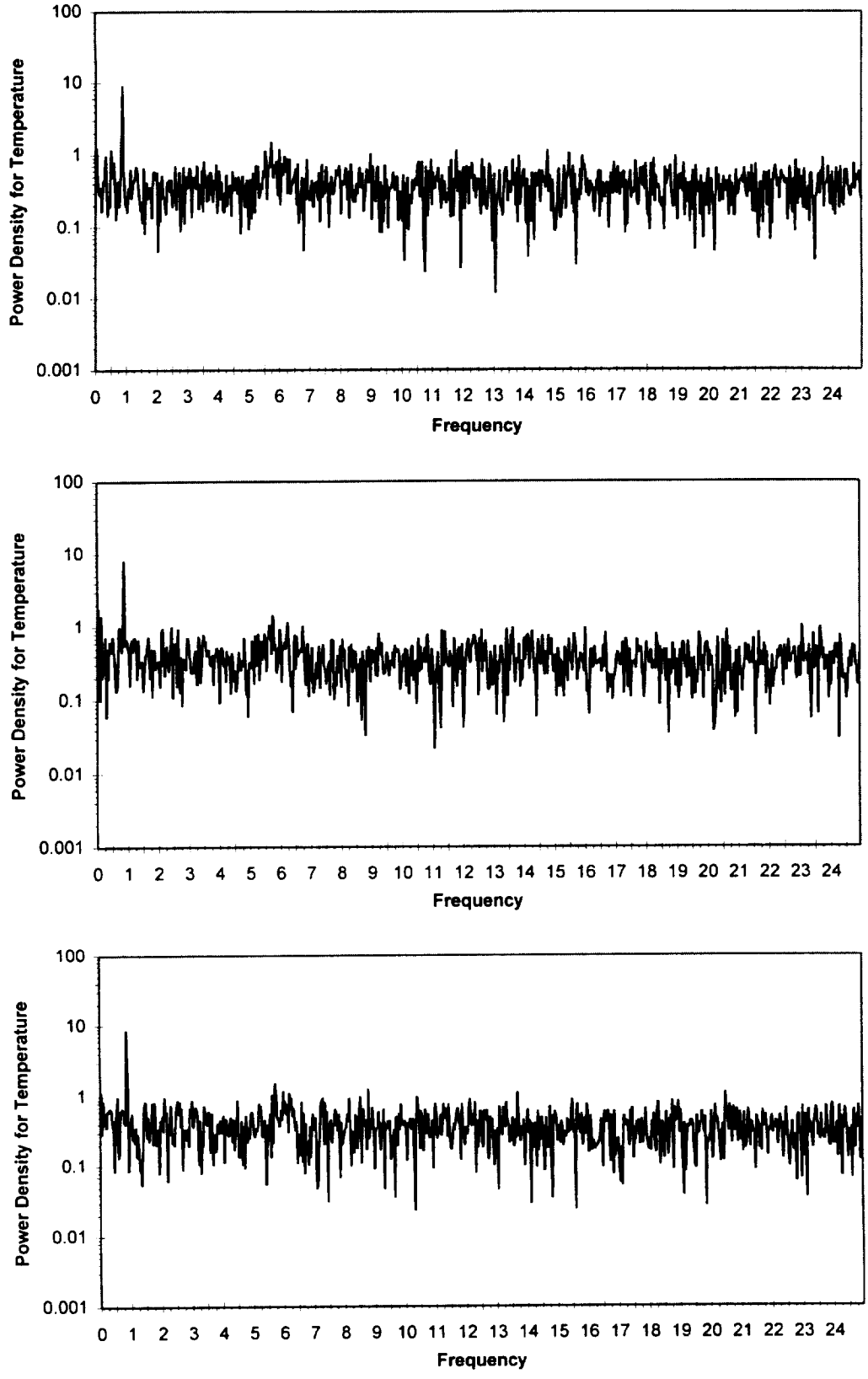

Figure 19: Power Spectrums for the Second Observed Oscillation of the Diameter 1.0, Aspect Ratio 1.0, Bond Number 2.94 Case

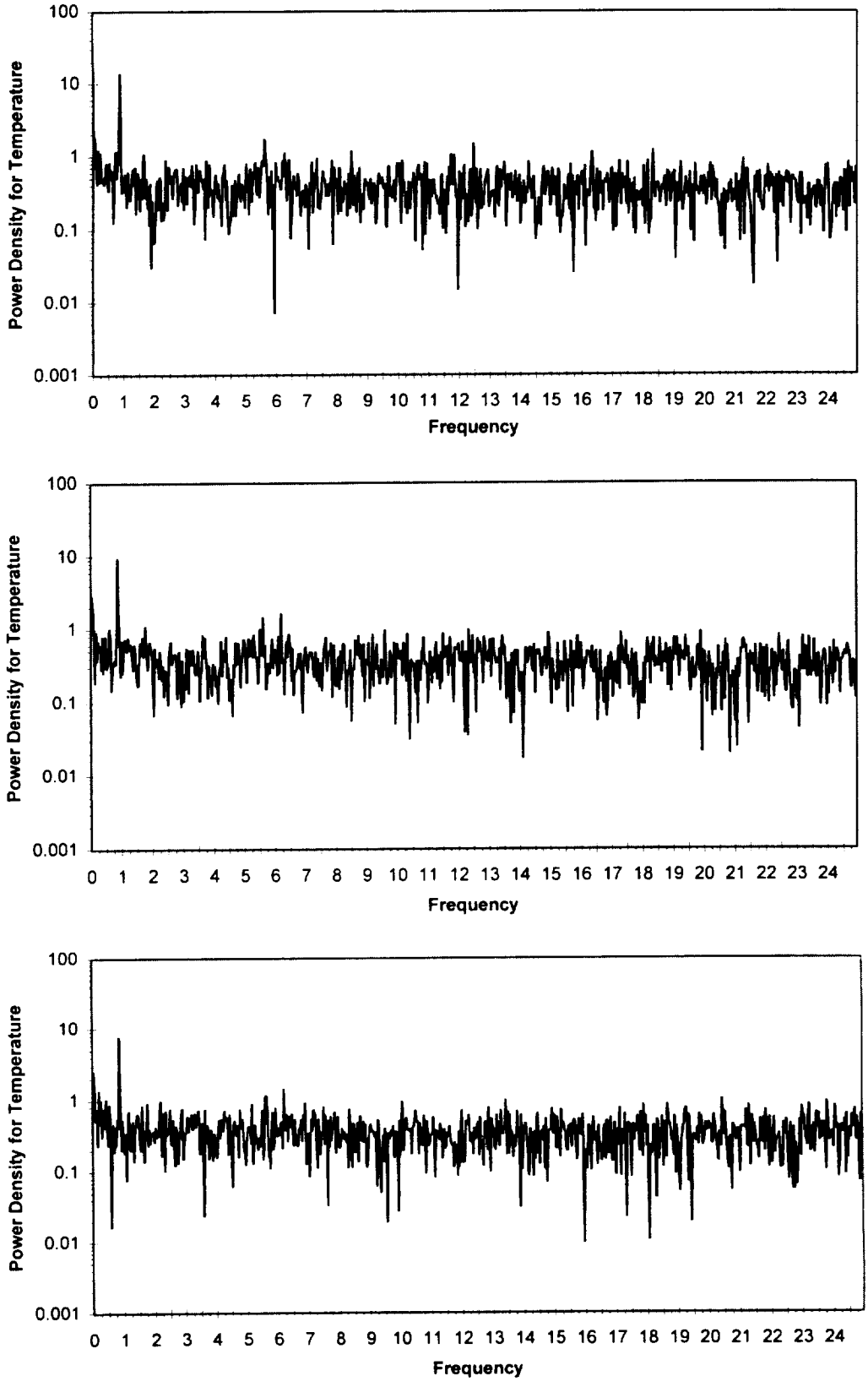

Figure 20: Power Spectrums for the Third Observed Oscillation of the Diameter 1.0, Aspect Ratio 1.0, Bond Number 2.94 Case

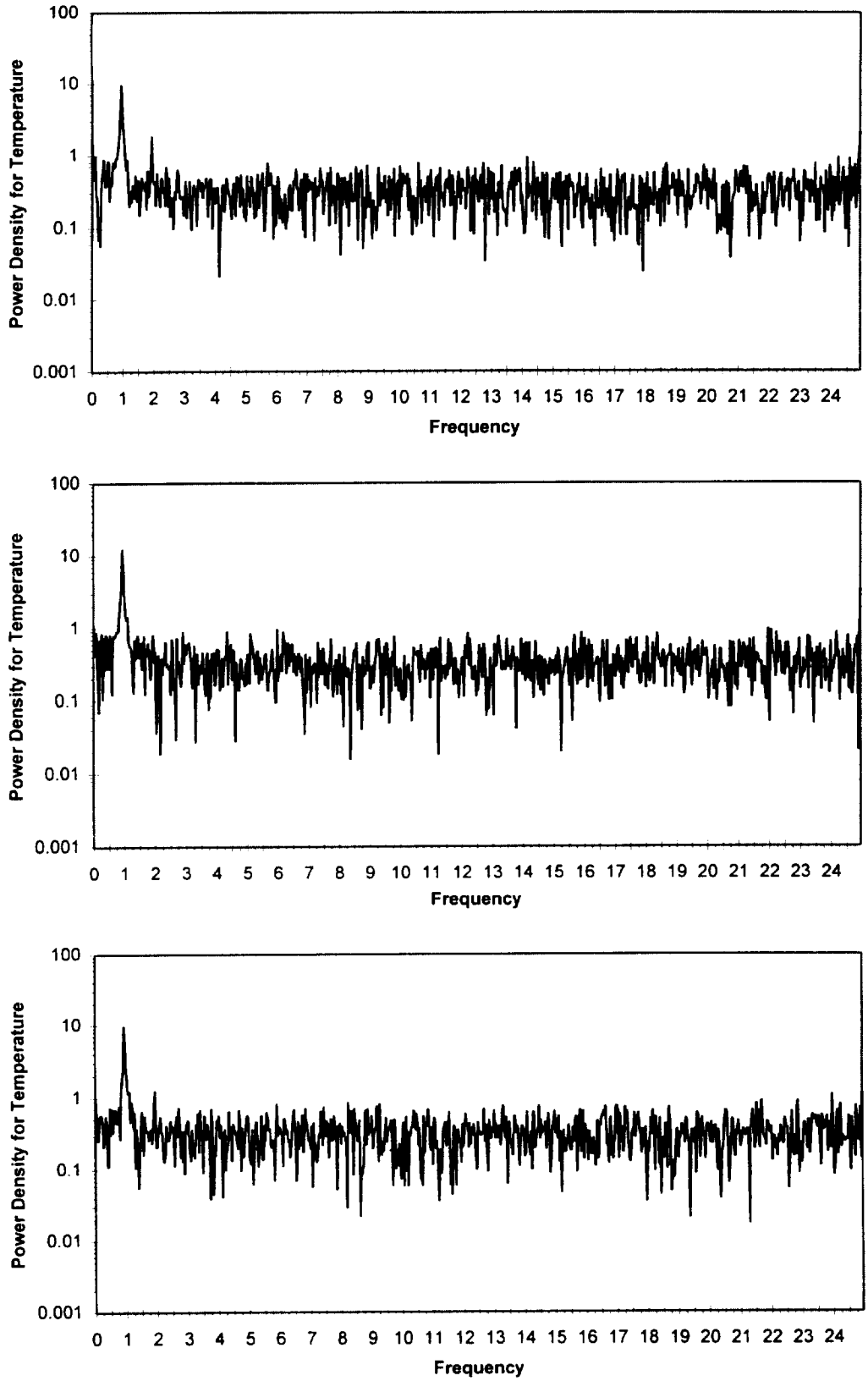

Figure 21: Power Spectrums for the Fourth Observed Oscillation of the Diameter 1.0, Aspect Ratio 1.0, Bond Number 2.94 Case

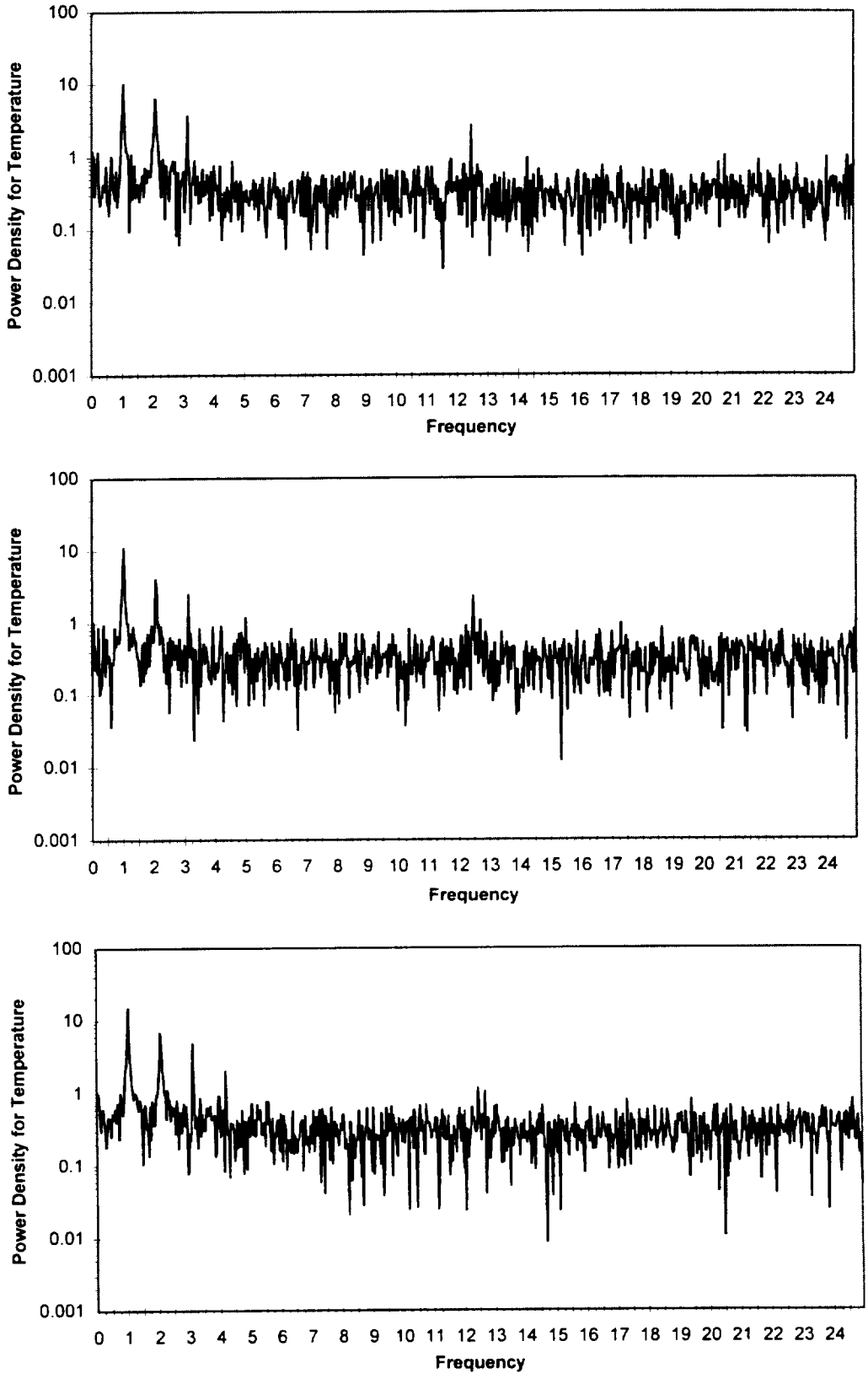

Figure 22: Power Spectrums for the Fifth Observed Oscillation of the Diameter 1.0, Aspect Ratio 1.0, Bond Number 2.94 Case

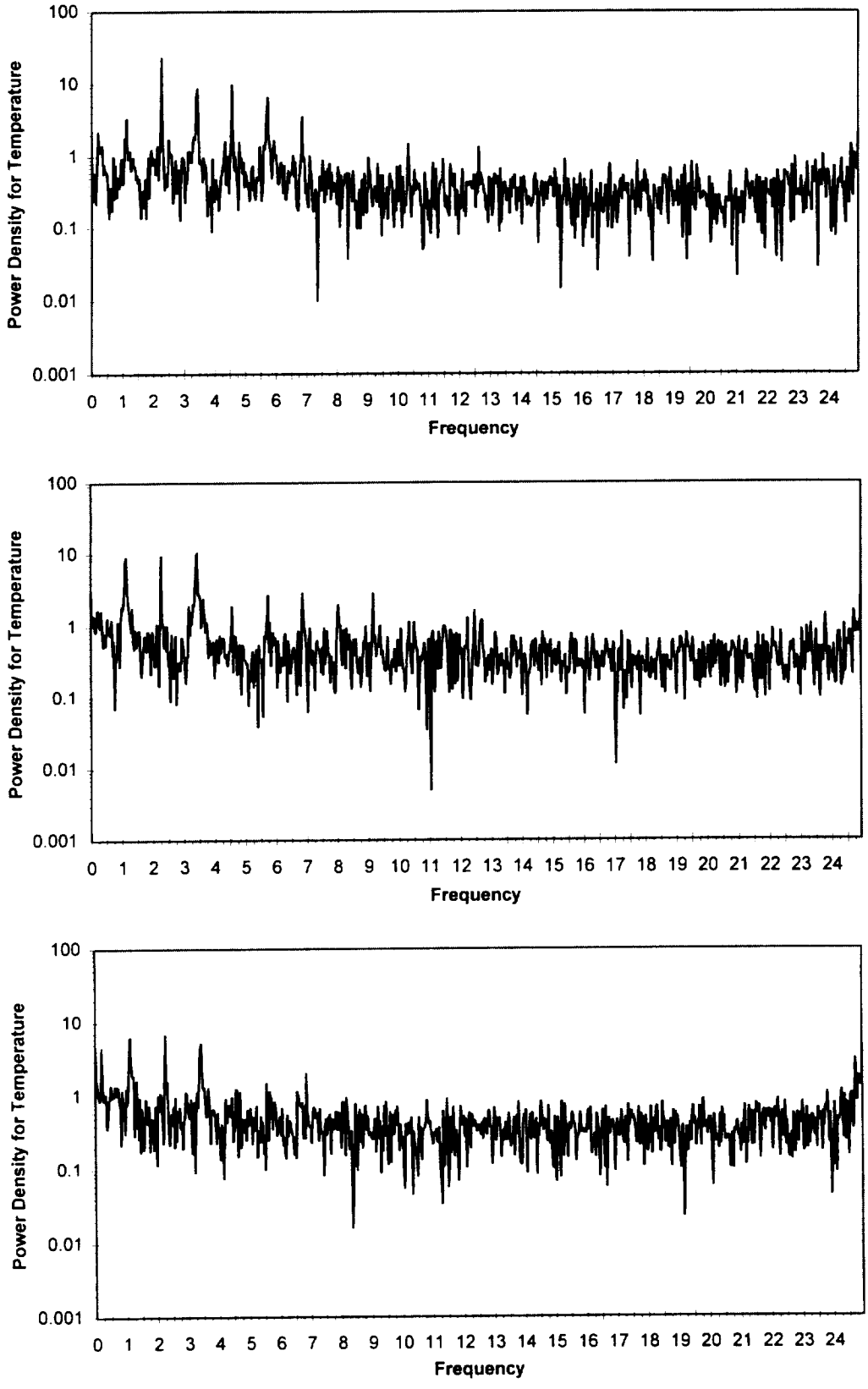

Figure 23: Power Spectrums for the Sixth Observed Oscillation of the Diameter 1.0, Aspect Ratio 1.0, Bond Number 2.94 Case

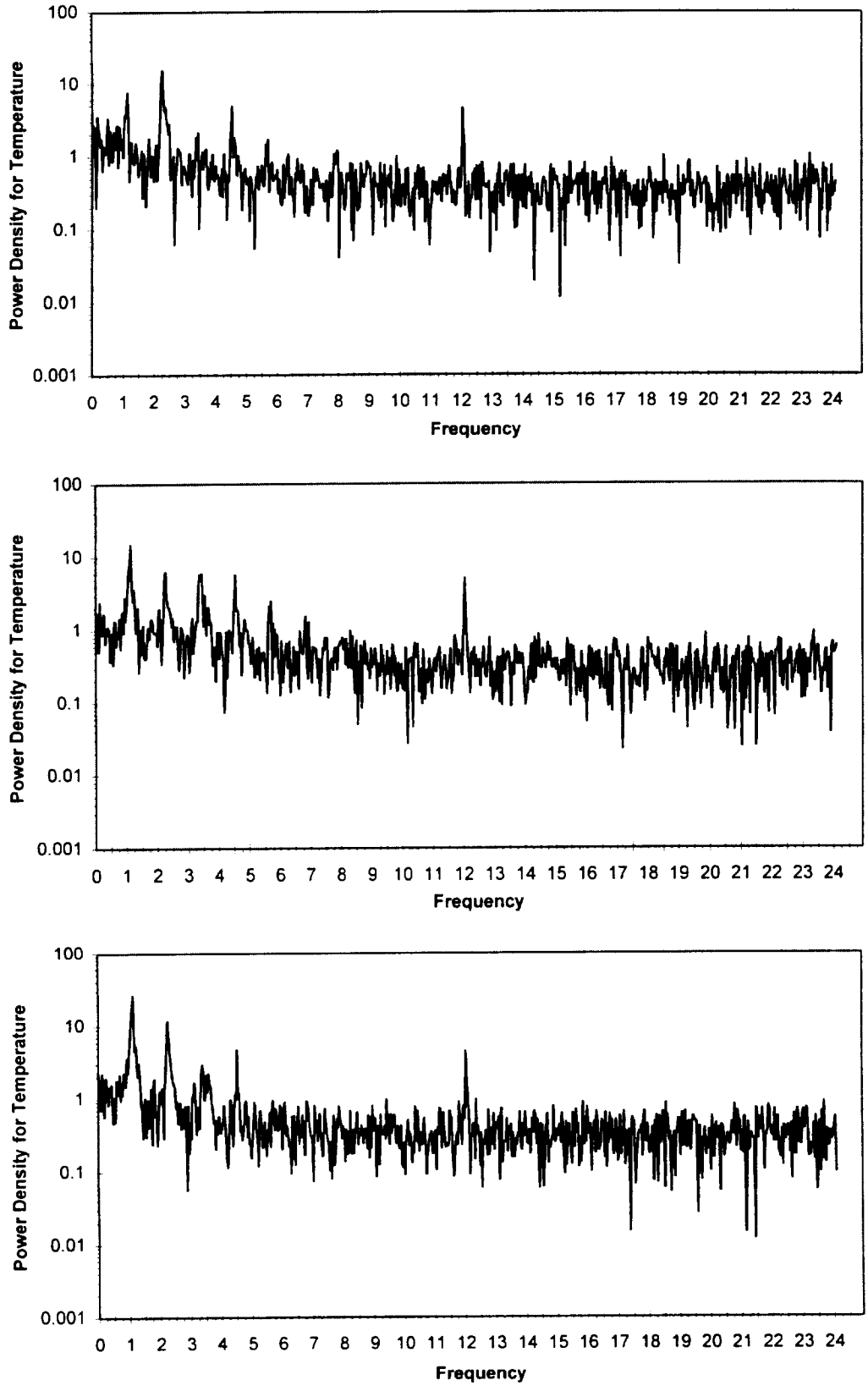

Figure 24: Power Spectrums for the Seventh Observed Oscillation of the Diameter 1.0, Aspect Ratio 1.0, Bond Number 2.94 Case

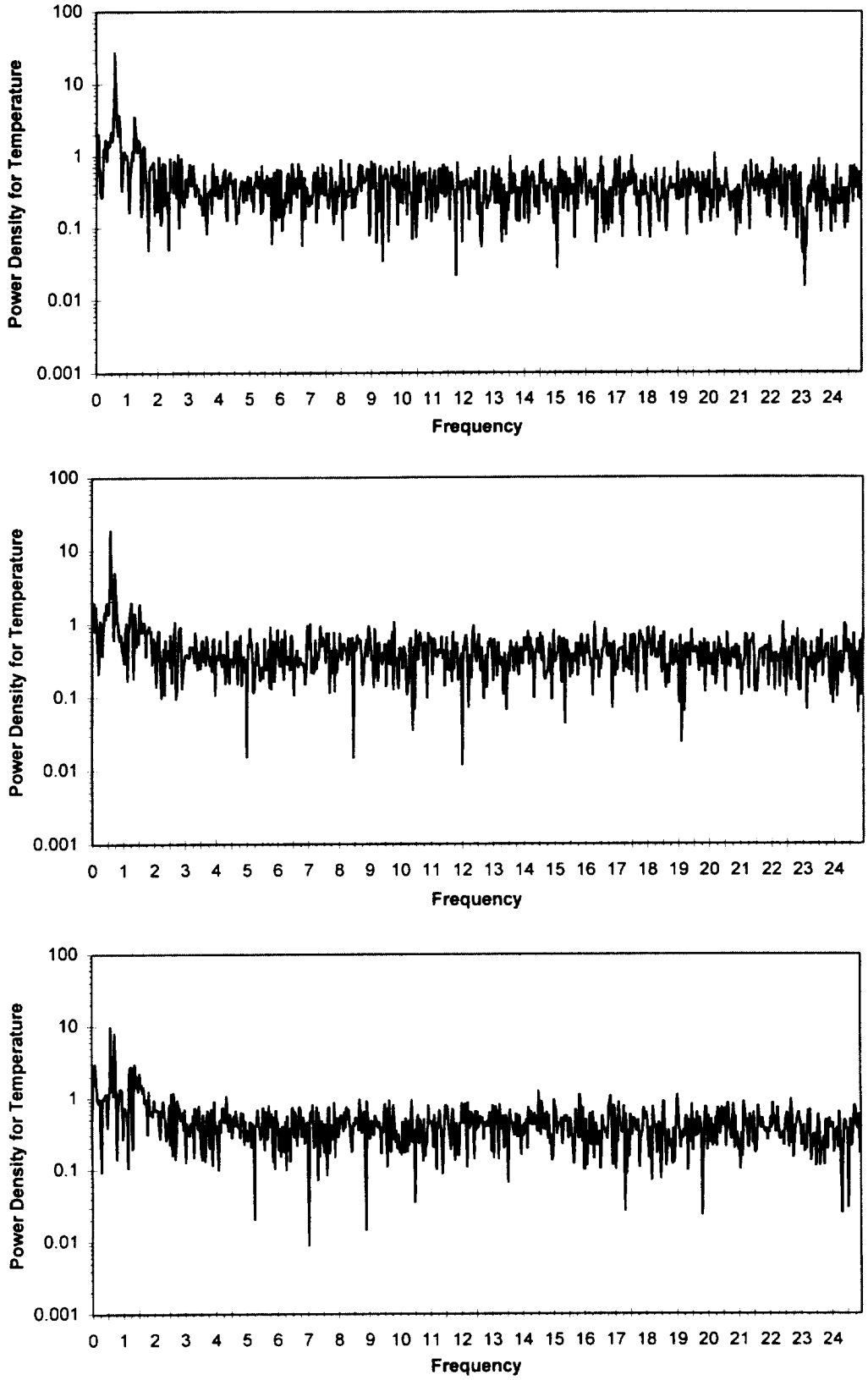

Figure 25: Power Spectrums for the Second Observed Oscillation of the Diameter 3.0, Aspect Ratio 0.5, Bond Number 3.31 Case

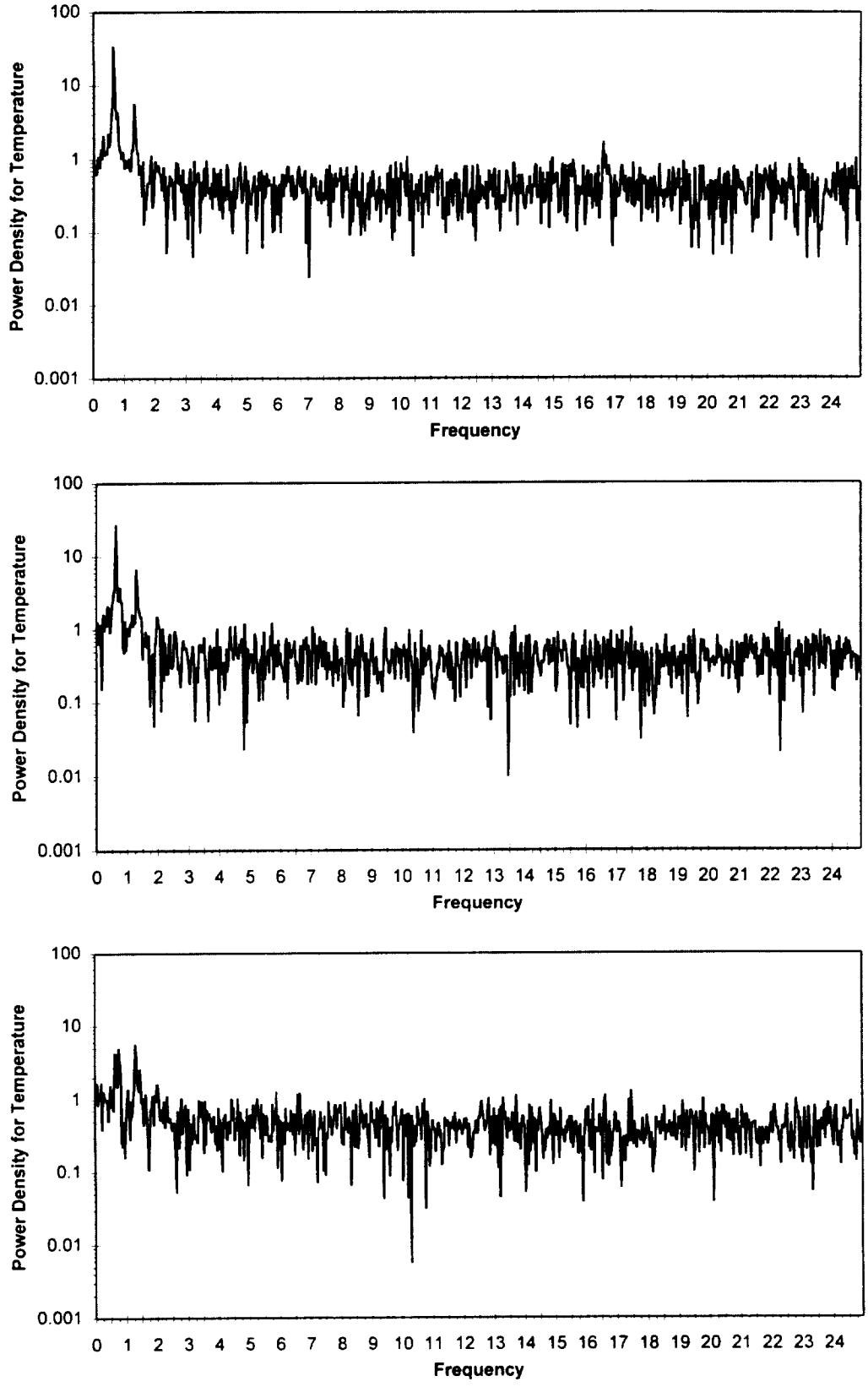

Figure 26: Power Spectrums for the Third Observed Oscillation of the Diameter 3.0, Aspect Ratio 0.5, Bond Number 3.31 Case

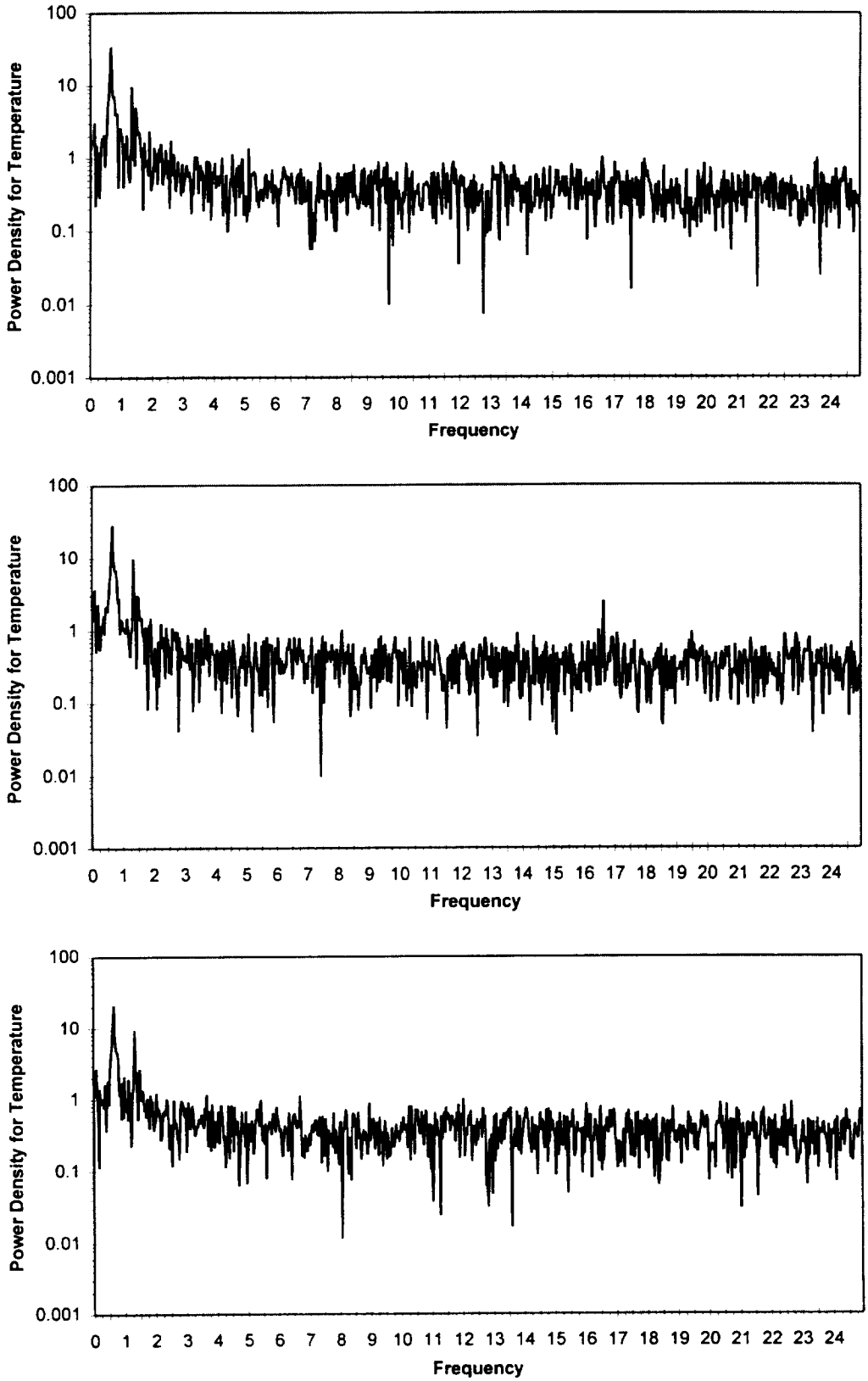

Figure 27: Power Spectrums for the Fourth Observed Oscillation of the Diameter 3.0, Aspect Ratio 0.5, Bond Number 3.31 Case

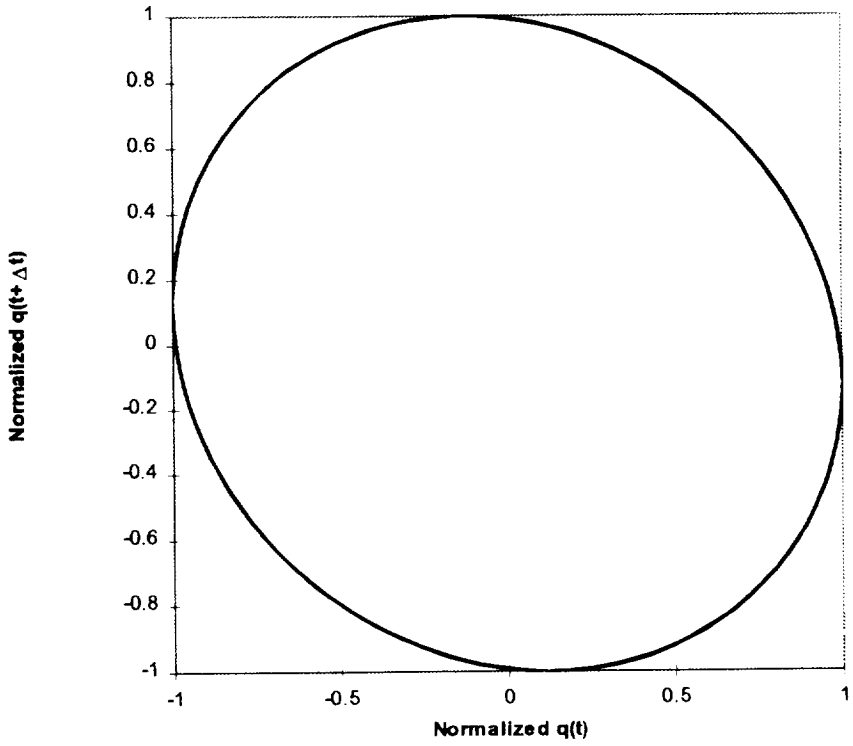

Figure 28A: Phase Trajectory for the Second Oscillation, Chamber Diameter 1.0 cm, Aspect Ratio 1.0, Bond Number 2.94 Case

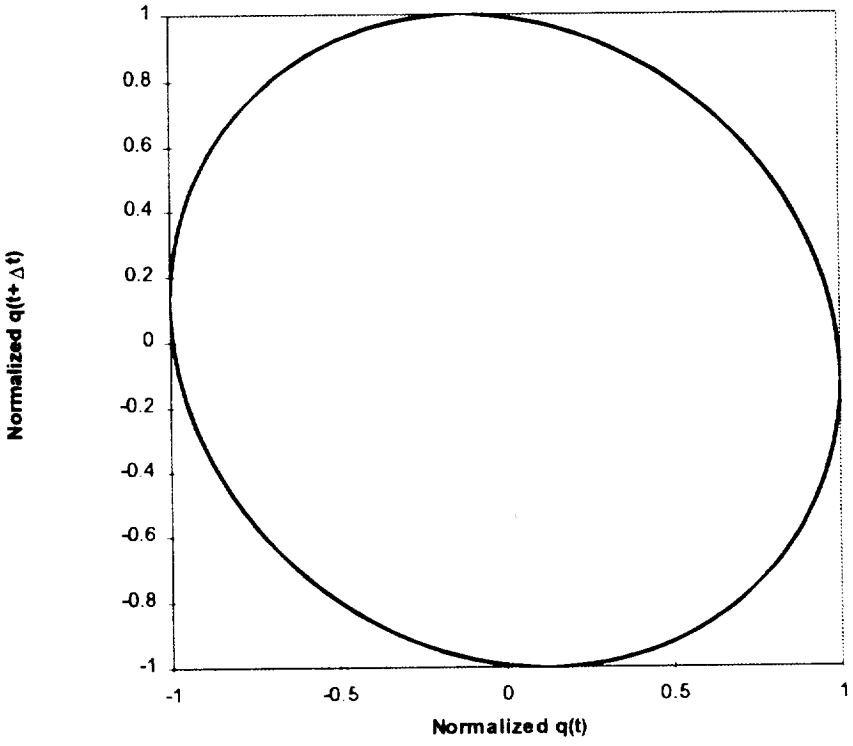

Figure 28B: Phase Trajectory for the Third Oscillation, Chamber Diameter 1.0 cm, Aspect Ratio 1.0, Bond Number 2.94 Case

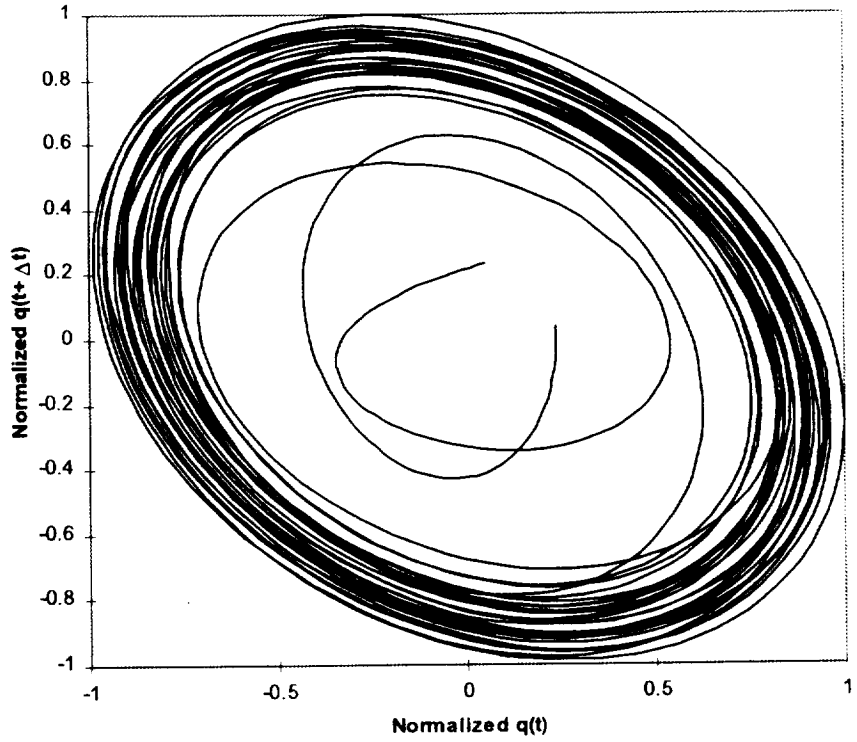

Figure 28C: Phase Trajectory for the Fourth Oscillation, Chamber Diameter 1.0 cm, Aspect Ratio 1.0, Bond Number 2.94 Case

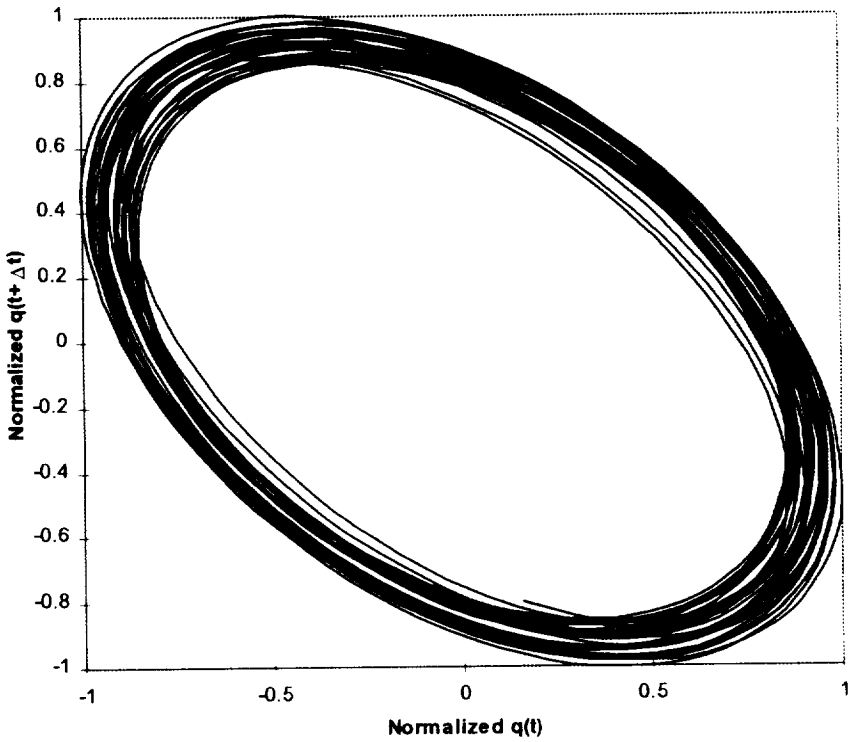

Figure 28D: Phase Trajectory for the Fifth Oscillation Chamber Diameter 1.0 cm, Aspect Ratio 1.0, Bond Number 2.94 Case

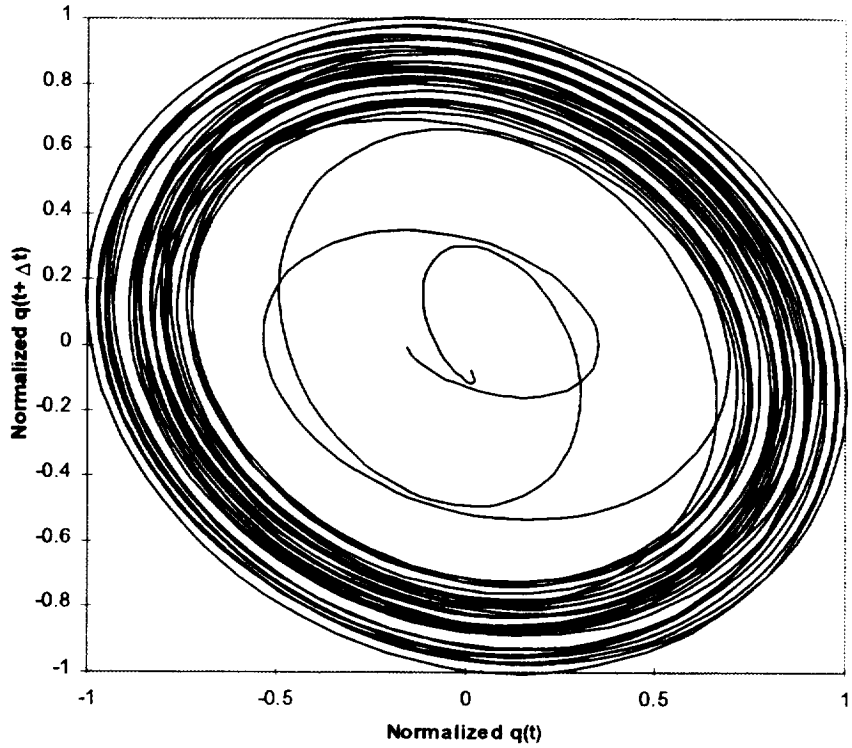

Figure 28E: Phase Trajectory for the Sixth Oscillation, Chamber Diameter 1.0 cm, Aspect Ratio 1.0, Bond Number 2.94 Case

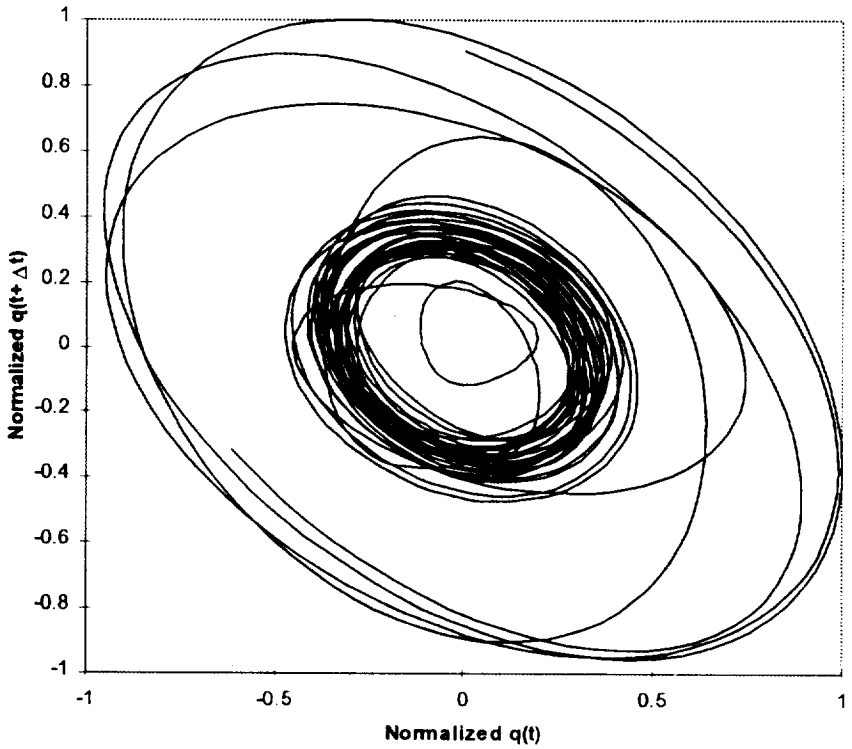

Figure 28F: Phase Trajectory for the Seventh Oscillation, Chamber Diameter 1.0 cm, Aspect Ratio 1.0, Bond Number 2.94 Case

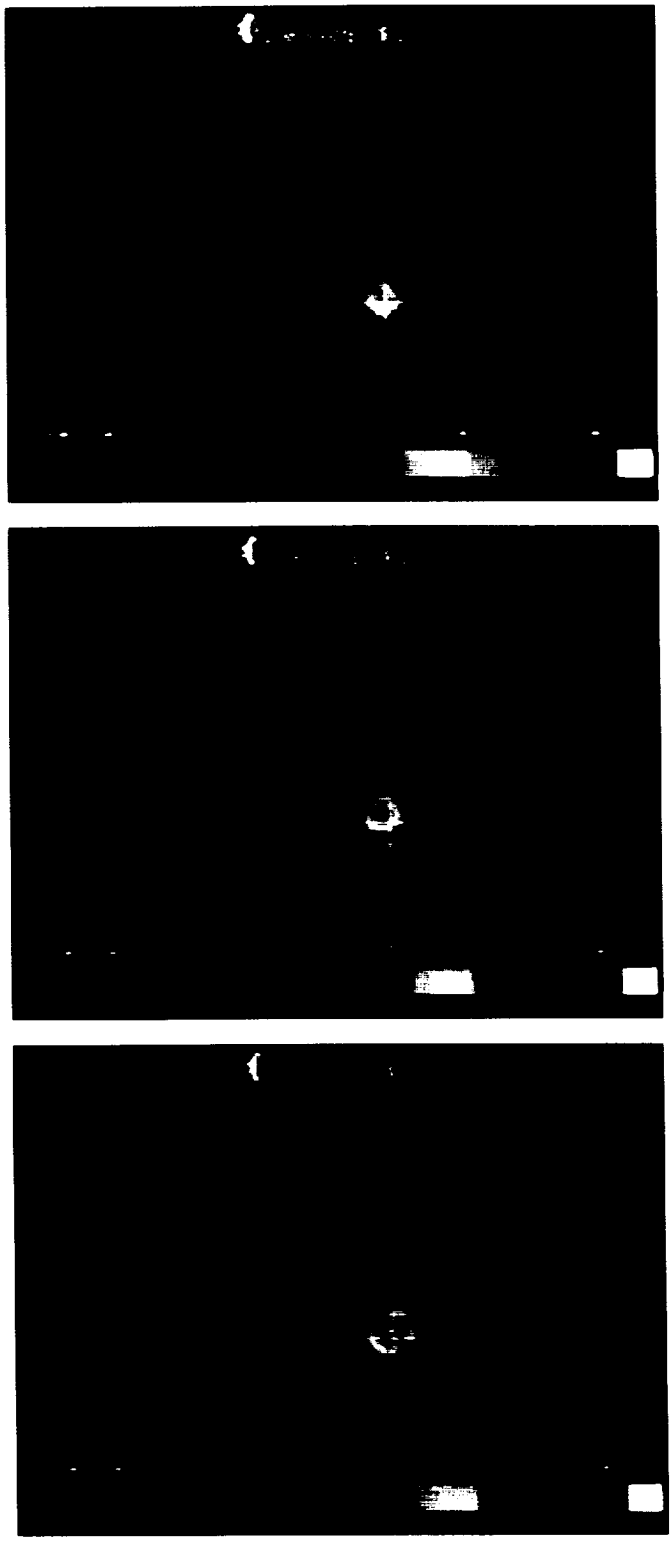

Figure 31: Chaotic Motion, Diameter 0.5 cm,
Aspect Ratio 2.0, Bond Number 5.88

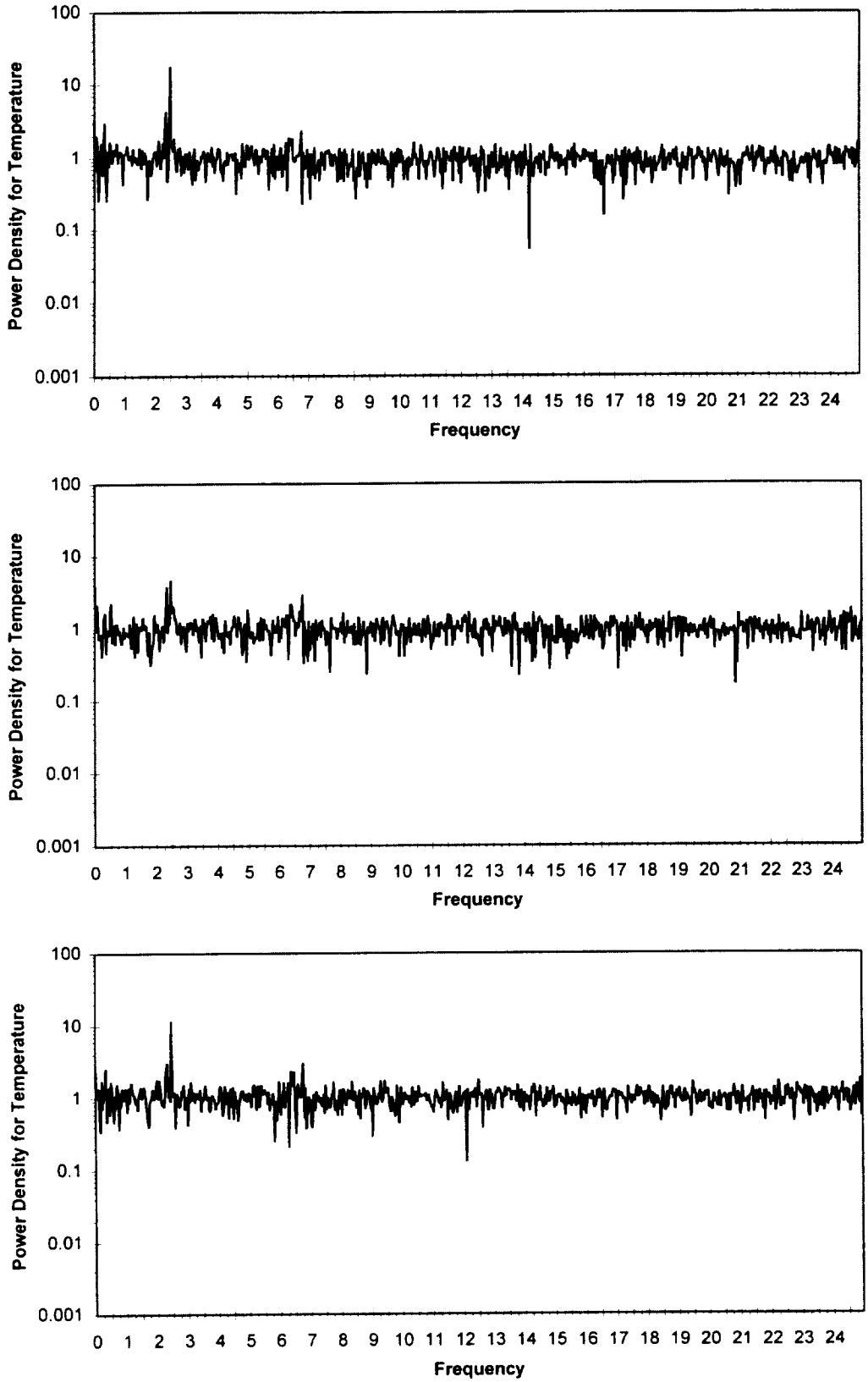

Figure 32: Power Spectrums for the Second Observed Oscillation of the Diameter 0.5, Aspect Ratio 2.0, Bond Number 5.88 Case

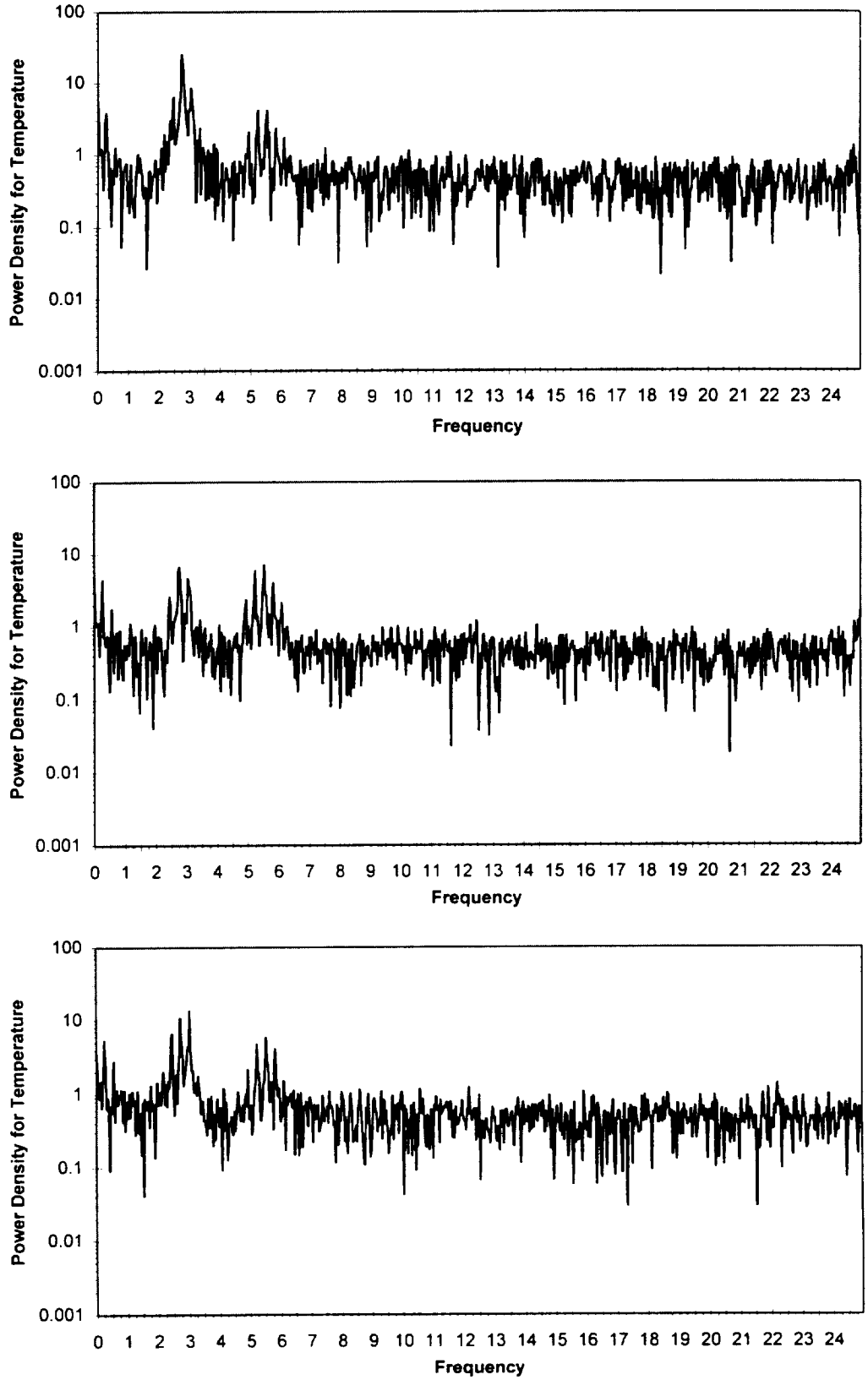

Figure 33: Power Spectrums for the Third Observed Oscillation of the Diameter 0.5, Aspect Ratio 2.0, Bond Number 5.88 Case

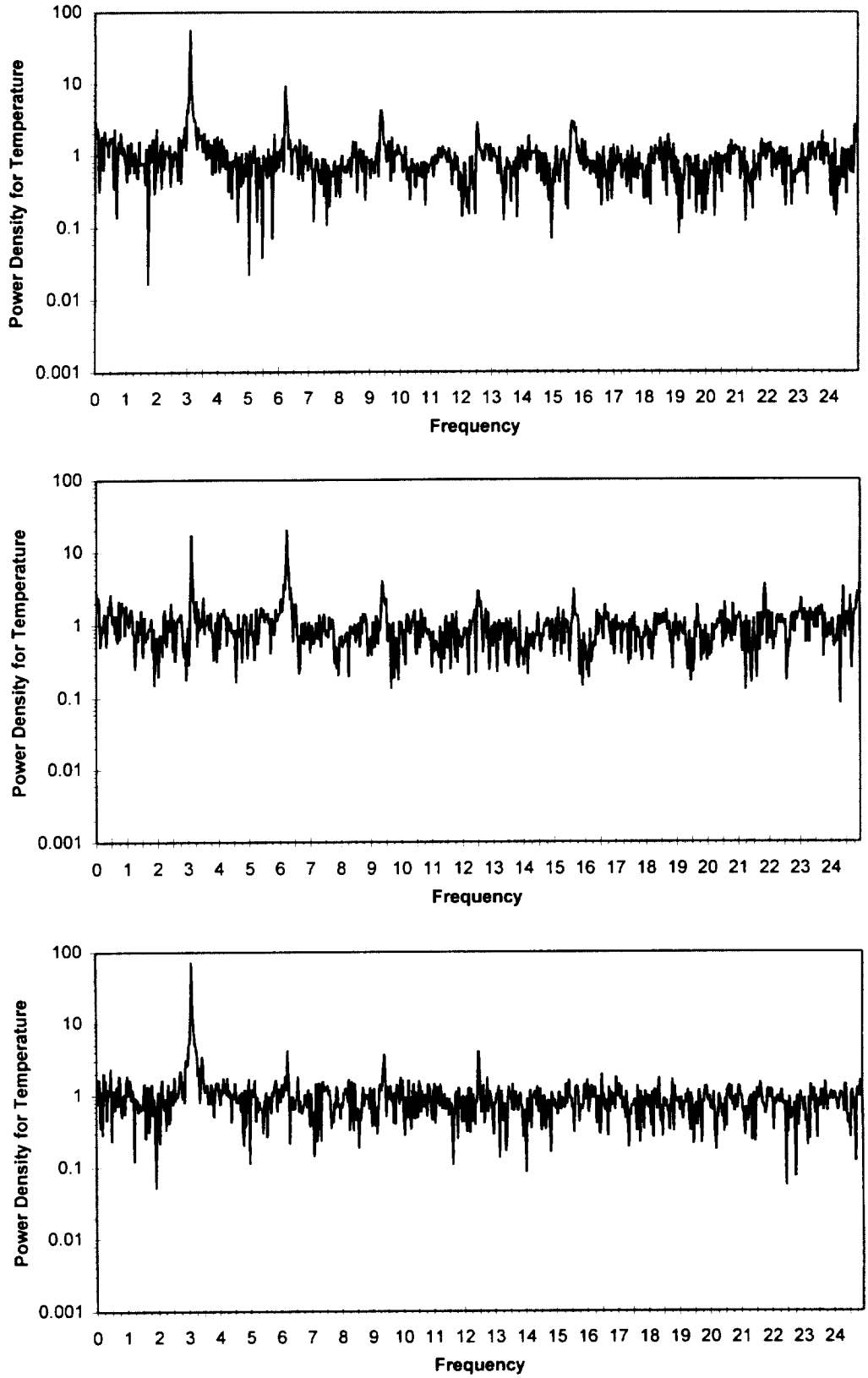

Figure 34: Power Spectrums for the Fourth Observed Oscillation of the Diameter 0.5, Aspect Ratio 2.0, Bond Number 5.88 Case

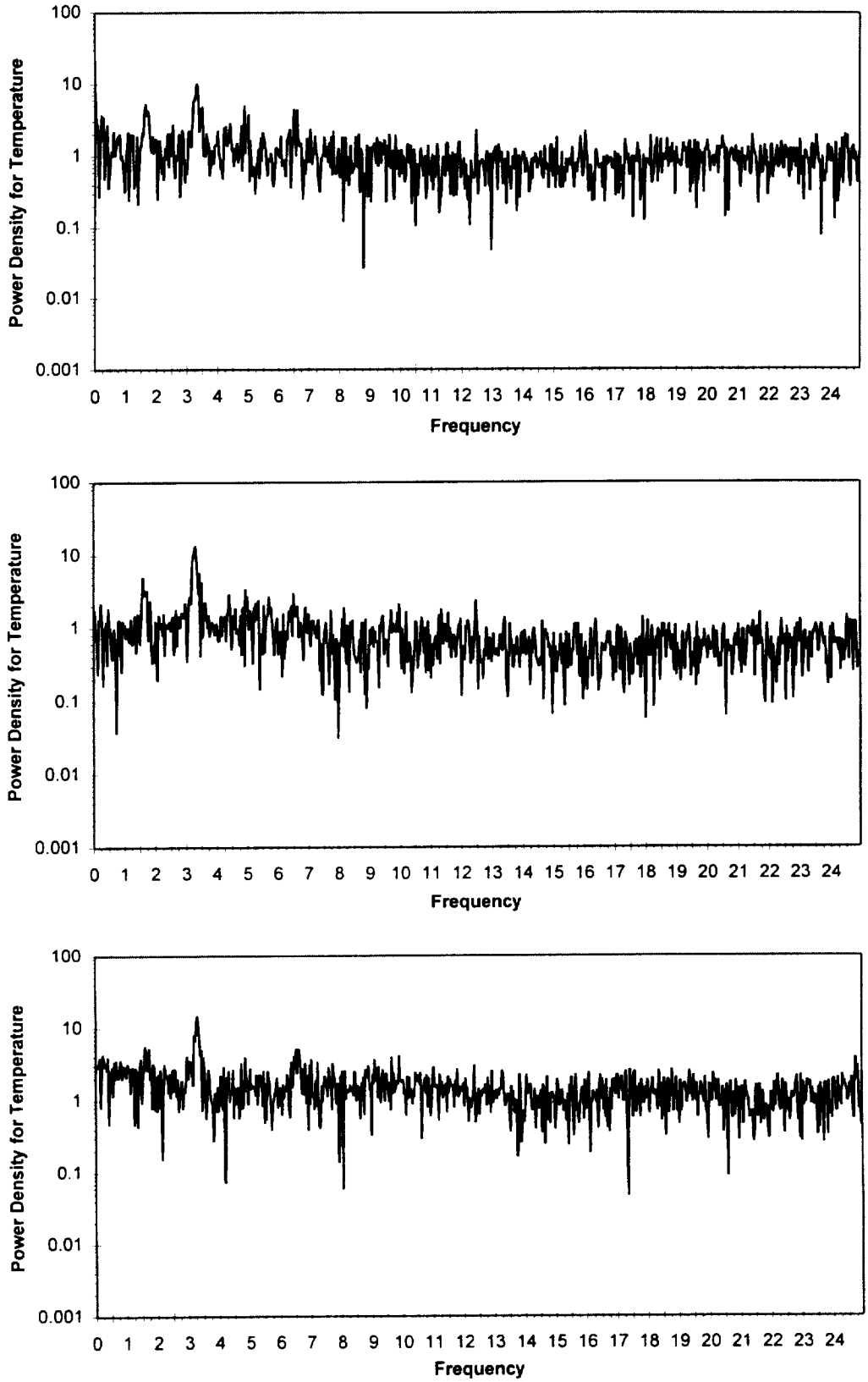

Figure 35: Power Spectrums for the Fifth Observed Oscillation of the Diameter 0.5, Aspect Ratio 2.0, Bond Number 5.88 Case

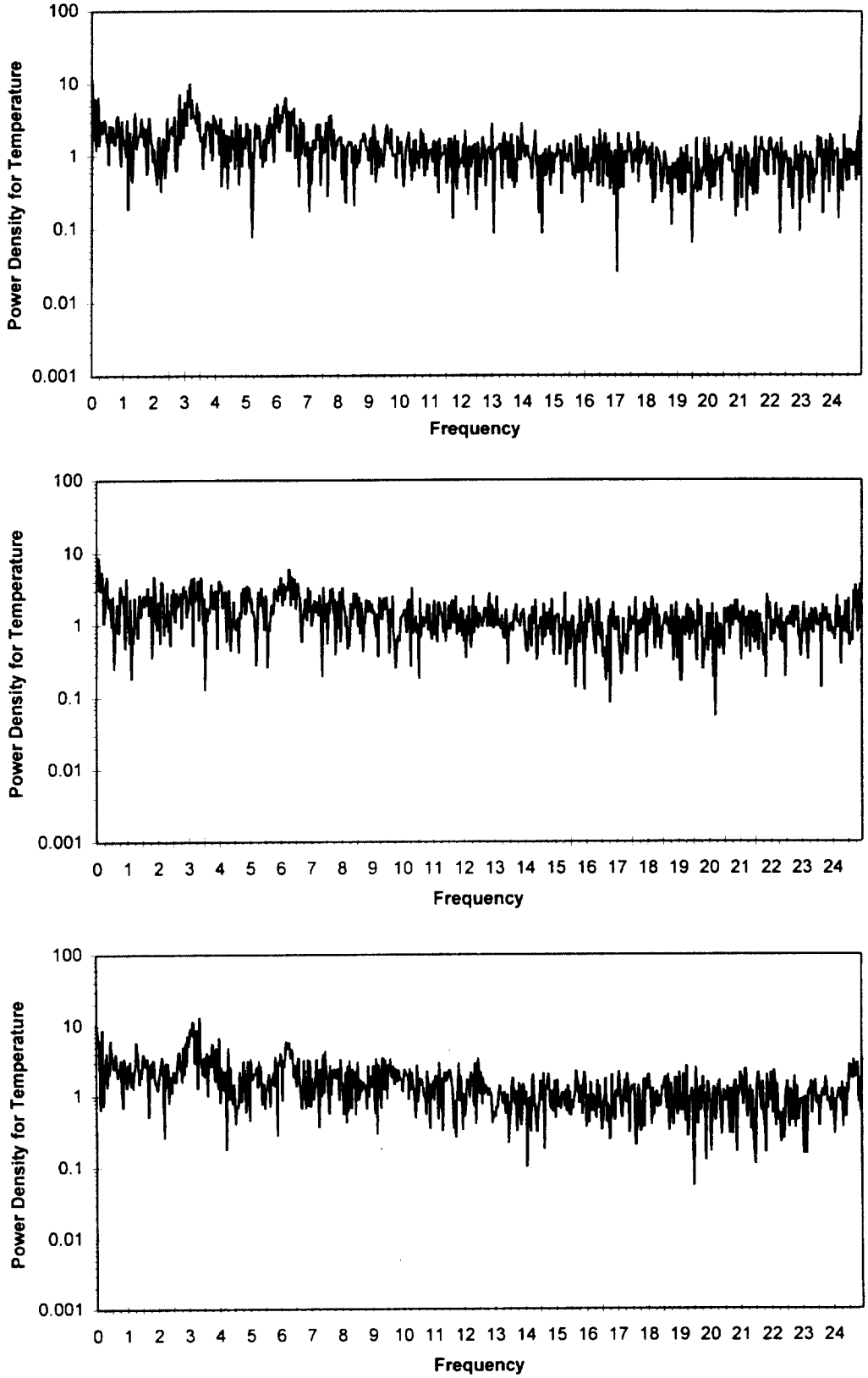

Figure 36: Power Spectrums for the Sixth Observed Oscillation of the Diameter 0.5, Aspect Ratio 2.0, Bond Number 5.88 Case

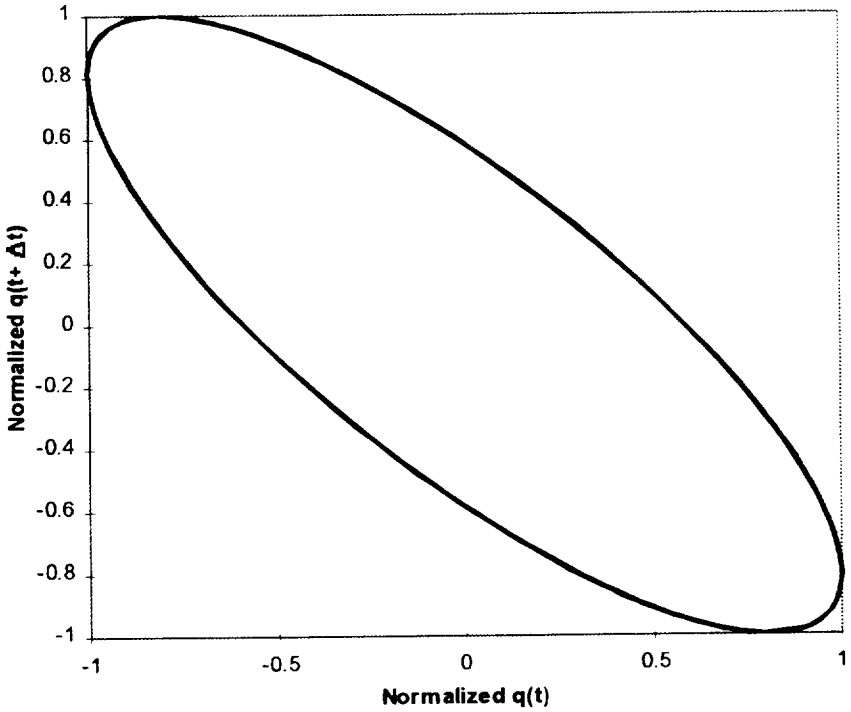

Figure 37A: Phase Trajectory for the Second Oscillation, Chamber Diameter 0.5 cm, Aspect Ratio 2.0, Bond Number 5.88 Case

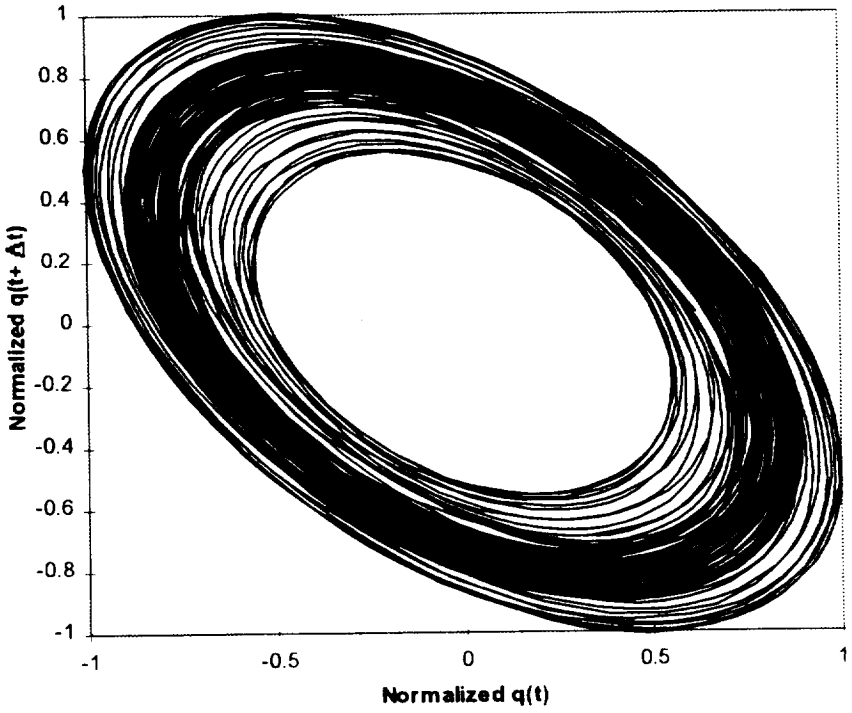

Figure 37B: Phase Trajectory for the Third Oscillation, Chamber Diameter 0.5 cm, Aspect Ratio 2.0, Bond Number 5.88 Case

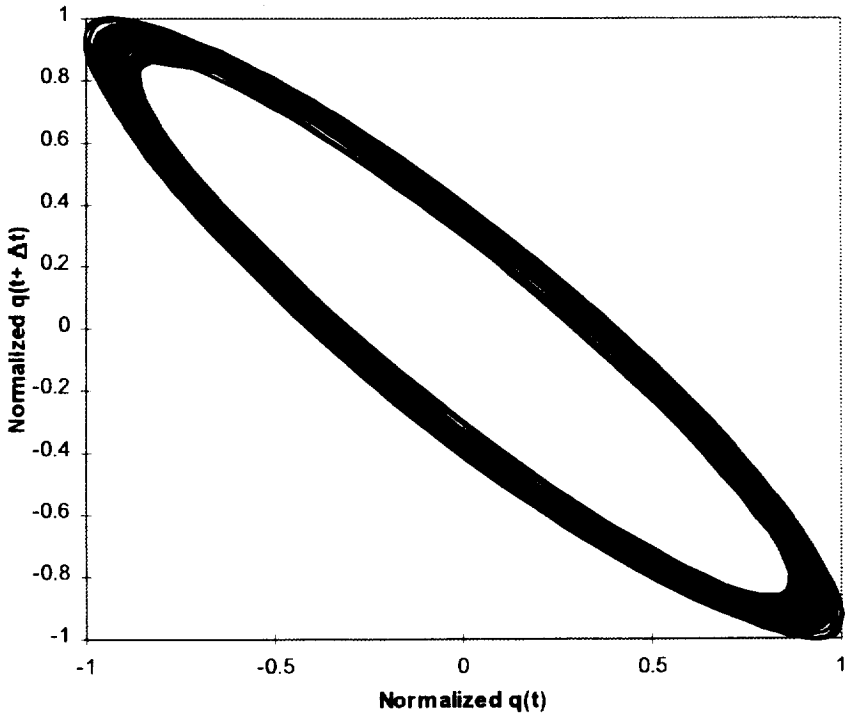

Figure 37C: Phase Trajectory for the Fourth Oscillation, Chamber Diameter 0.5 cm, Aspect Ratio 2.0, Bond Number 5.88 Case

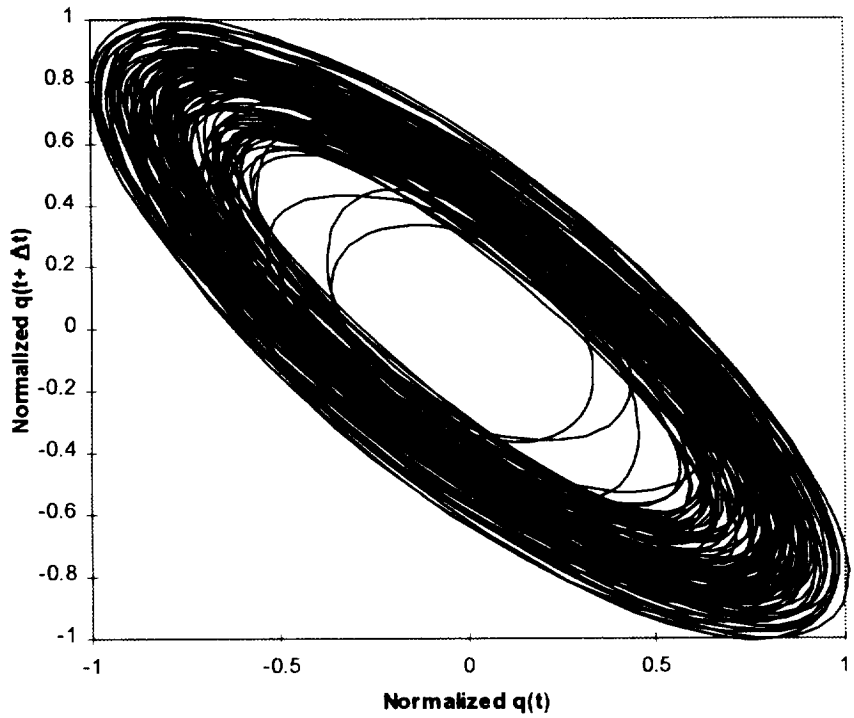

Figure 37C: Phase Trajectory for the Fifth Oscillation, Chamber Diameter 0.5 cm, Aspect Ratio 2.0, Bond Number 5.88 Case

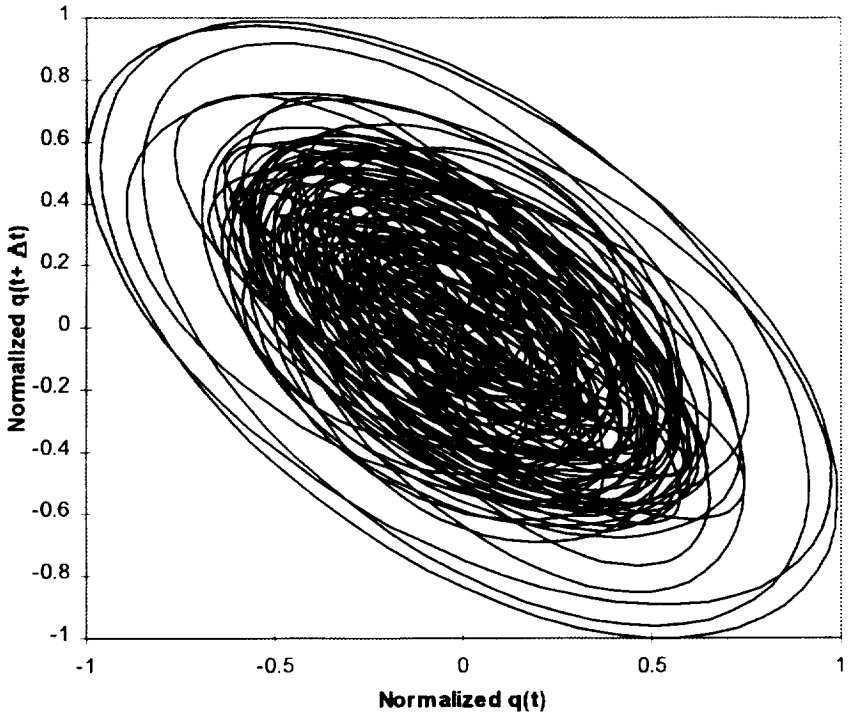

Figure 37C: Phase Trajectory for the Sixth Oscillation, Chamber Diameter 0.5 cm, Aspect Ratio 2.0, Bond Number 5.88 Case

X. Appendices

1. Power Spectra for the 0.5 cm Diameter Test Chamber

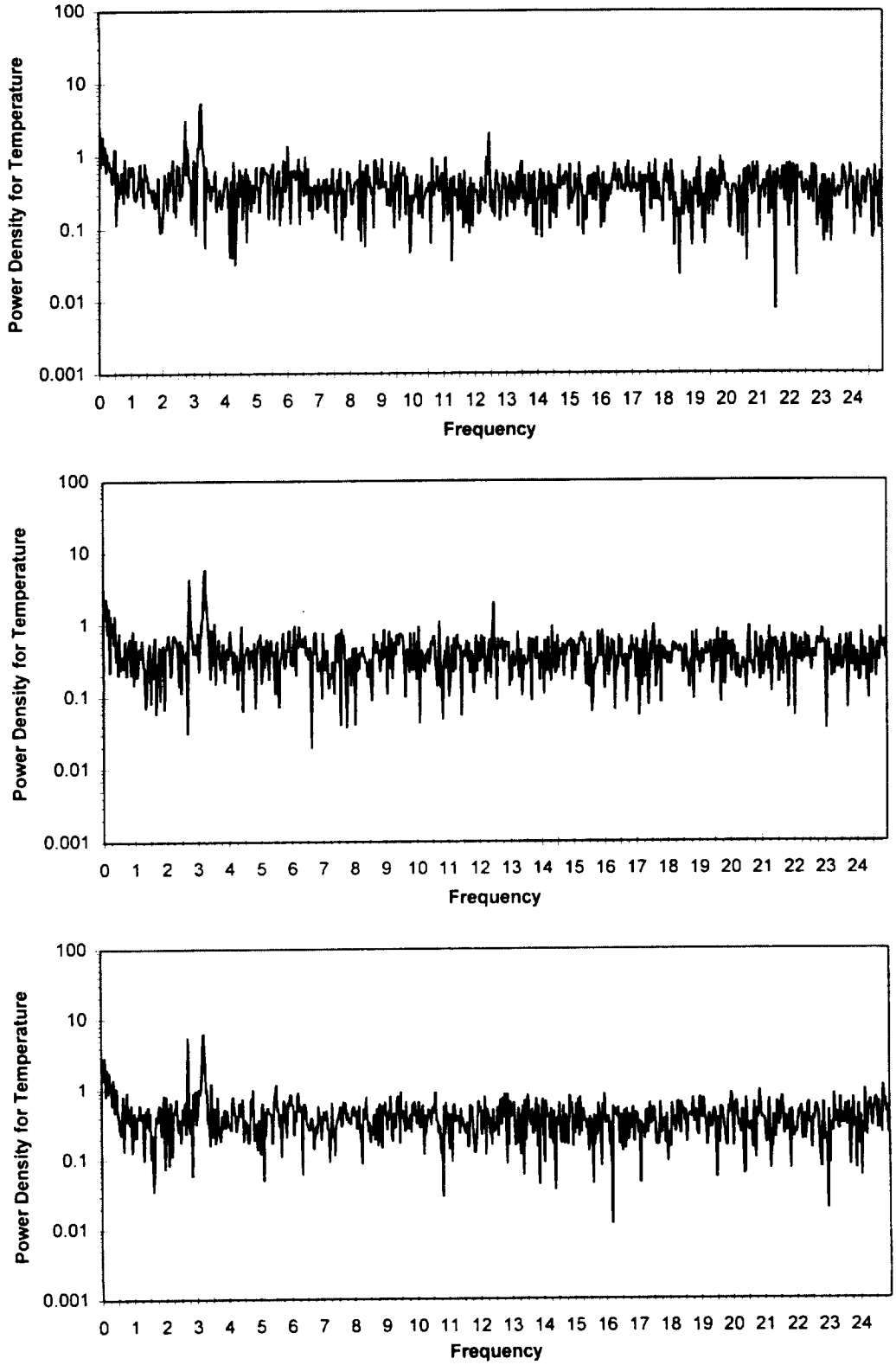

Power Spectrums for the Second Observed Oscillation of the Diameter 0.5, Aspect Ratio 1.0, Bond Number 0.74 Case

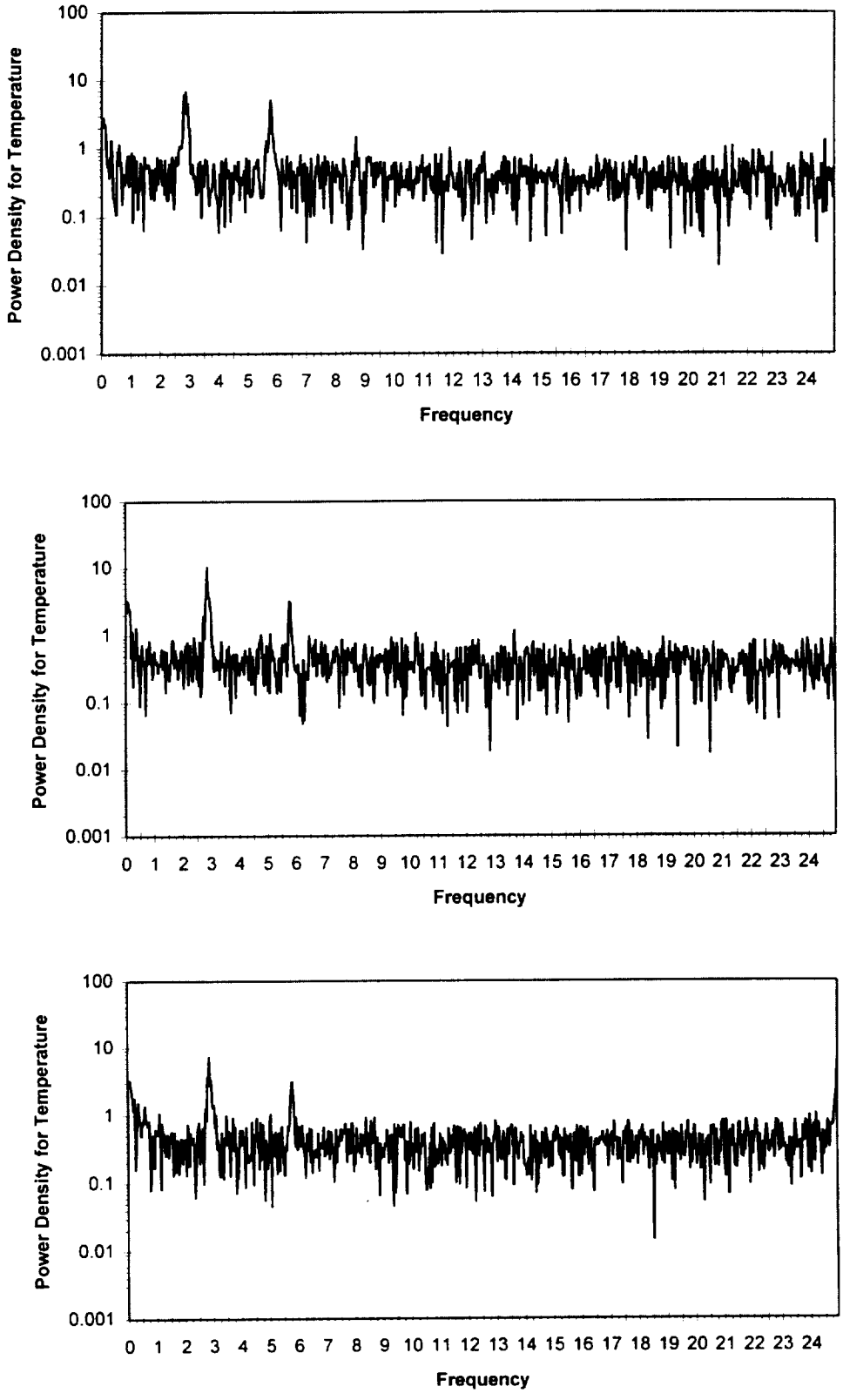

Power Spectrums for the Third Observed Oscillation of the Diameter 0.5, Aspect Ratio 1.0, Bond Number 0.74 Case

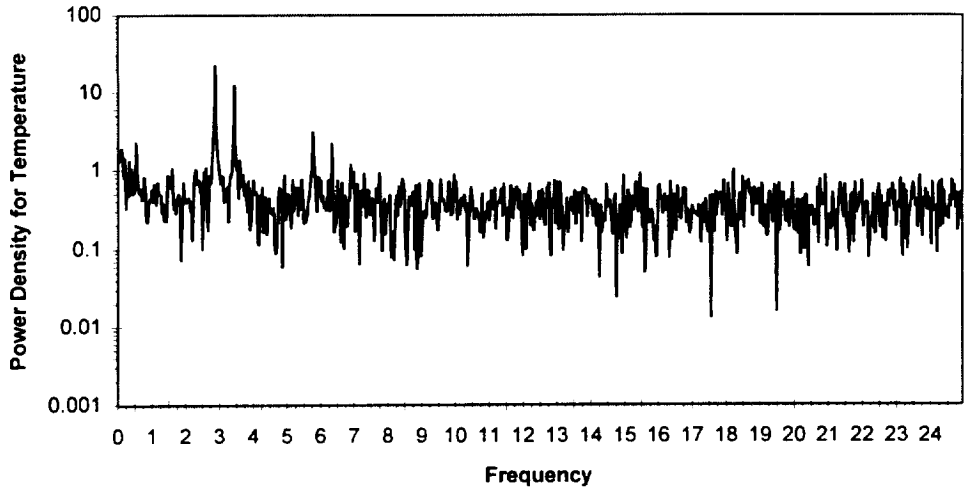

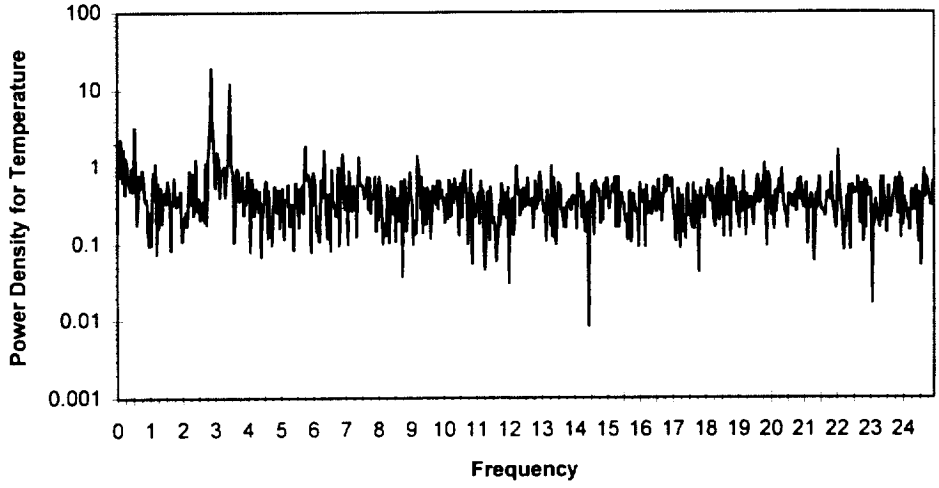

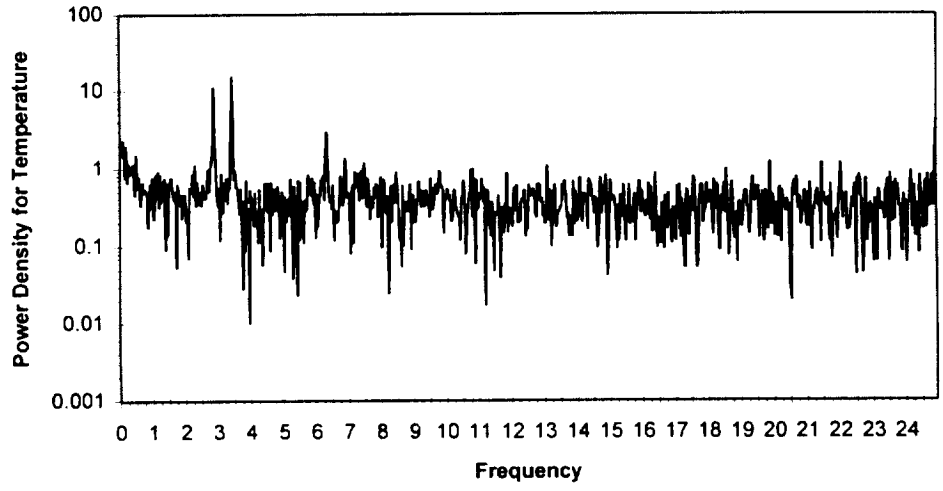

Power Spectrums for the Fourth Observed Oscillation of the Diameter 0.5, Aspect Ratio 1.0, Bond Number 0.74 Case

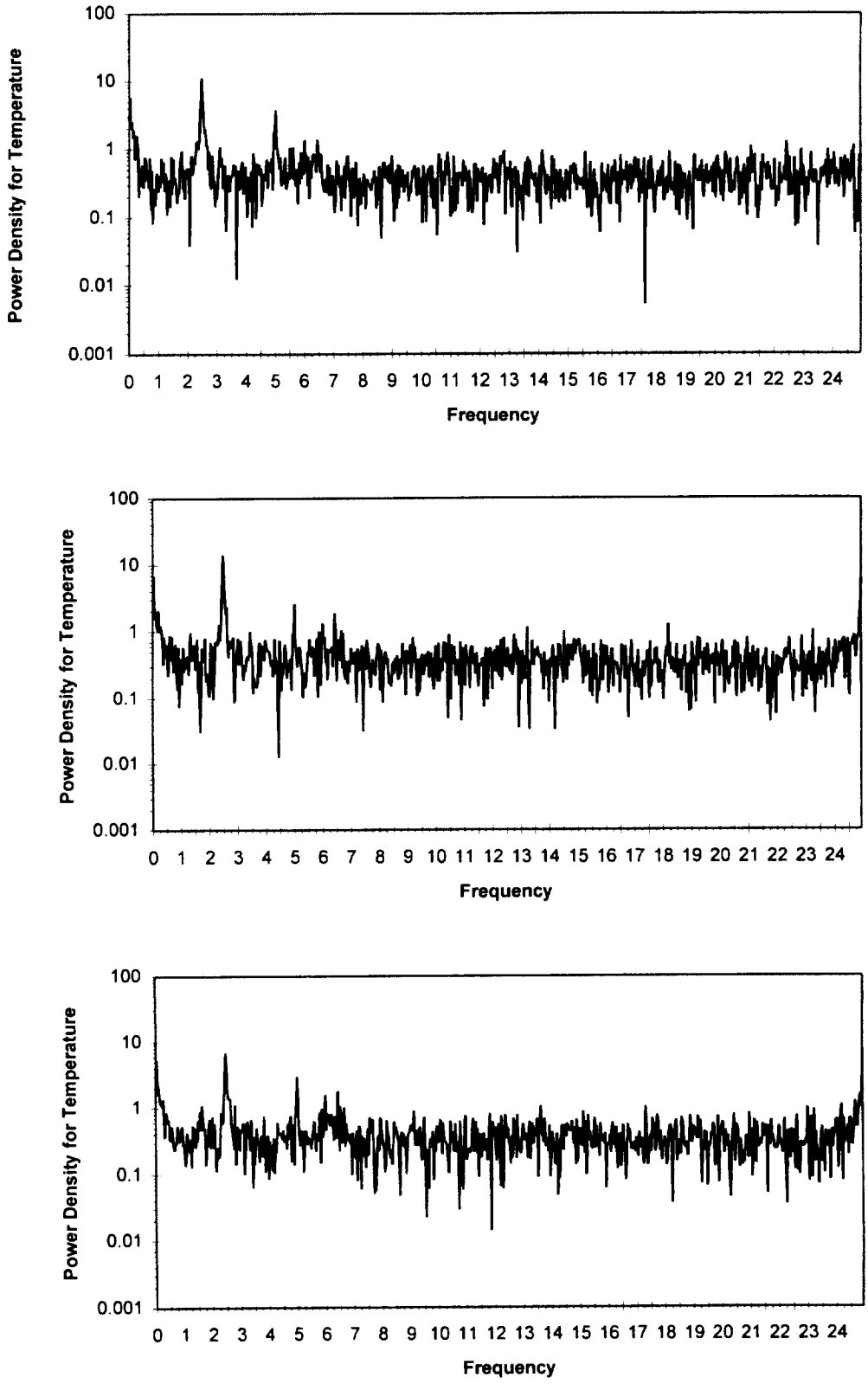

Power Spectrums for the Second Observed Oscillation of the Diameter 0.5, Aspect Ratio 1.5, Bond Number 2.84 Case

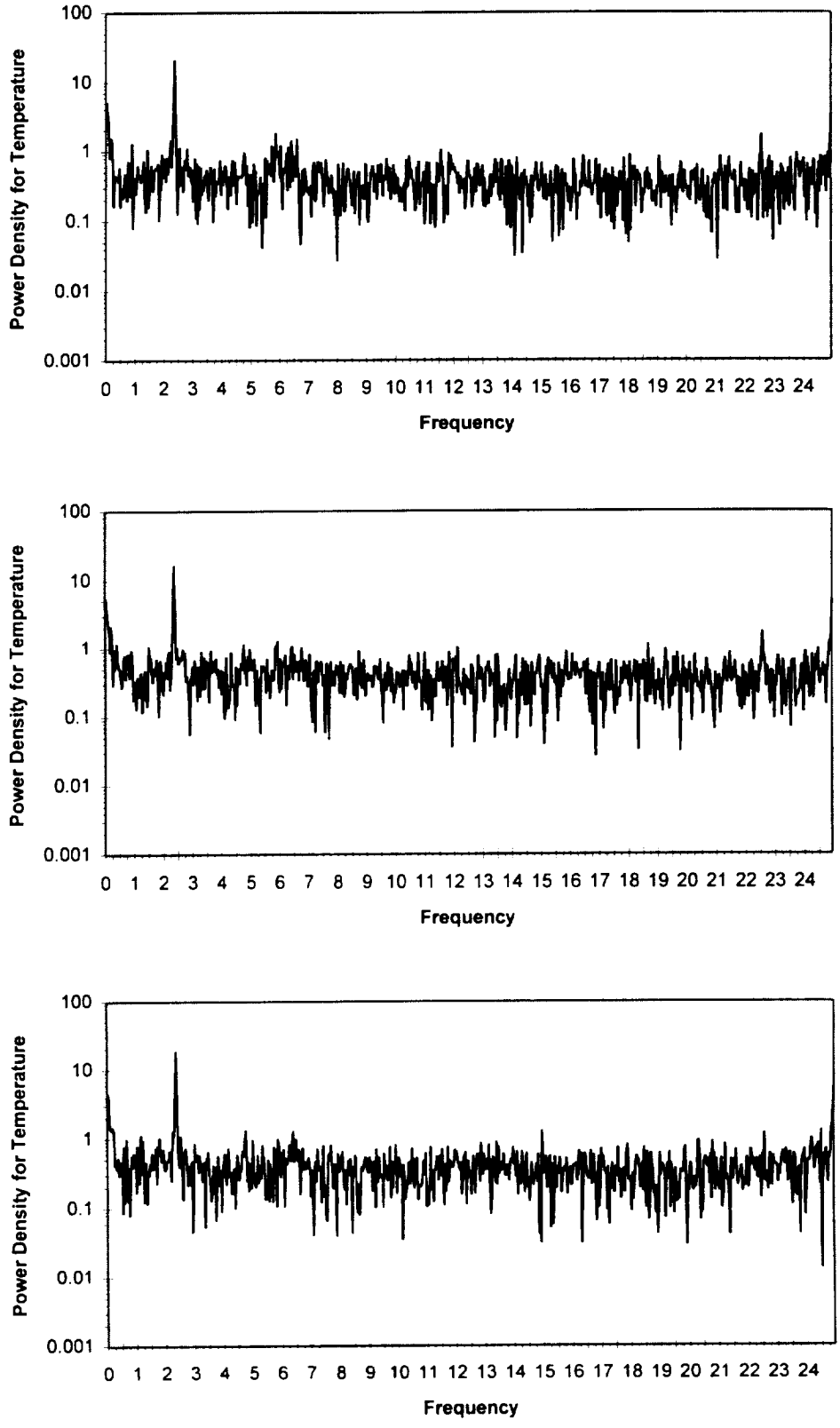

Power Spectrums for the Third Observed Oscillation of the Diameter 0.5, Aspect Ratio 1.5, Bond Number 2.84 Case

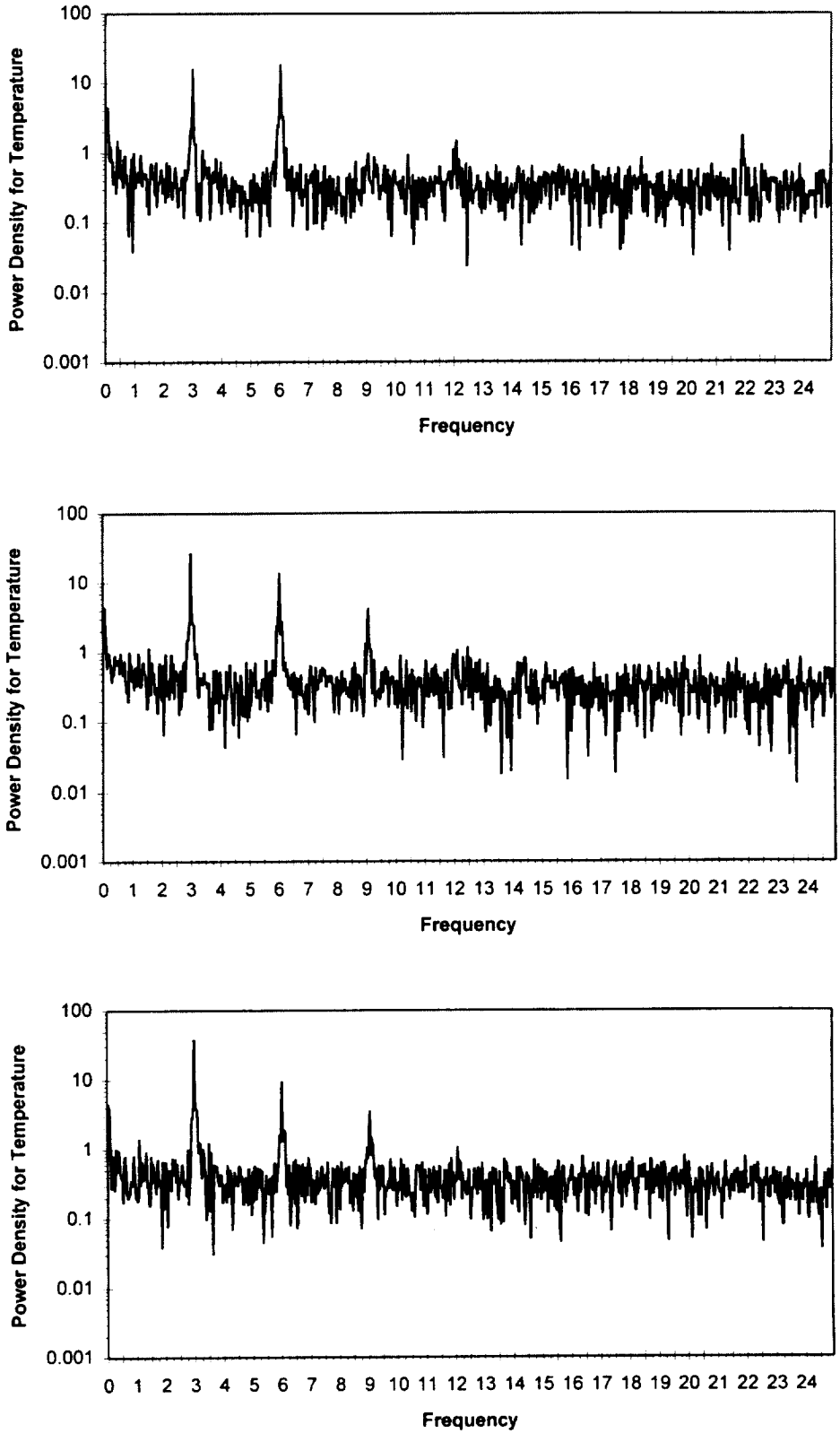

Power Spectrums for the Fourth Observed Oscillation of the Diameter 0.5, Aspect Ratio 1.5, Bond Number 2.84 Case

2. Power Spectra for the 1.0 cm Diameter Test Chamber

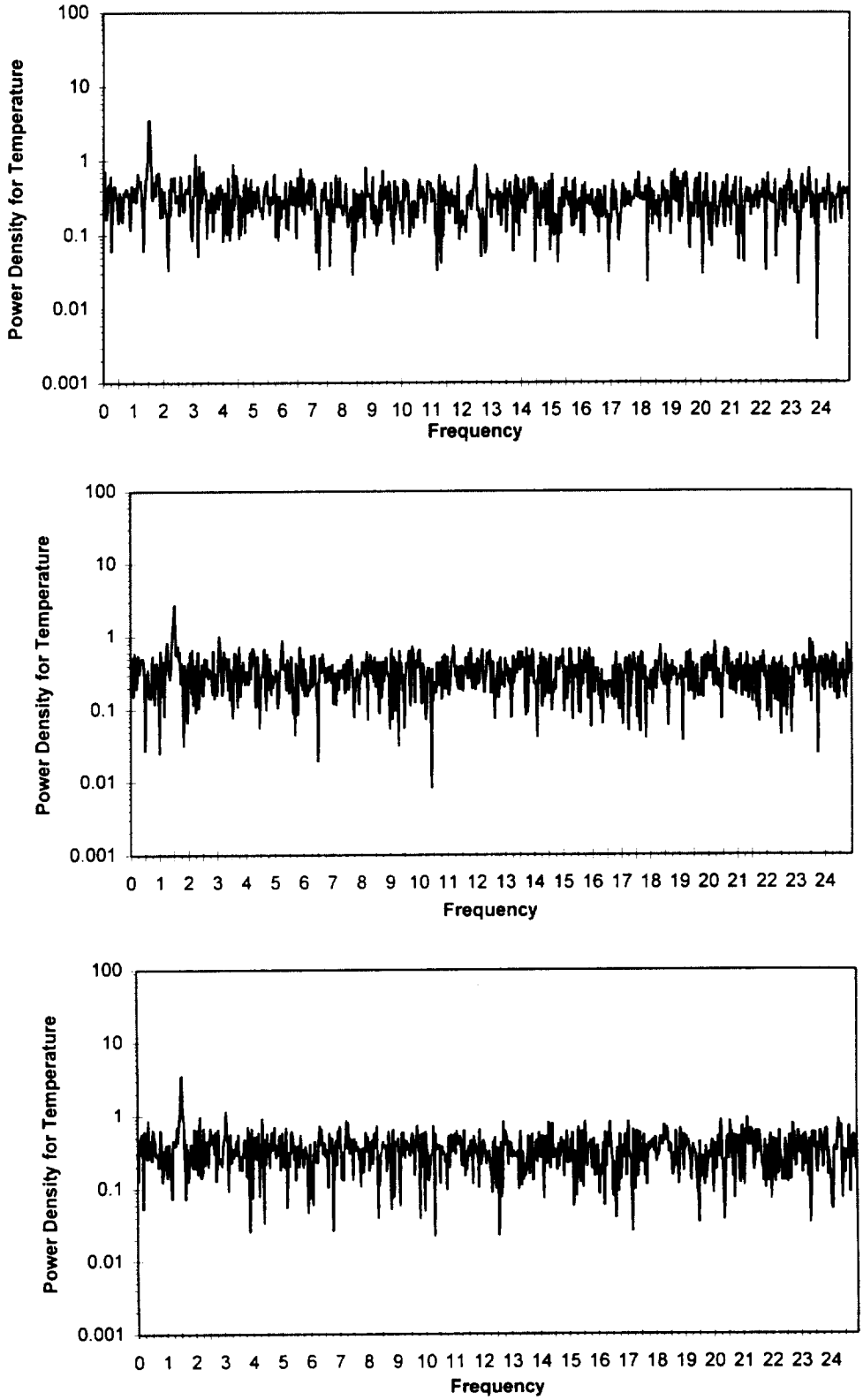

Power Spectrums for the Second Observed Oscillation of the Diameter 1.0, Aspect Ratio 0.5, Bond Number 0.37 Case

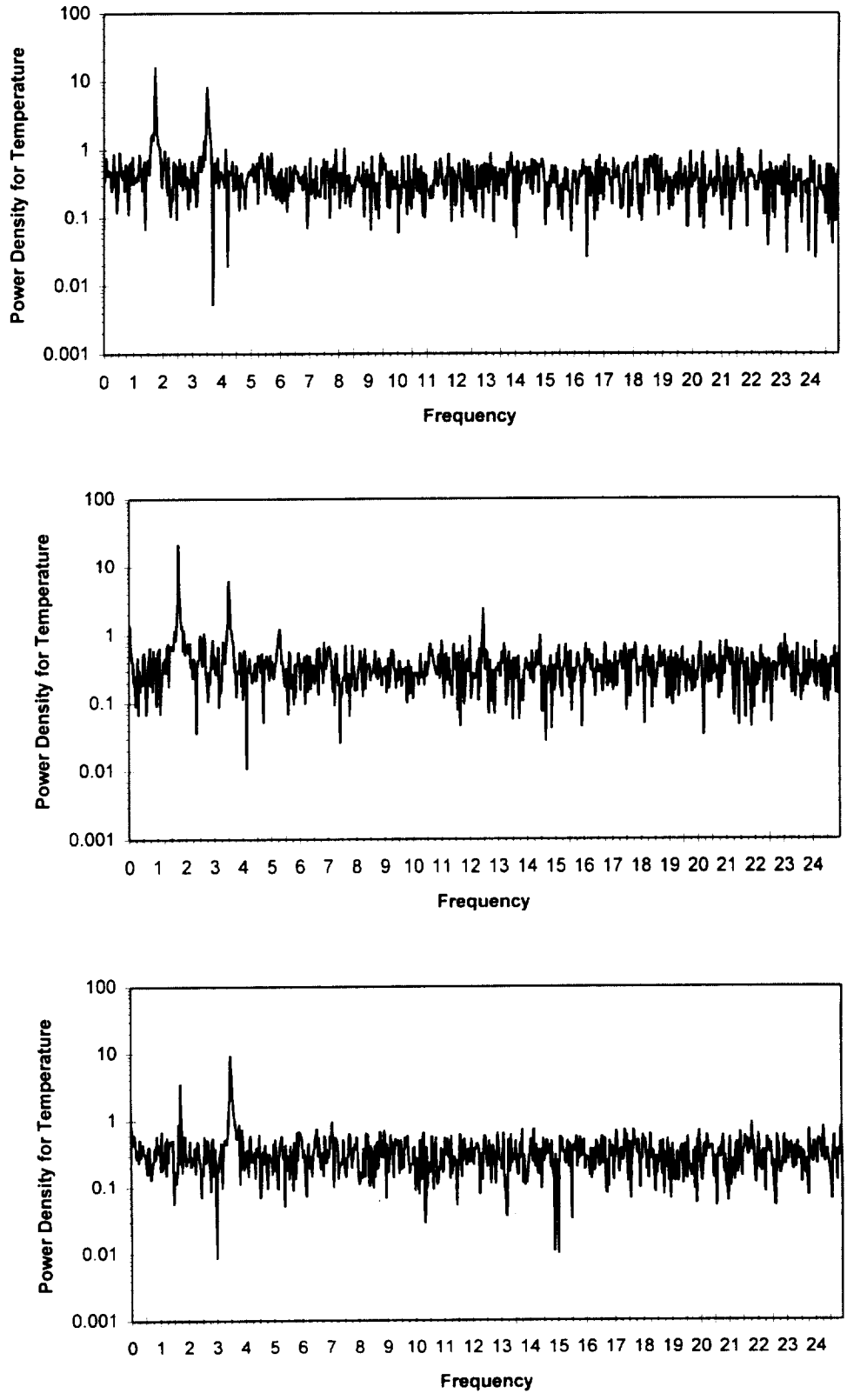

Power Spectrums for the Third Observed Oscillation of the Diameter 1.0, Aspect Ratio 0.5, Bond Number 0.37 Case

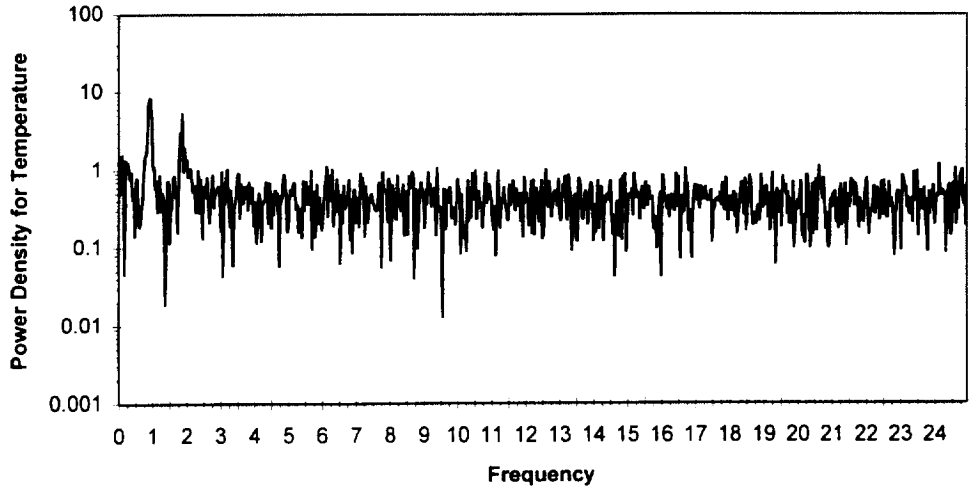

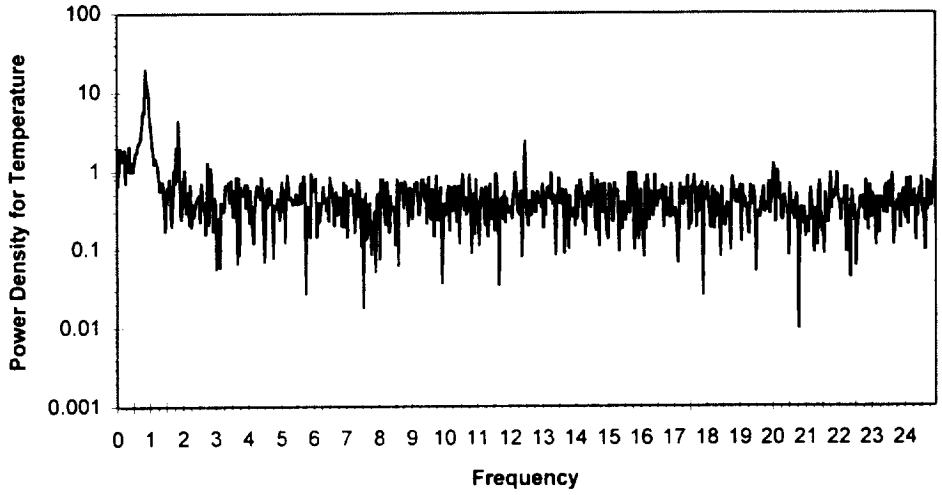

D=1.0cm, AR=1.5 Second Observed Oscillation: Angle = 180°

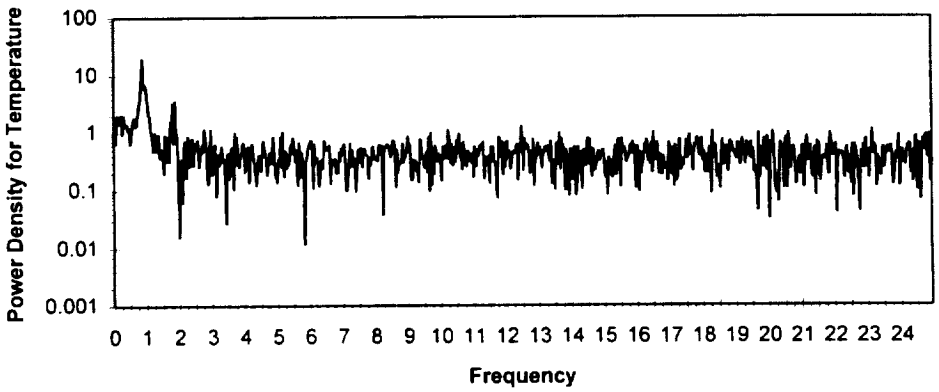

Power Spectrums for the Second Observed Oscillation of the Diameter 1.0, Aspect Ratio 1.5, Bond Number 9.92 Case

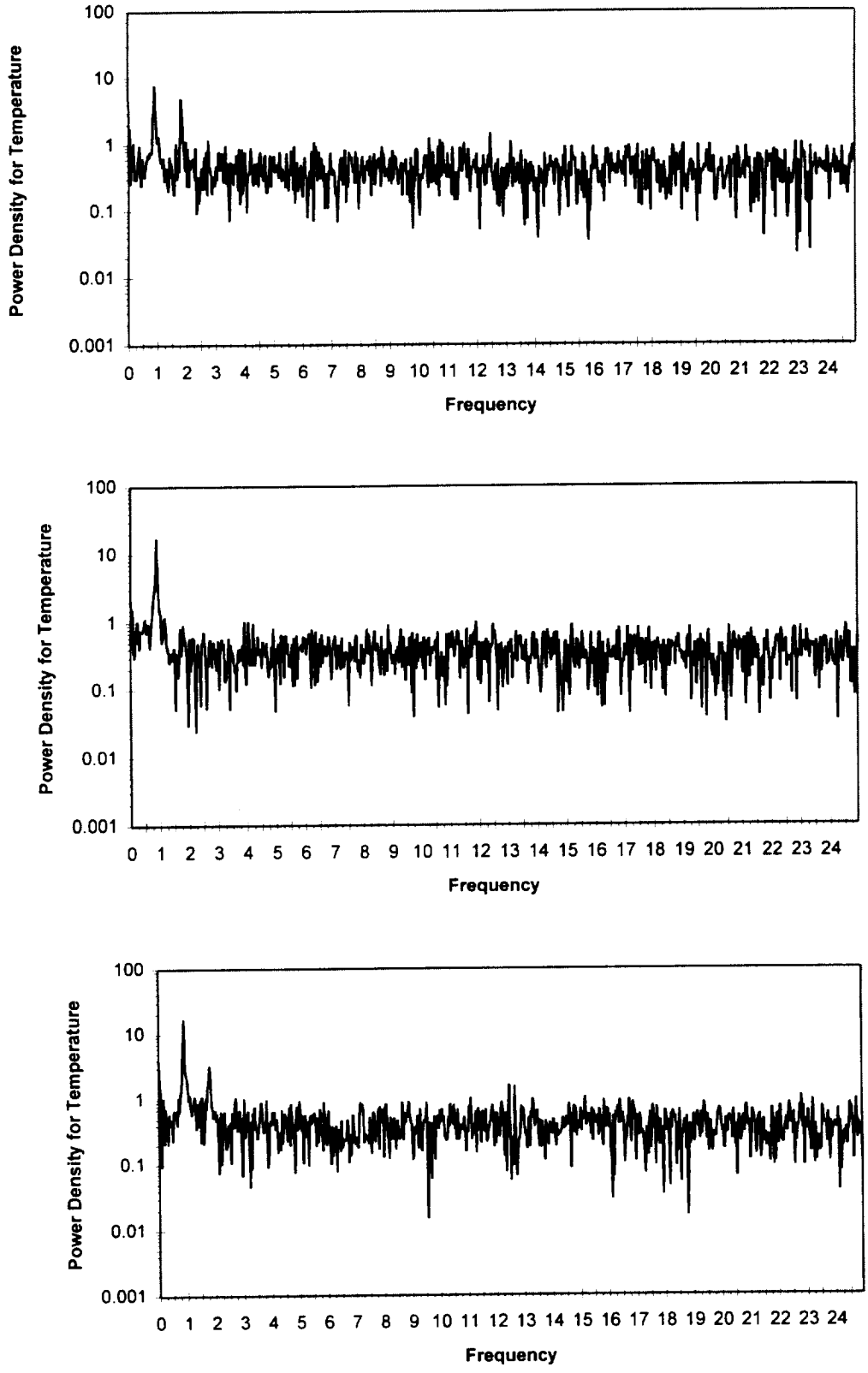

Power Spectrums for the Third Observed Oscillation of the Diameter 1.0, Aspect Ratio 1.5, Bond Number 9.92 Case

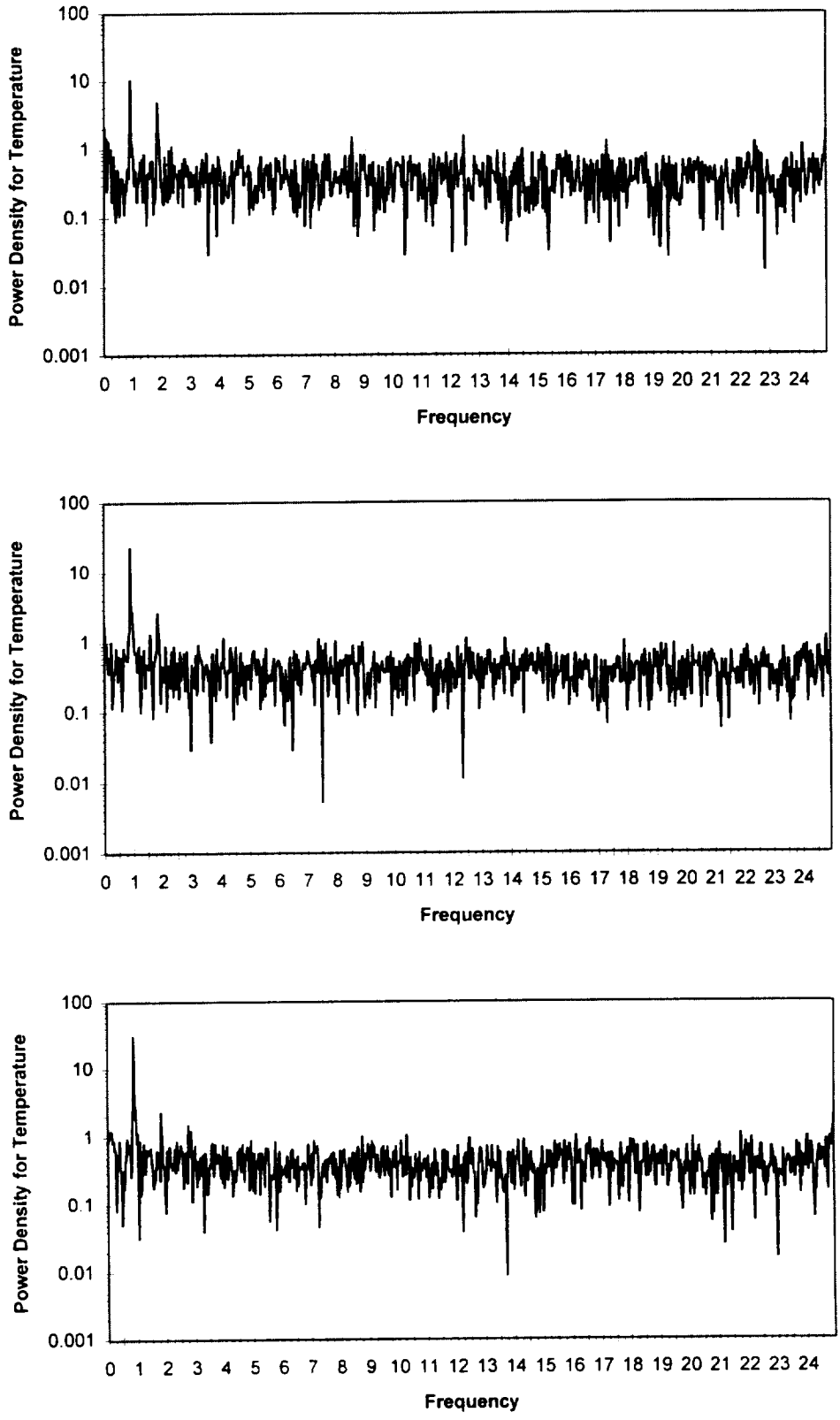

Power Spectrums for the Fourth Observed Oscillation of the Diameter 1.0, Aspect Ratio 1.5, Bond Number 9.92 Case

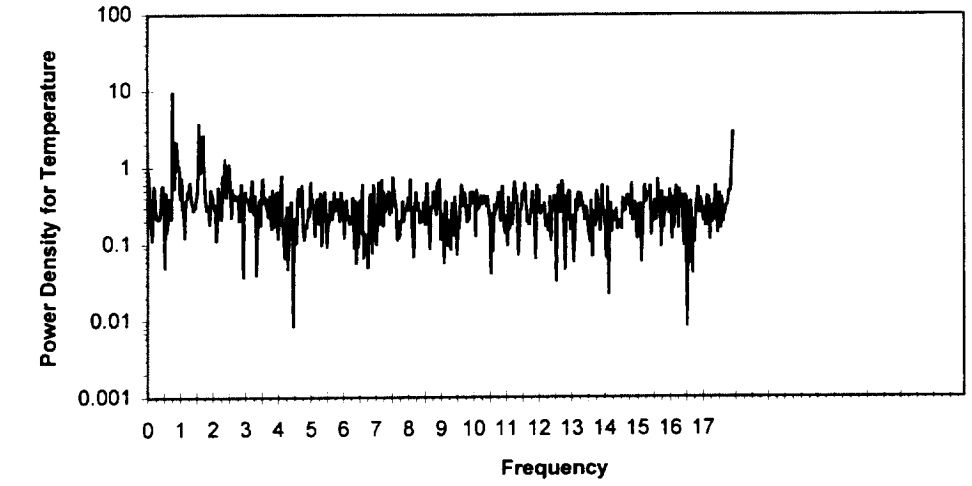

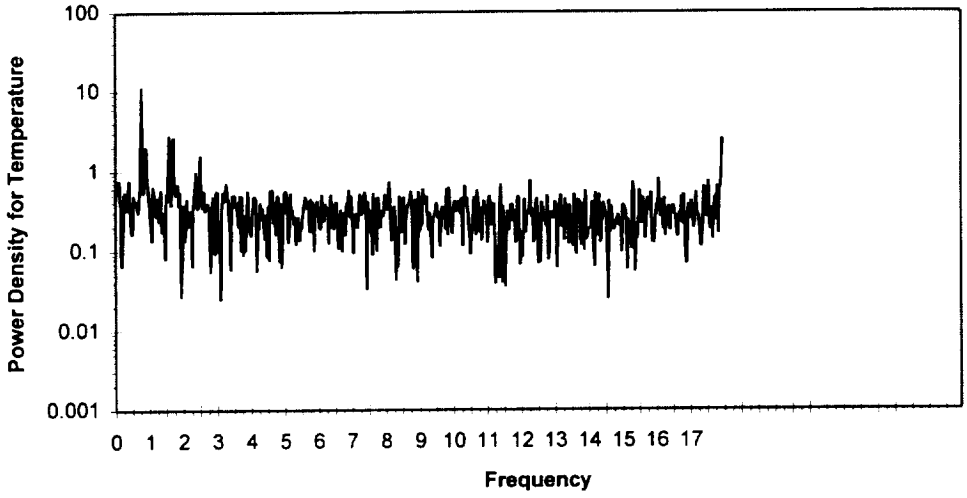

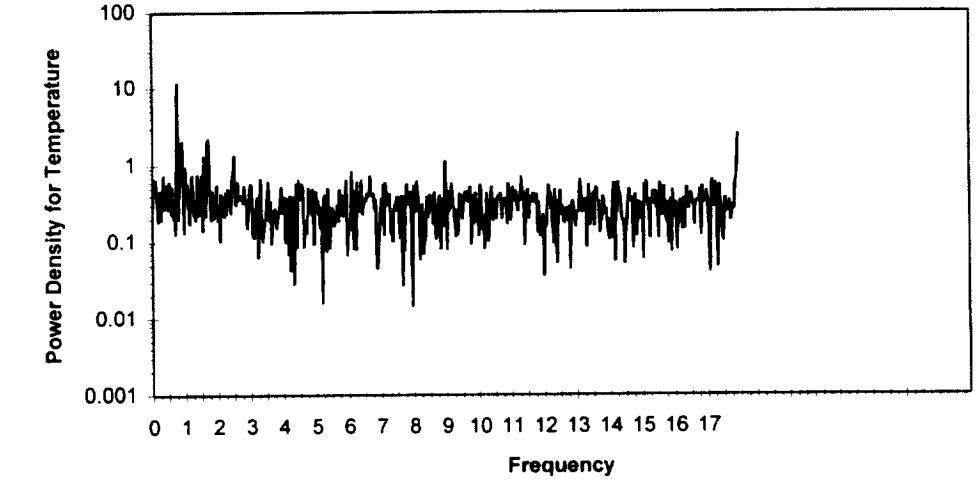

Power Spectrums for the Fifth Observed Oscillation of the Diameter 1.0, Aspect Ratio 1.5, Bond Number 9.92 Case

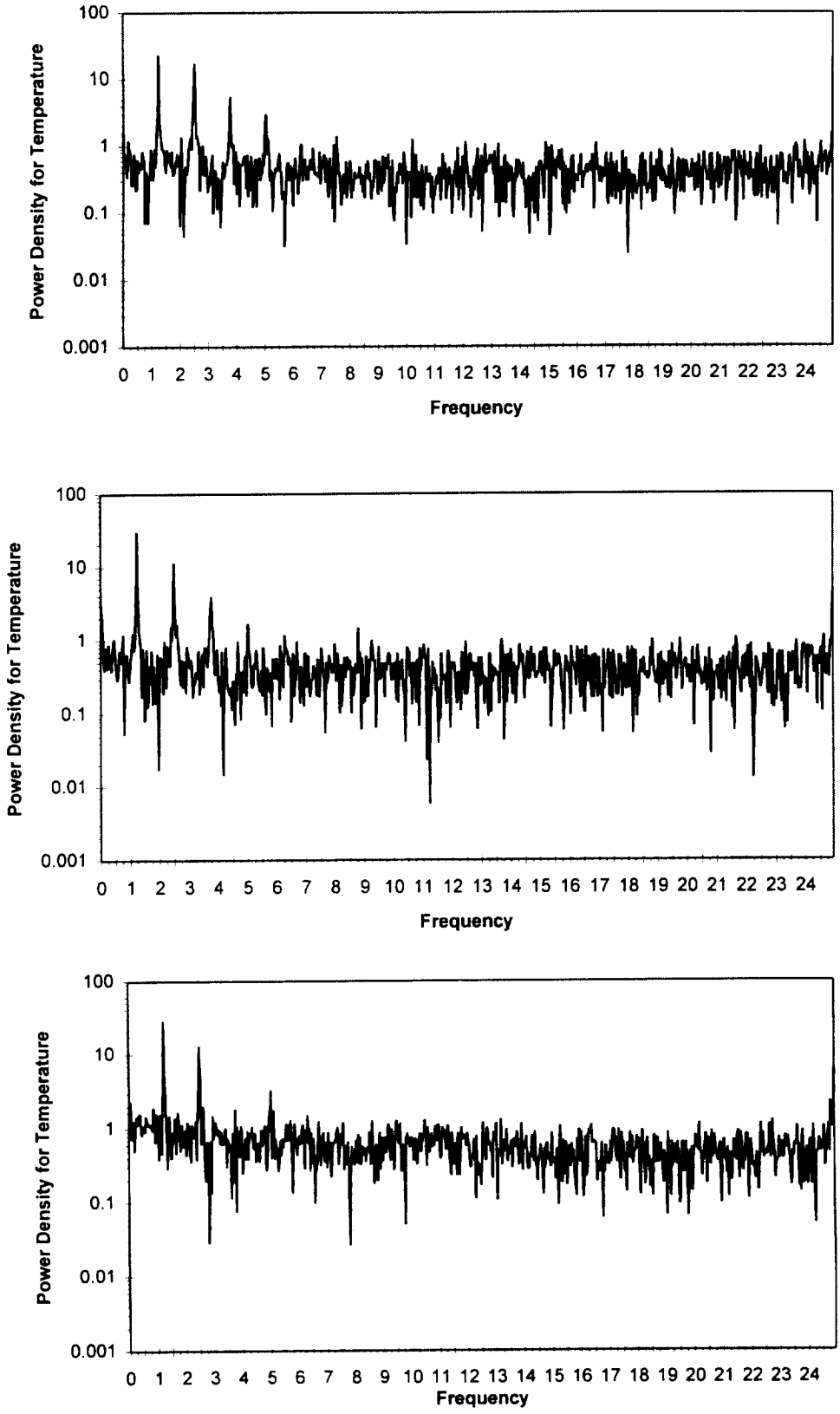

Power Spectrums for the Sixth Observed Oscillation of the Diameter 1.0, Aspect Ratio 1.5, Bond Number 9.92 Case

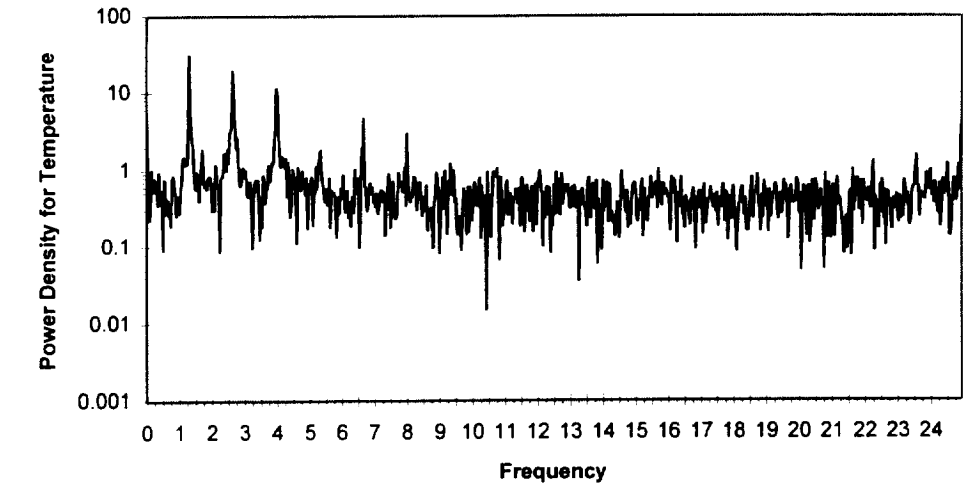

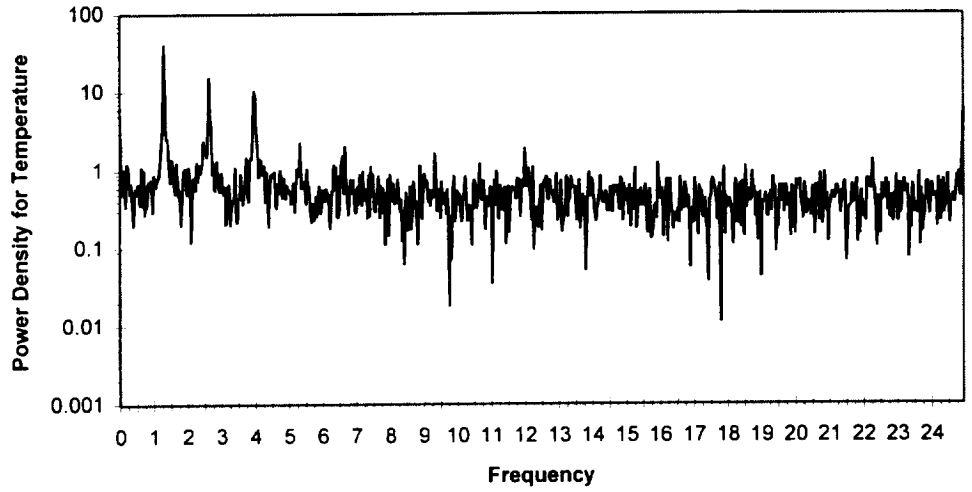

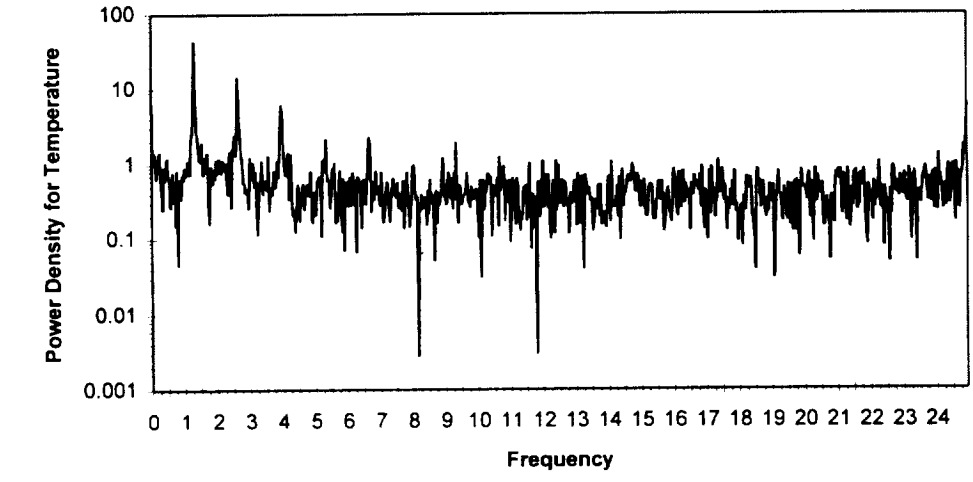

Power Spectrums for the Seventh Observed Oscillation of the Diameter 1.0, Aspect Ratio 1.5, Bond Number 9.92 Case

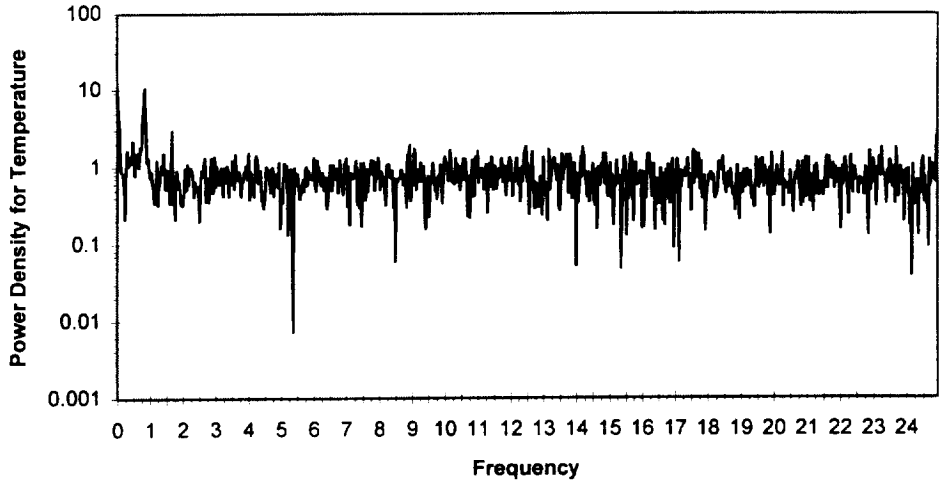

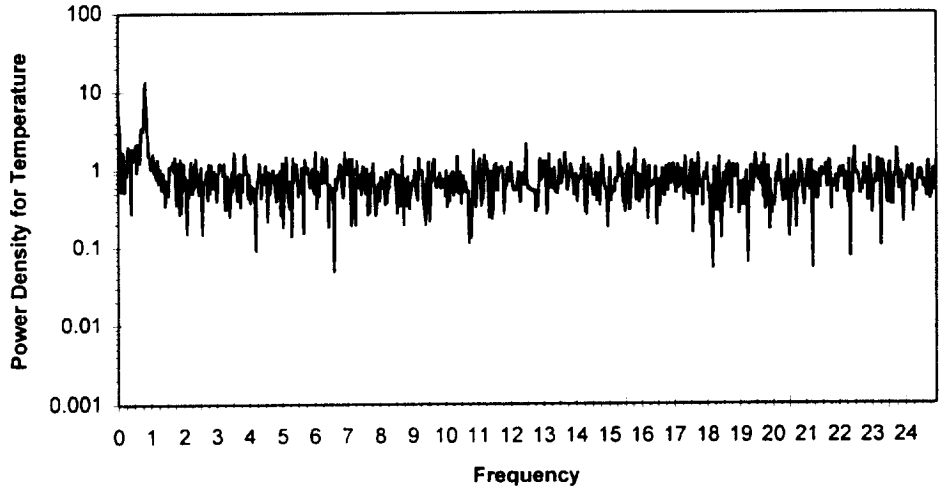

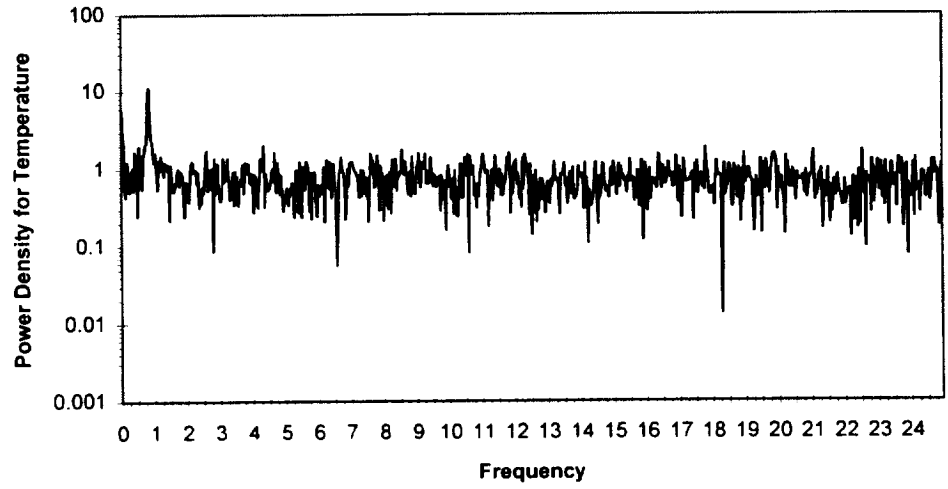

Power Spectrums for the Second Observed Oscillation of the Diameter 1.0, Aspect Ratio 2.0, Bond Number 23.5 Case

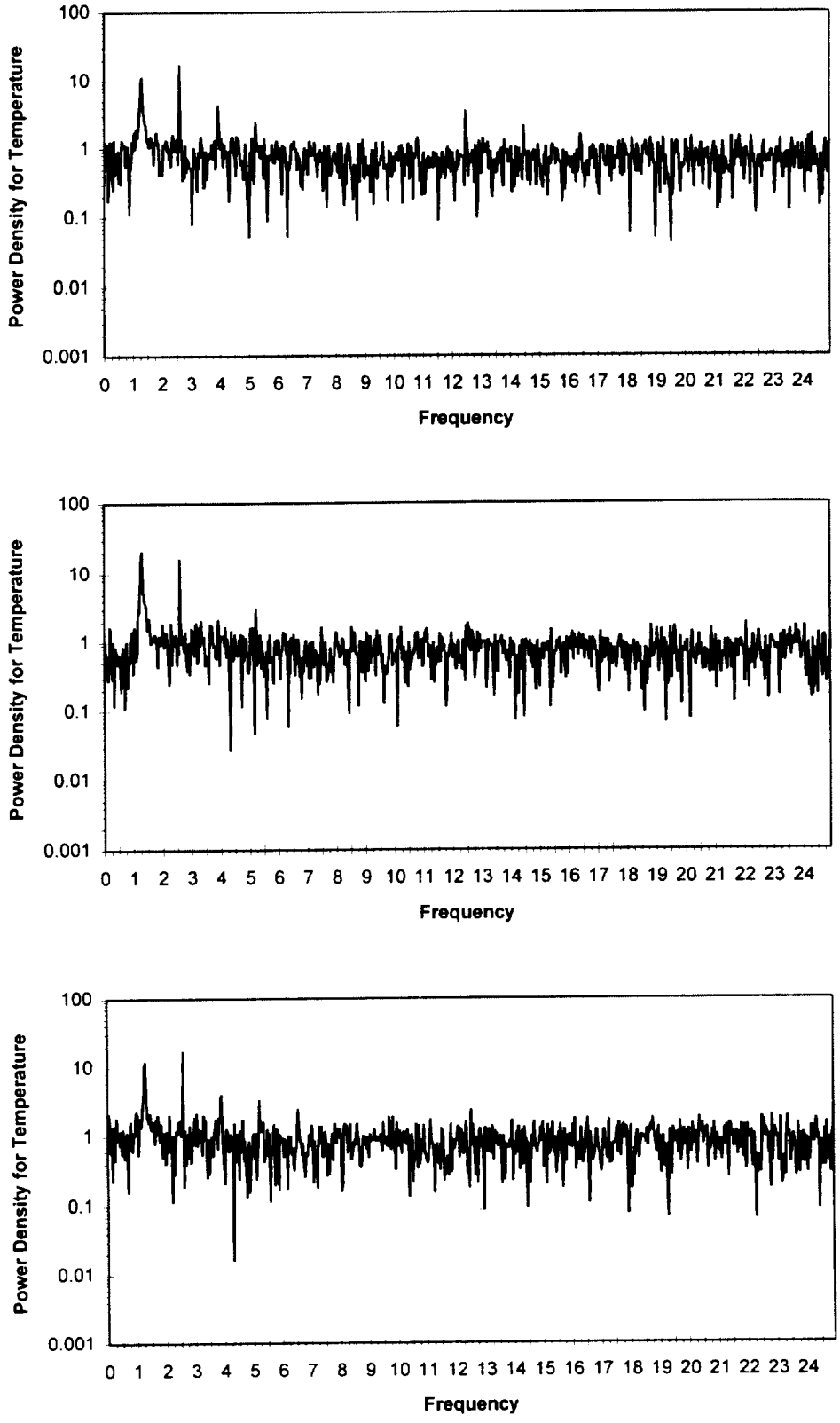

Power Spectrums for the Third Observed Oscillation of the Diameter 1.0, Aspect Ratio 2.0, Bond Number 23.5 Case

3. Power Spectra for the 1.2 cm Diameter Test Chamber

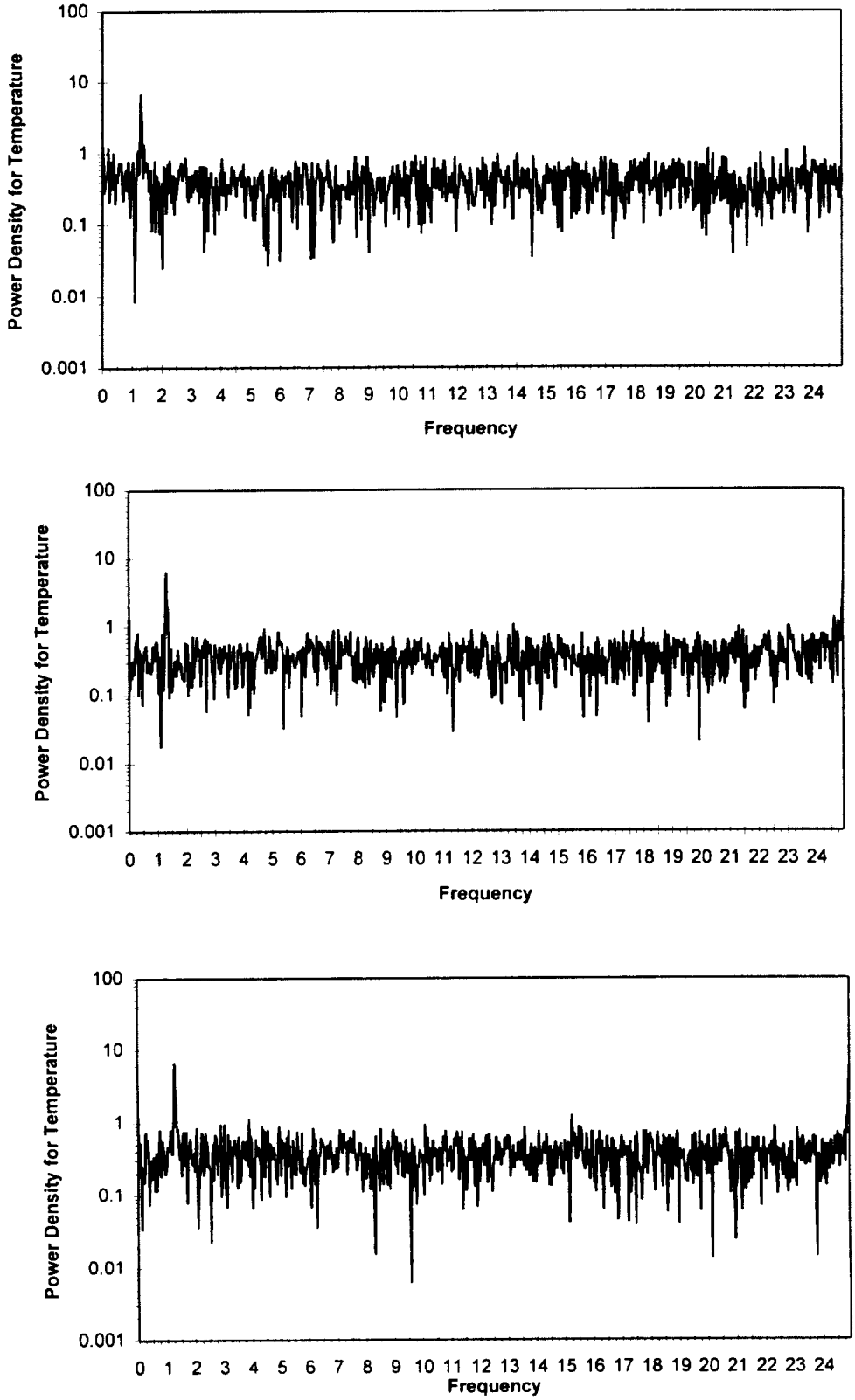

Power Spectrums for the Second Observed Oscillation of the Diameter 1.2, Aspect Ratio 0.5, Bond Number 0.53 Case

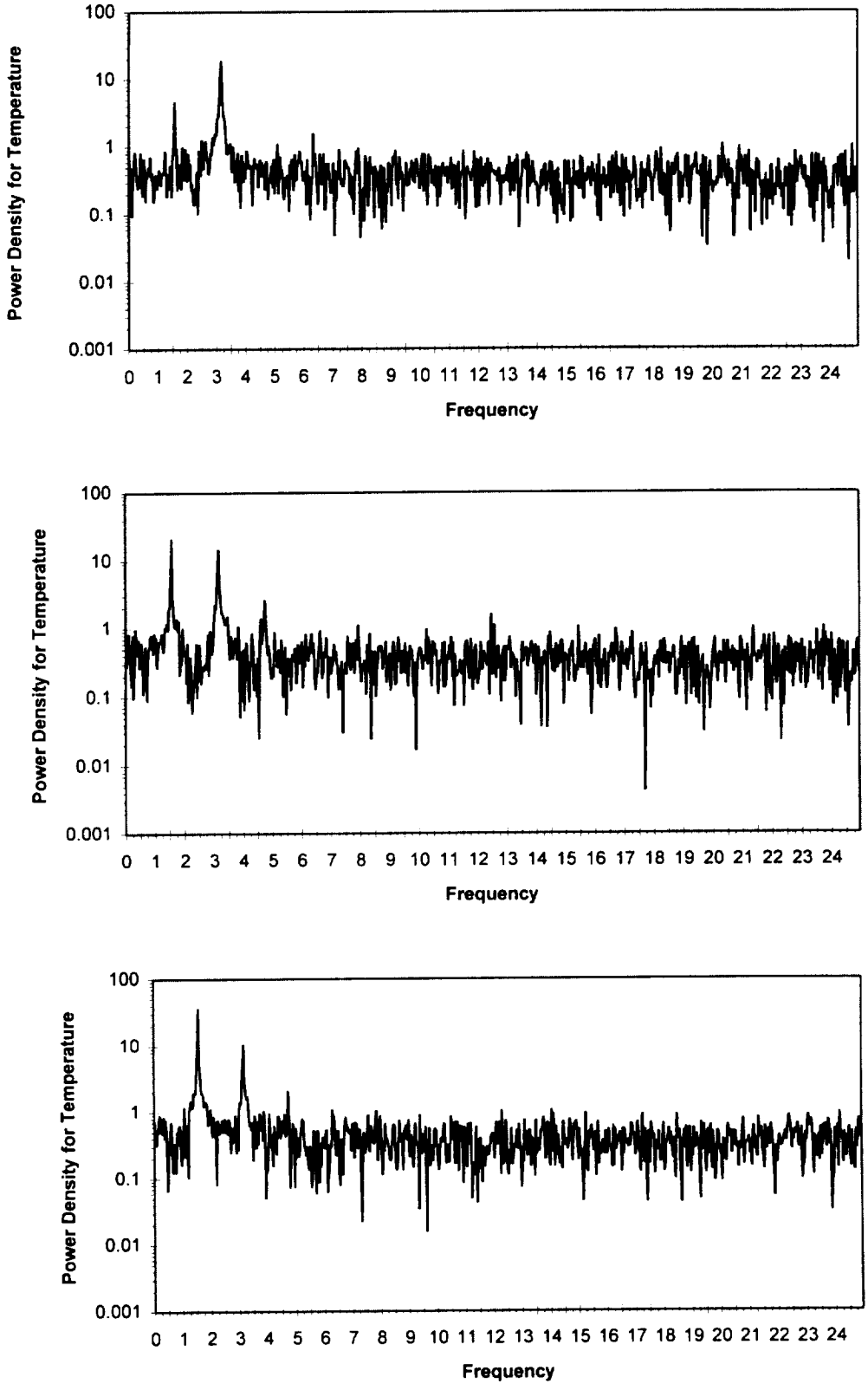

Power Spectrums for the Third Observed Oscillation of the Diameter 1.2, Aspect Ratio 0.5, Bond Number 0.53 Case

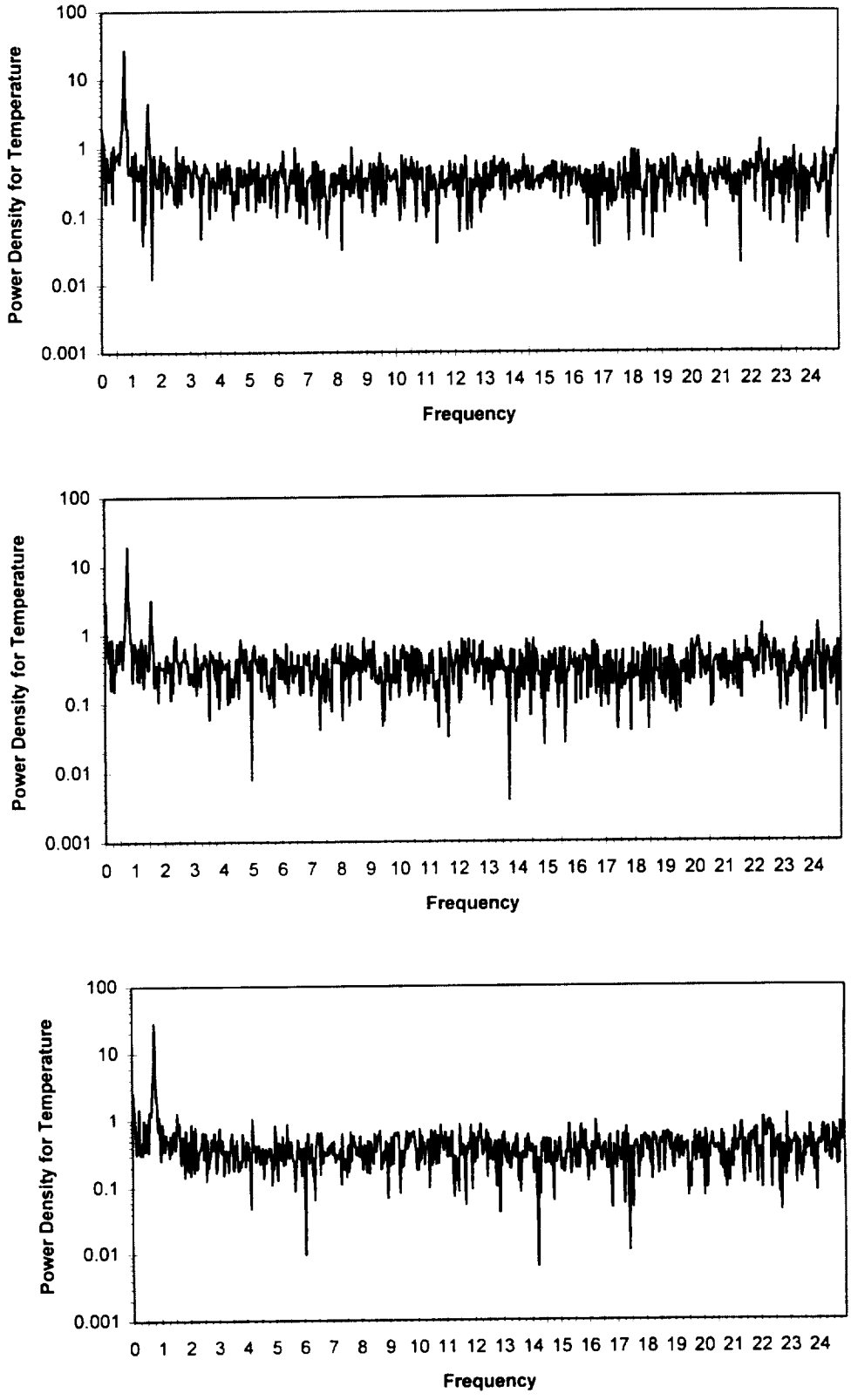

Power Spectrums for the Second Observed Oscillation of the Diameter 1.2, Aspect Ratio 1.0, Bond Number 4.23 Case

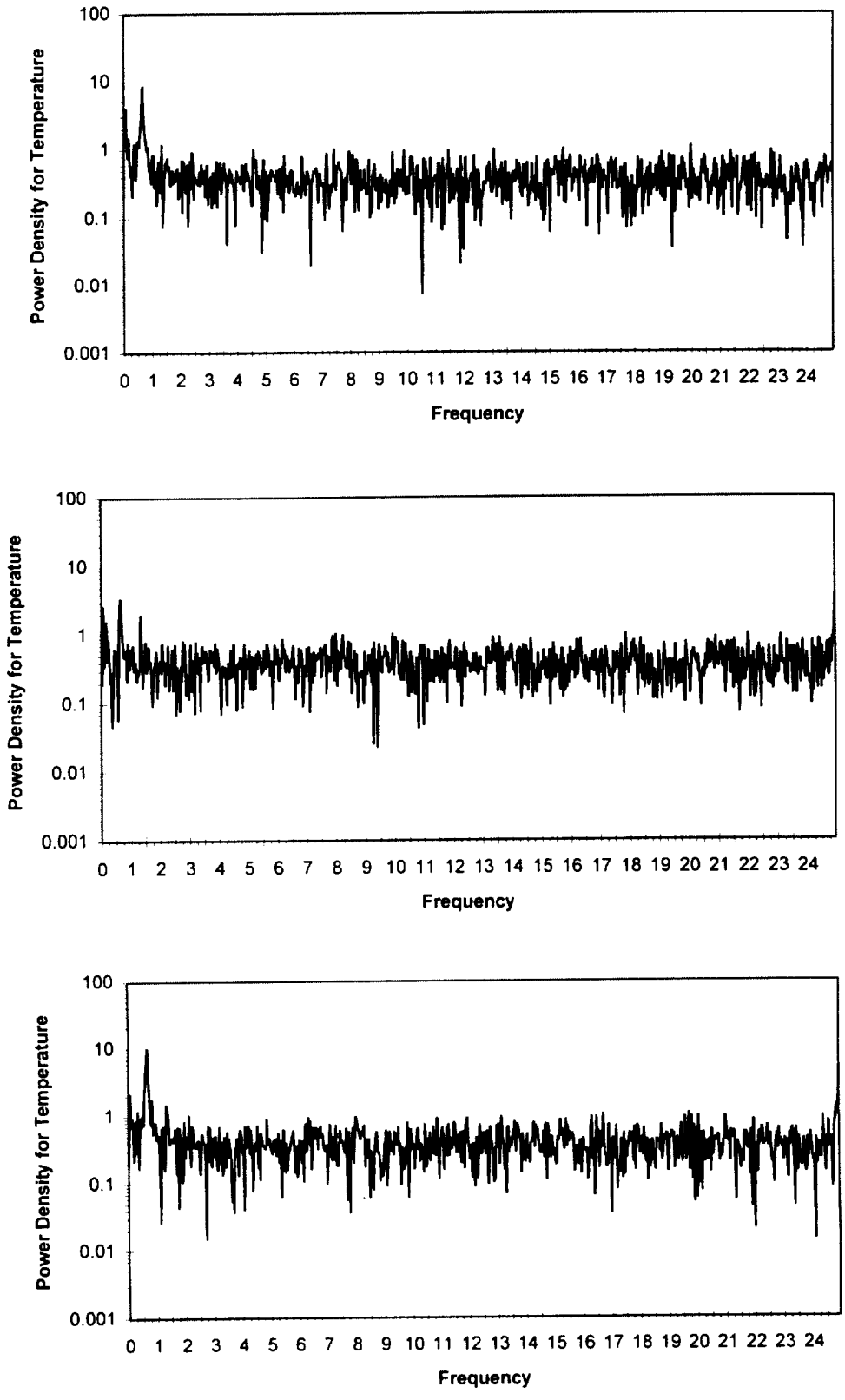

Power Spectrums for the Second Observed Oscillation of the Diameter 1.2, Aspect Ratio 1.5, Bond Number 14.3 Case

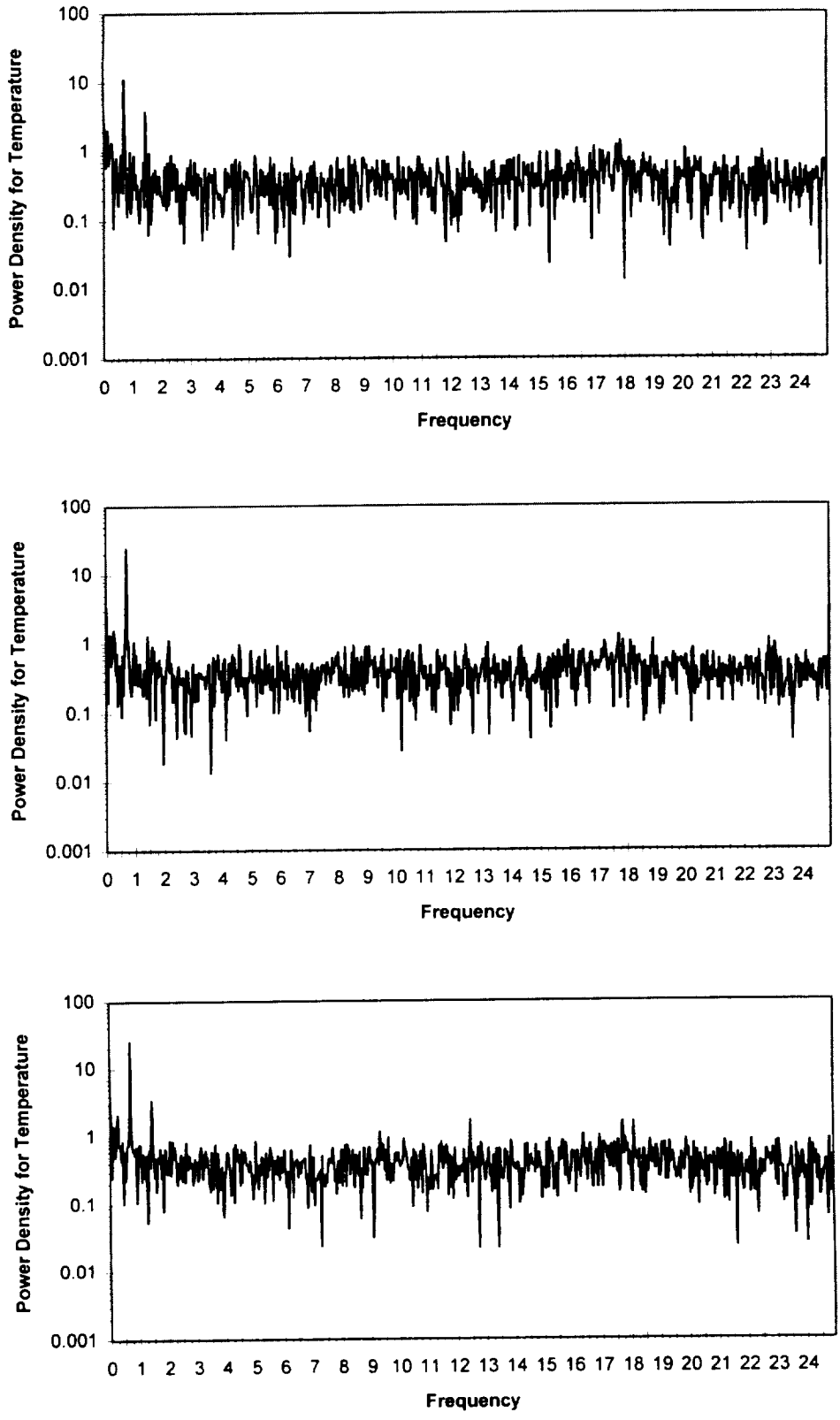

Power Spectrums for the Third Observed Oscillation of the Diameter 1.2, Aspect Ratio 1.5, Bond Number 14.3 Case

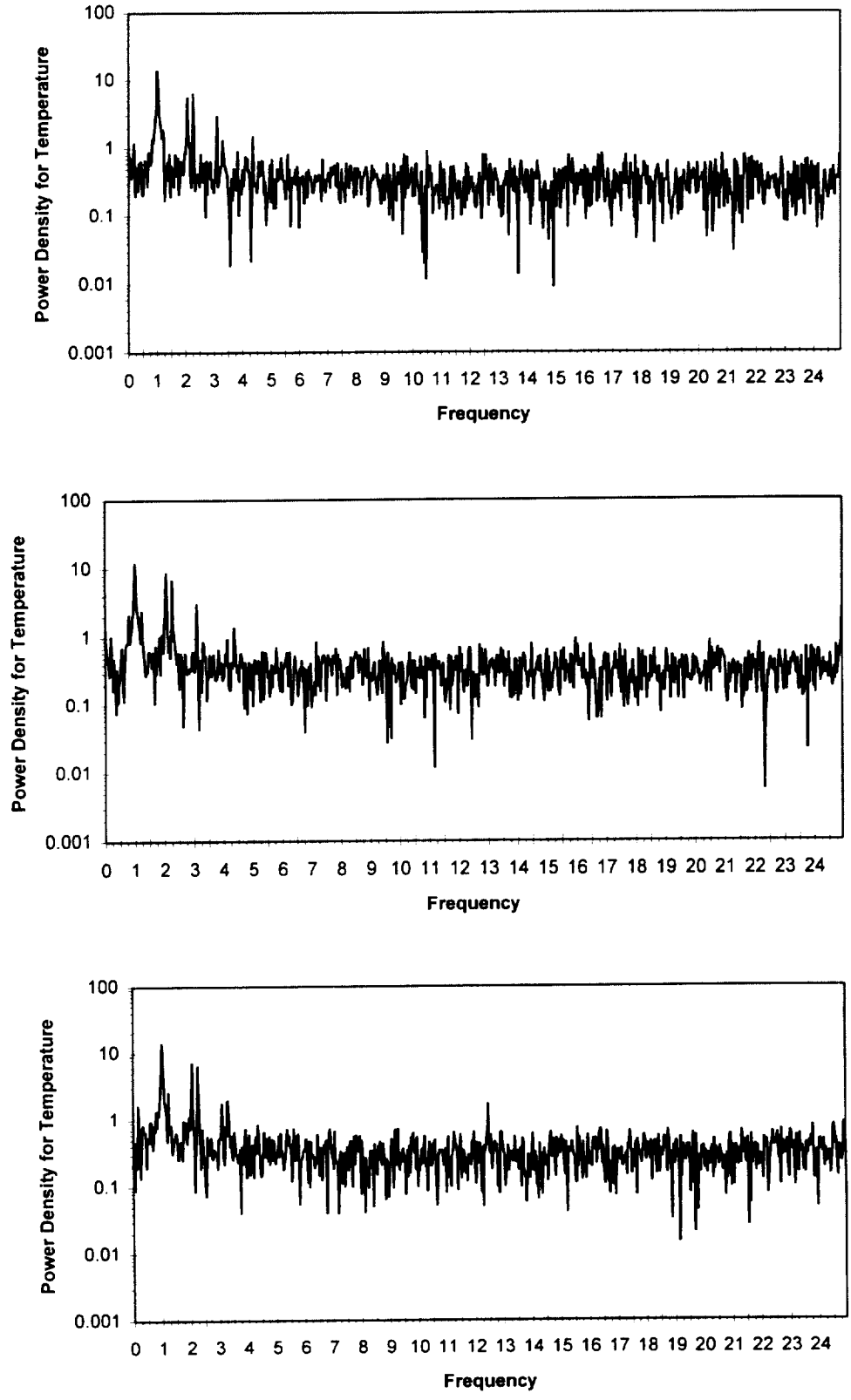

Power Spectrums for the Fourth Observed Oscillation of the Diameter 1.2, Aspect Ratio 1.5, Bond Number 14.3 Case

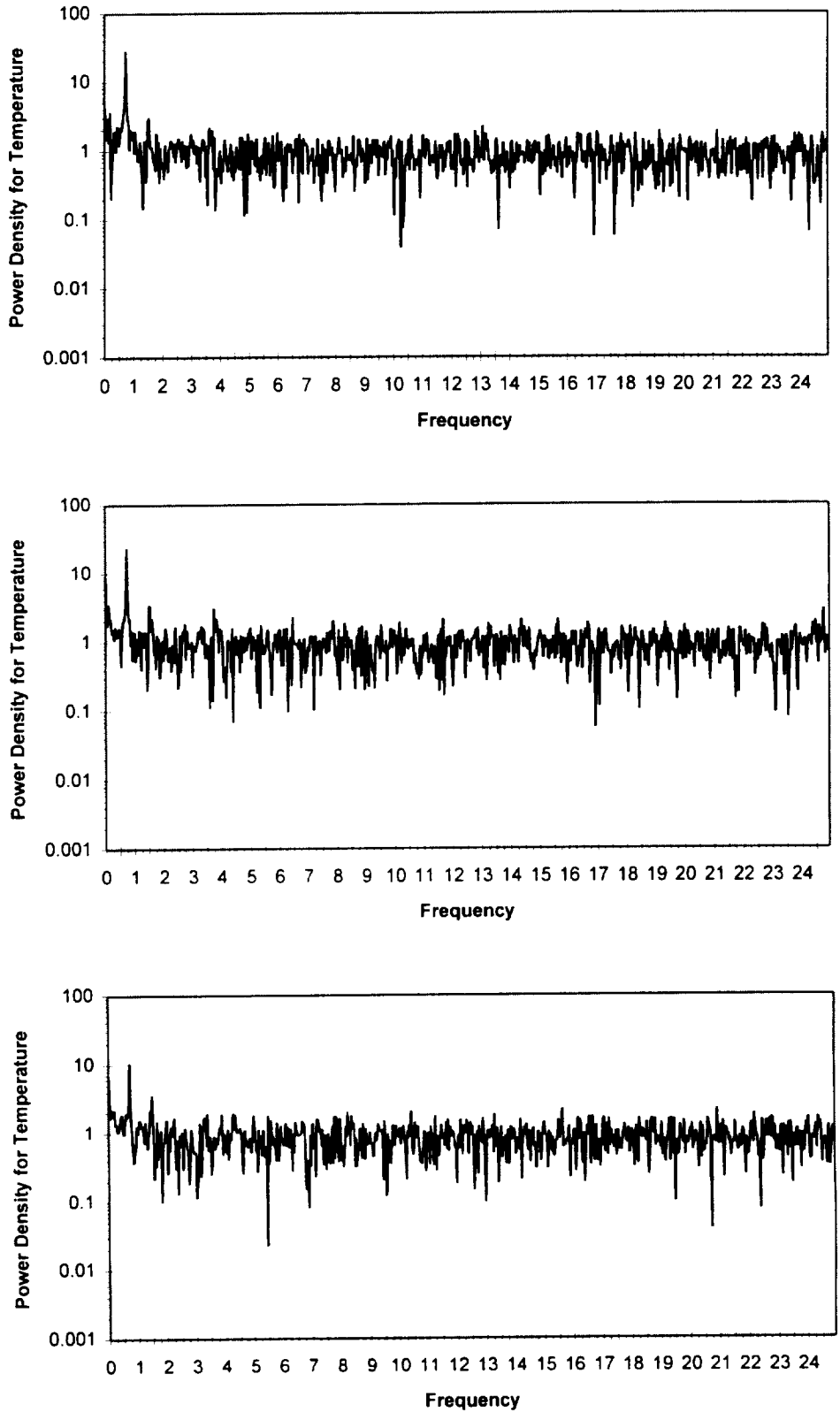

Power Spectrums for the Second Observed Oscillation of the Diameter 1.2, Aspect Ratio 2.0, Bond Number 33.9 Case

4. Power Spectra for the 2.0 cm Diameter Test Chamber

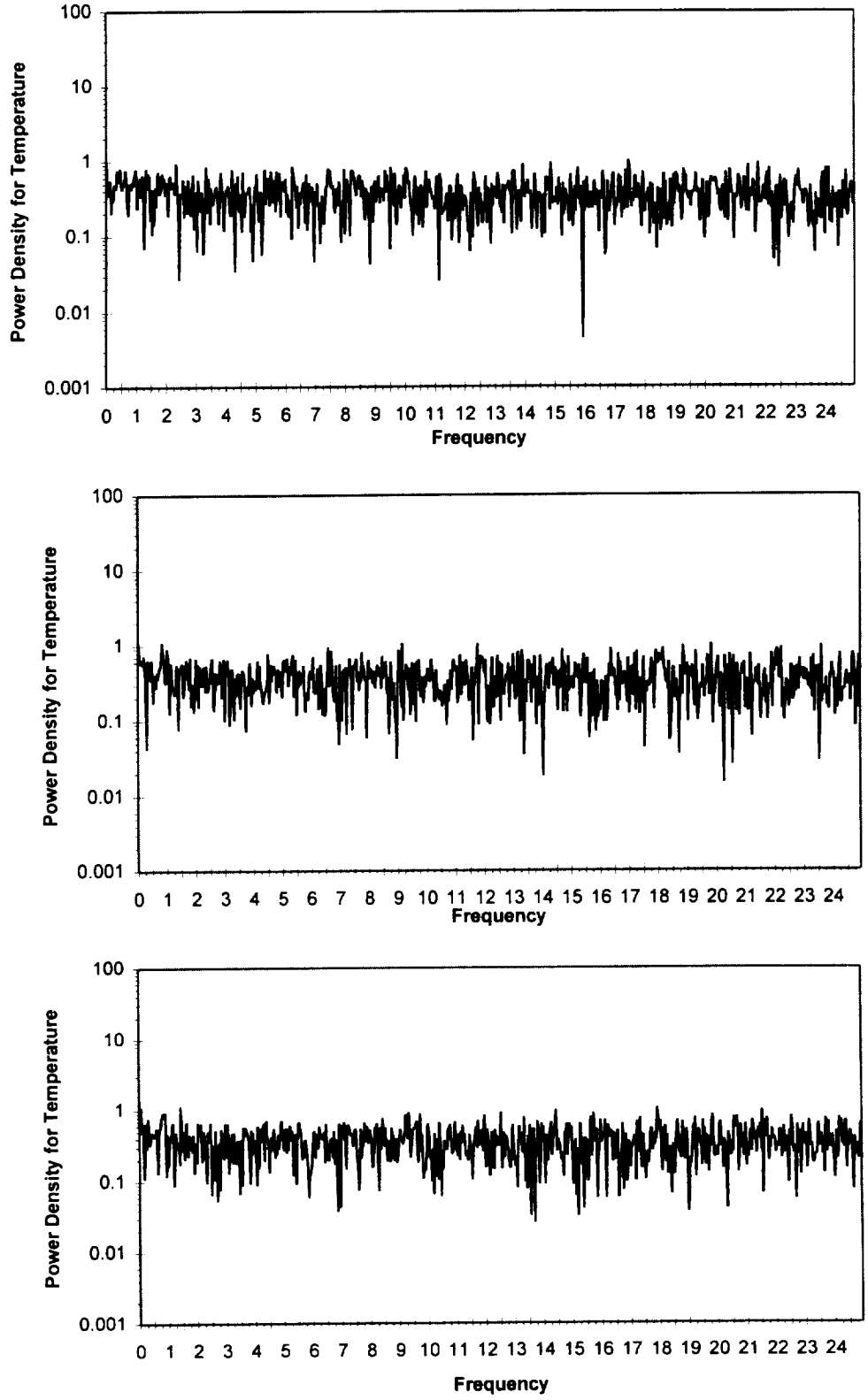

Power Spectrums for the Second Observed Oscillation of the Diameter 2.0, Aspect Ratio 0.5, Bond Number 1.47 Case

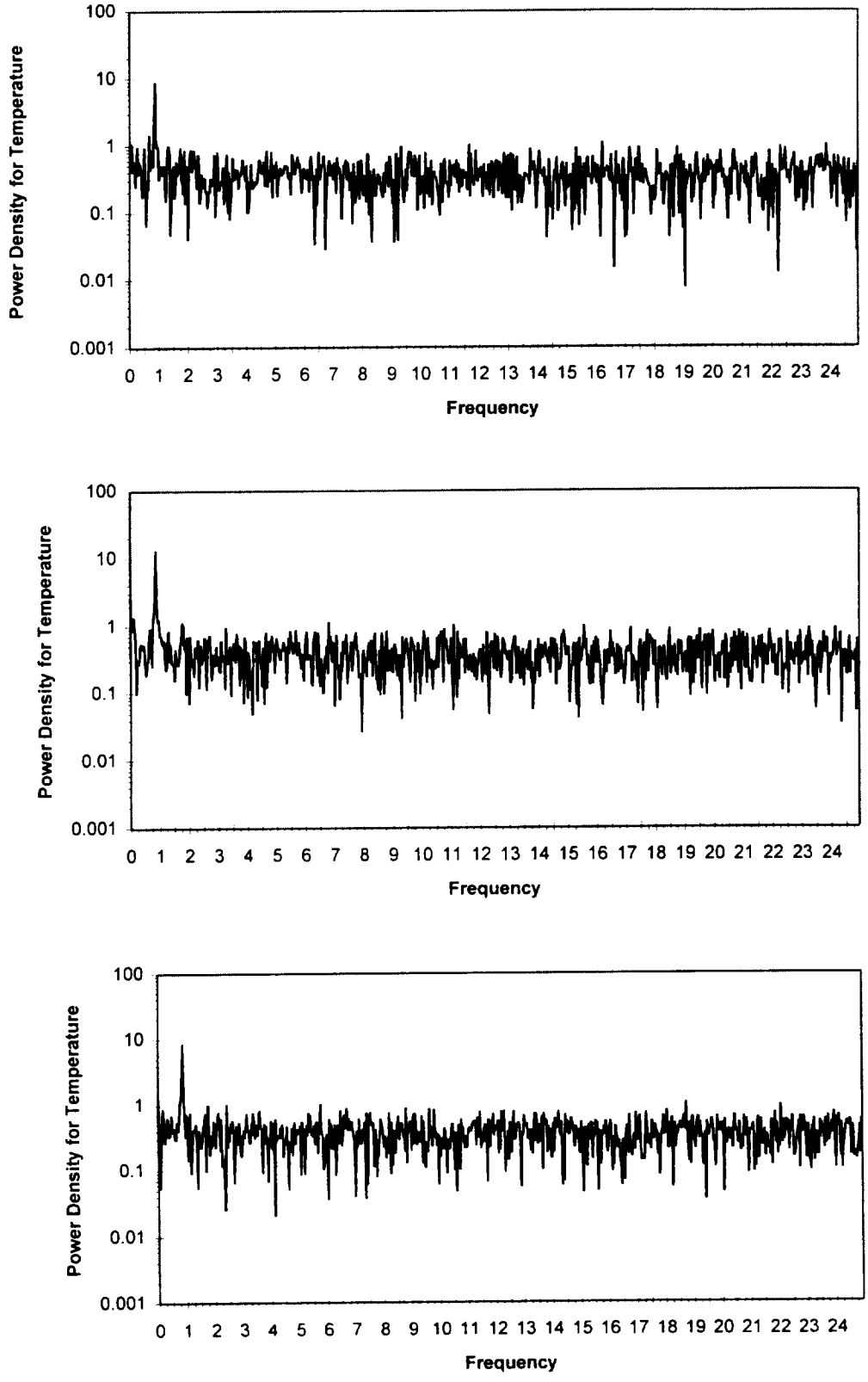

Power Spectrums for the Third Observed Oscillation of the Diameter 2.0, Aspect Ratio 0.5, Bond Number 1.47 Case

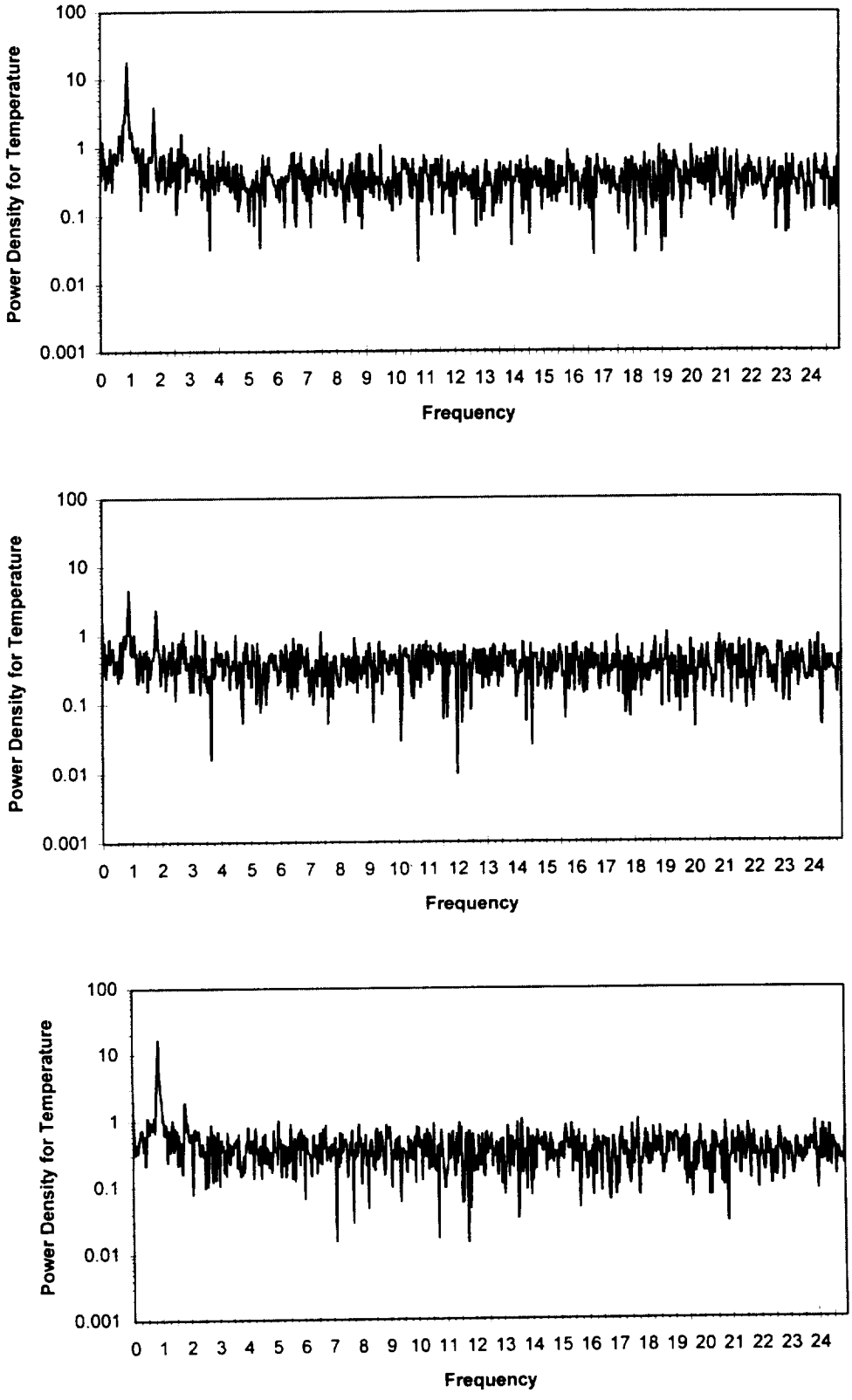

Power Spectrums for the Fourth Observed Oscillation of the Diameter 2.0, Aspect Ratio 0.5, Bond Number 1.47 Case

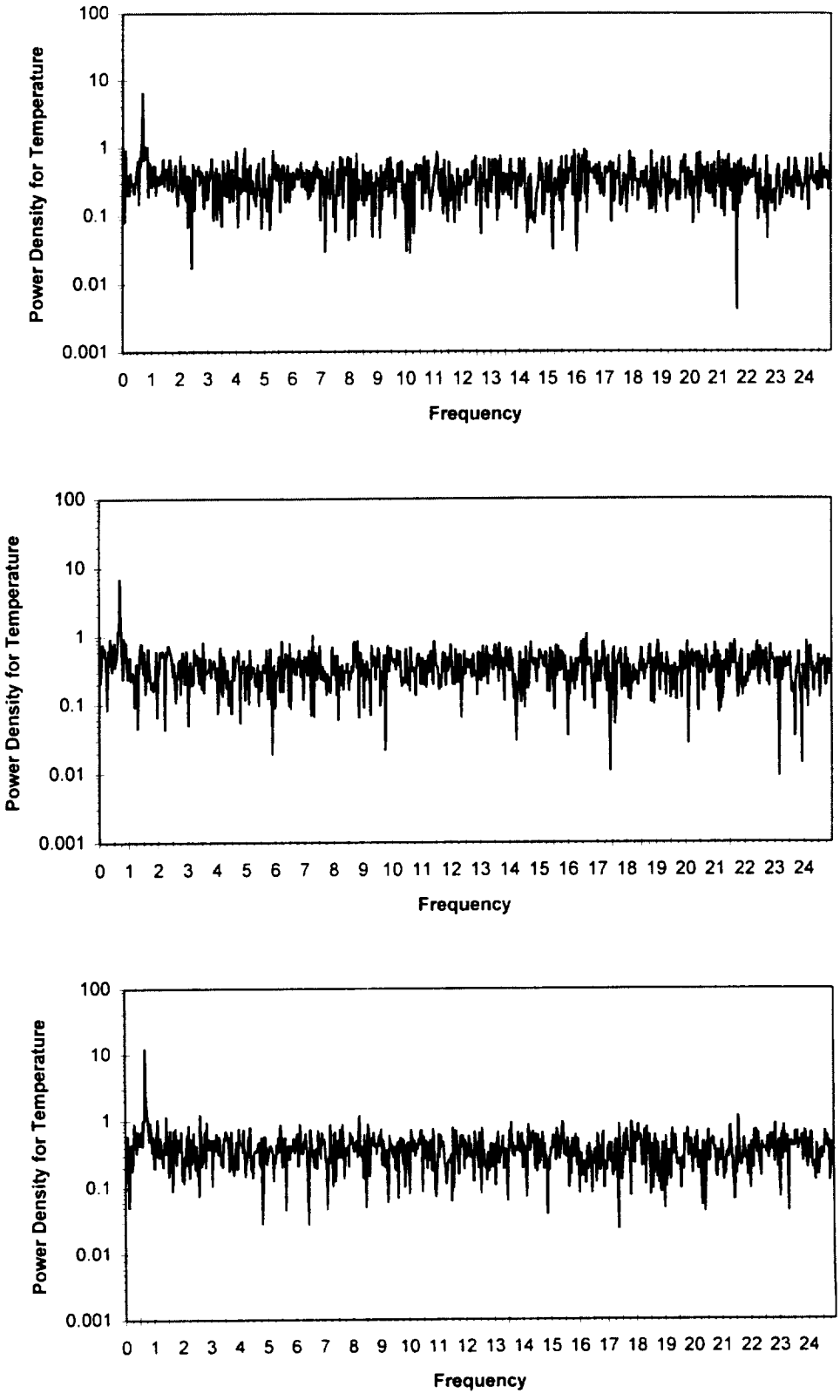

Power Spectrums for the Second Observed Oscillation of the Diameter 2.0, Aspect Ratio 1.0, Bond Number 11.8 Case

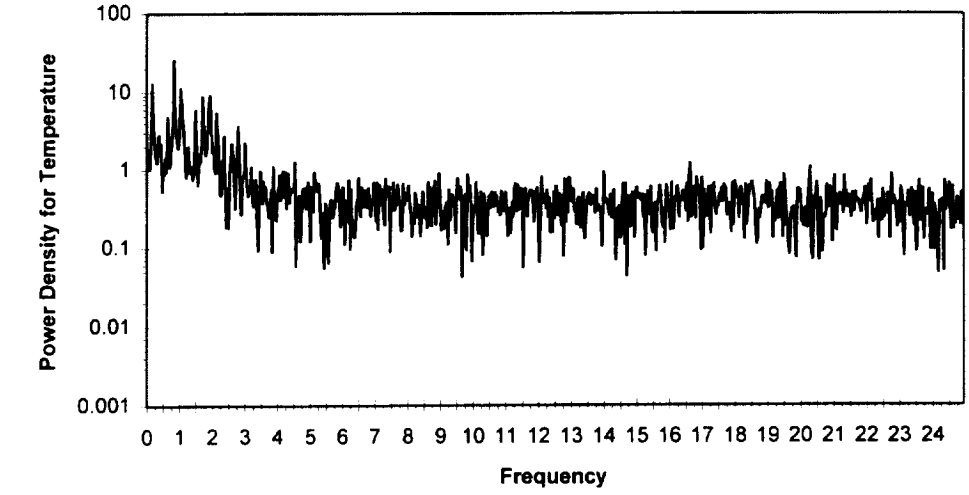

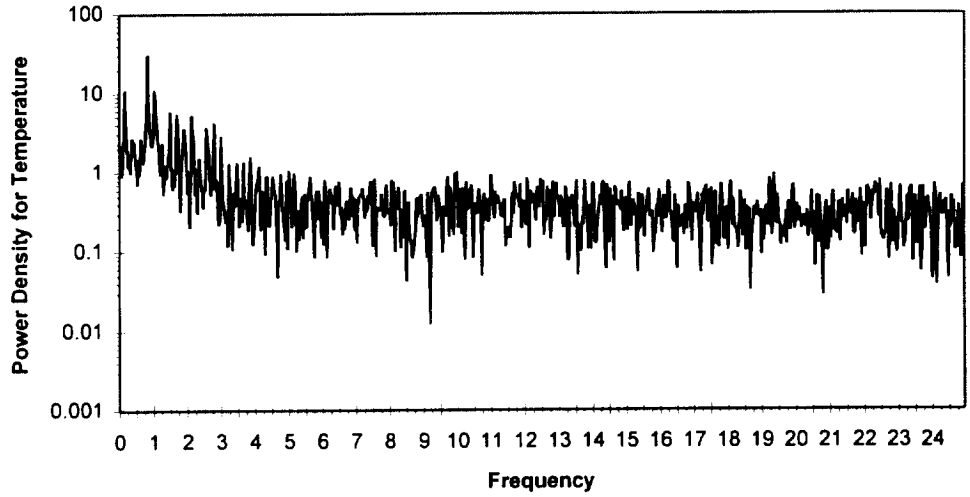

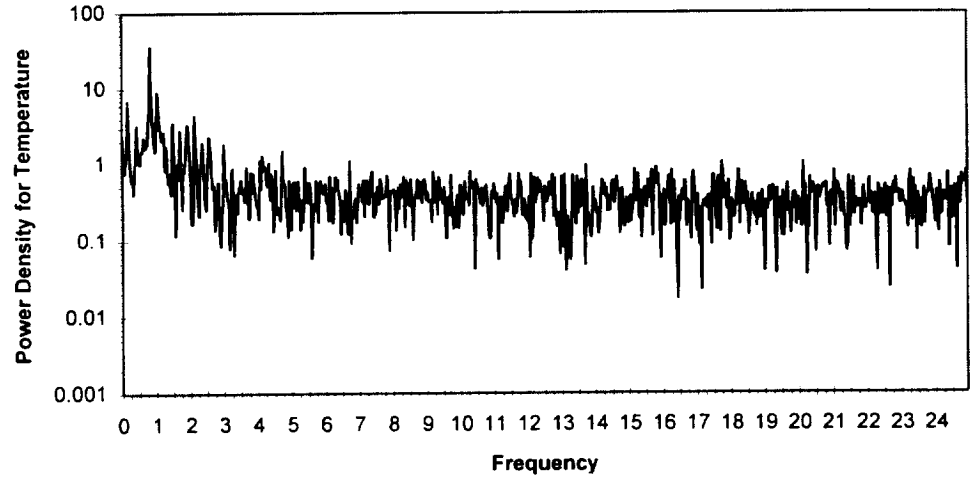

Power Spectrums for the Third Observed Oscillation of the Diameter 2.0, Aspect Ratio 1.0, Bond Number 11.8 Case

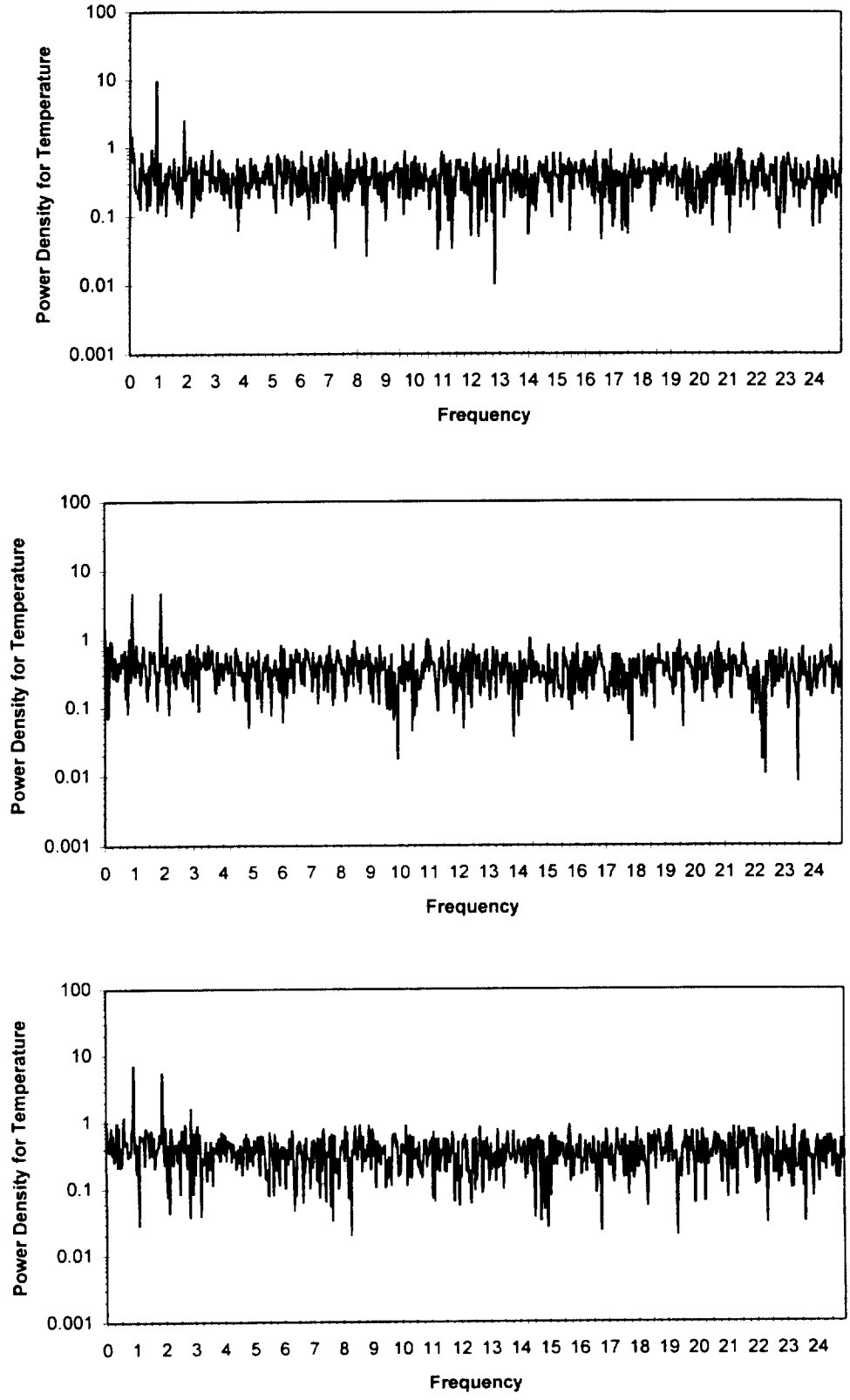

Power Spectrums for the Second Observed Oscillation of the Diameter 2.0, Aspect Ratio 1.5, Bond Number 39.7 Case

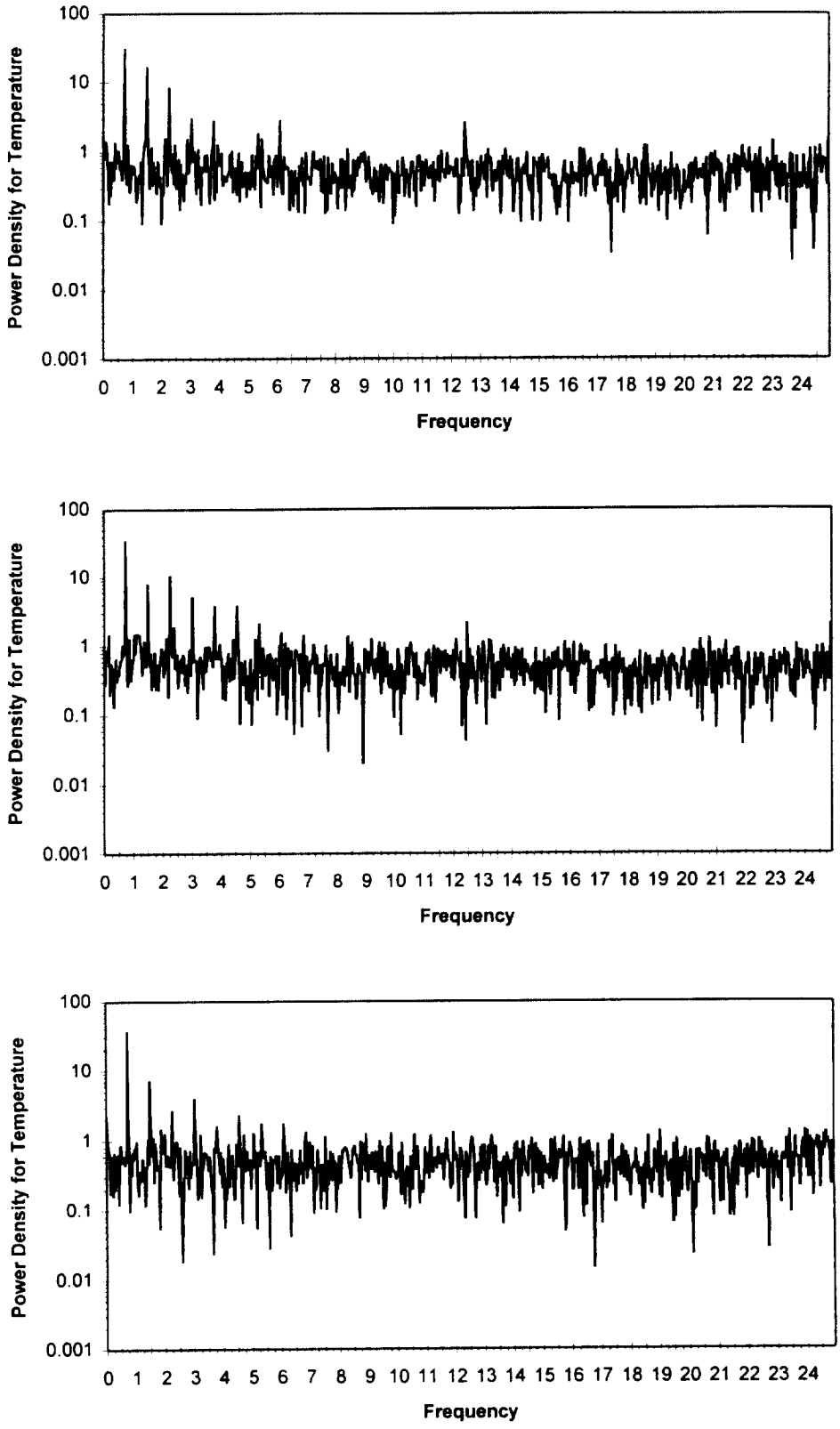

Power Spectrums for the Second Observed Oscillation of the Diameter 2.0, Aspect Ratio 2.0, Bond Number 94.1 Case

5. Power Spectra for the 3.0 cm Diameter Test Chamber

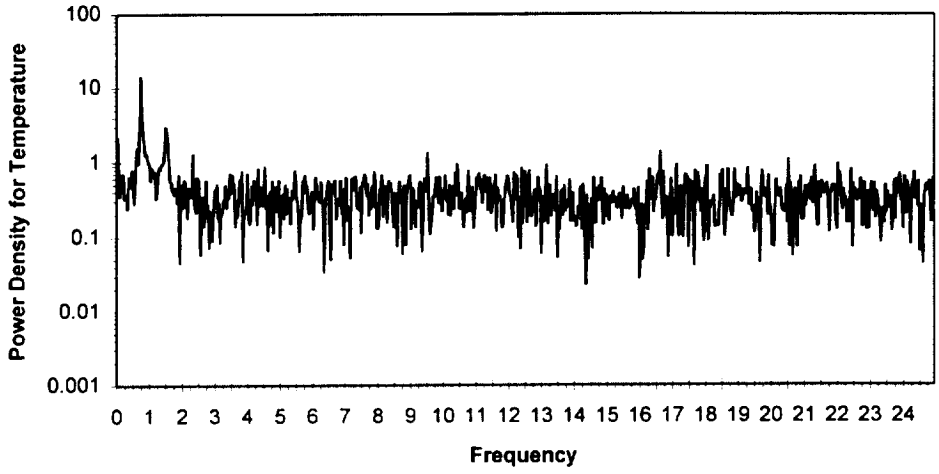

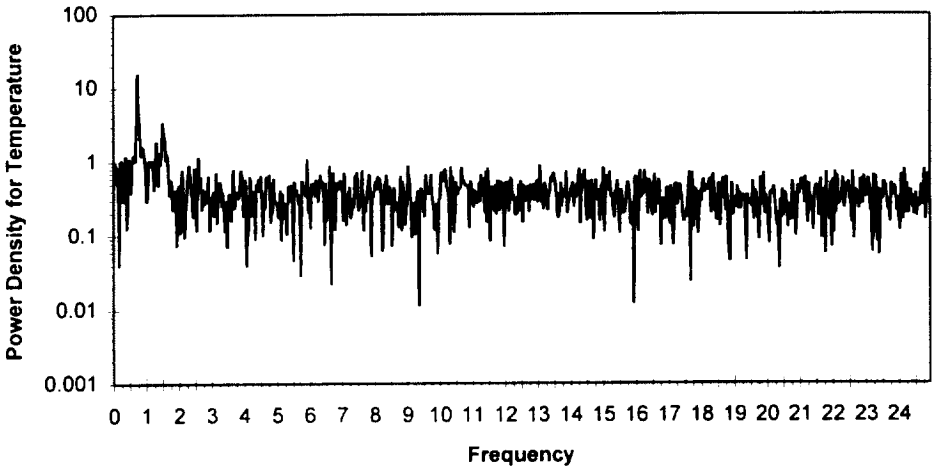

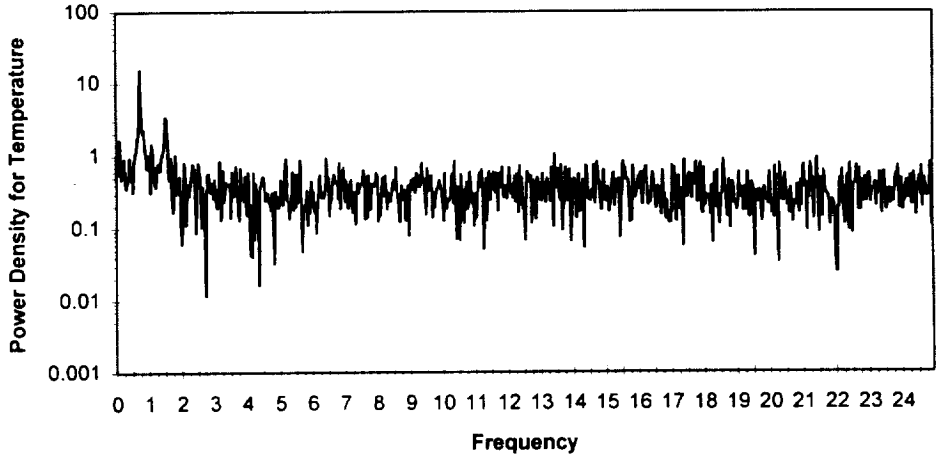

Power Spectrums for the Second Observed Oscillation of the Diameter 3.0, Aspect Ratio 1.0, Bond Number 26.5 Case

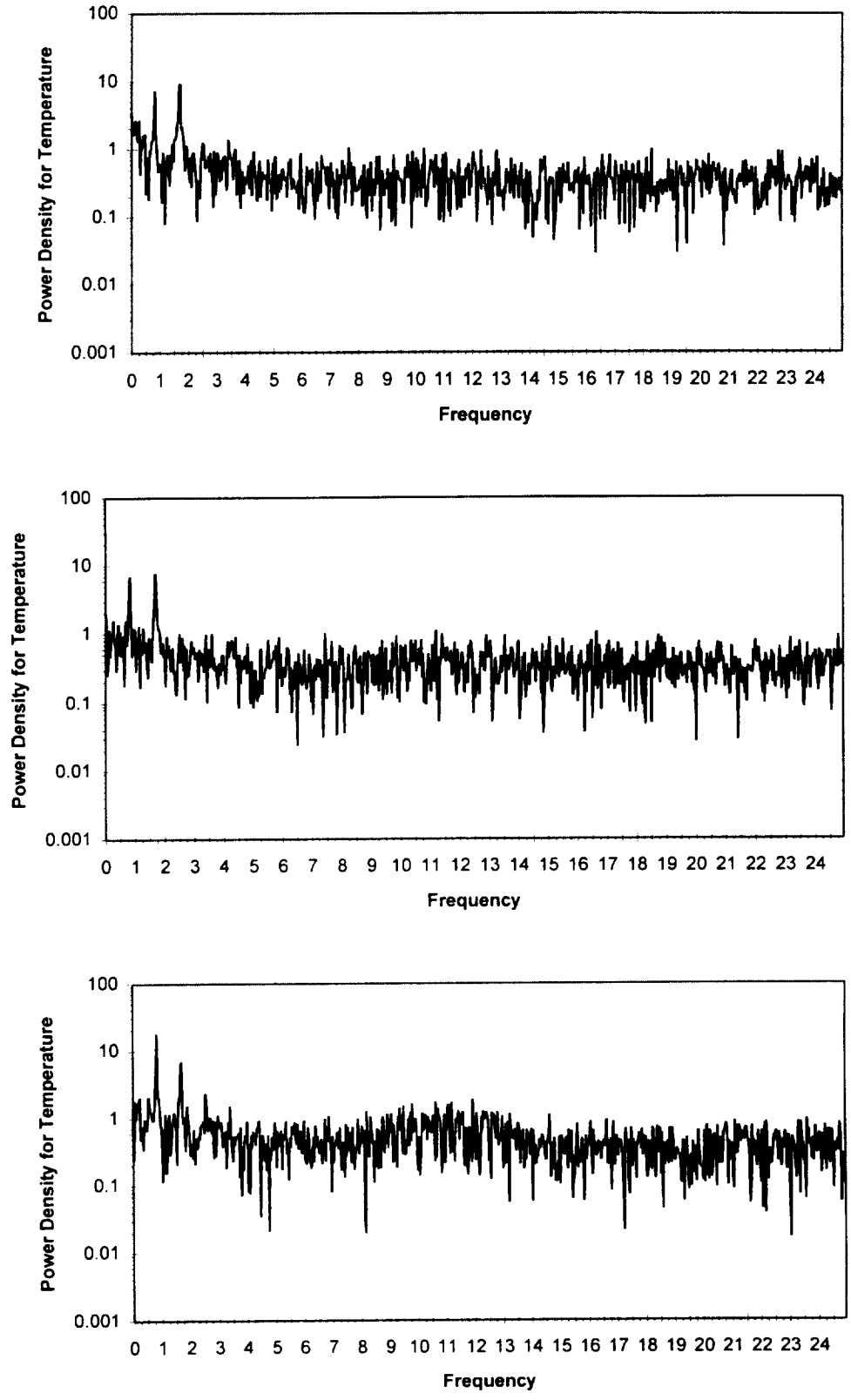

Power Spectrums for the Third Observed Oscillation of the Diameter 3.0, Aspect Ratio 1.0, Bond Number 26.5 Case

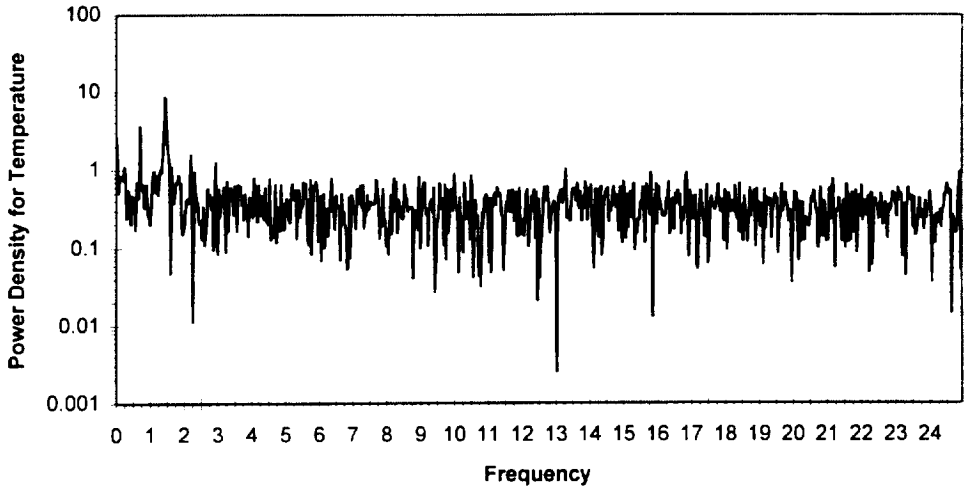

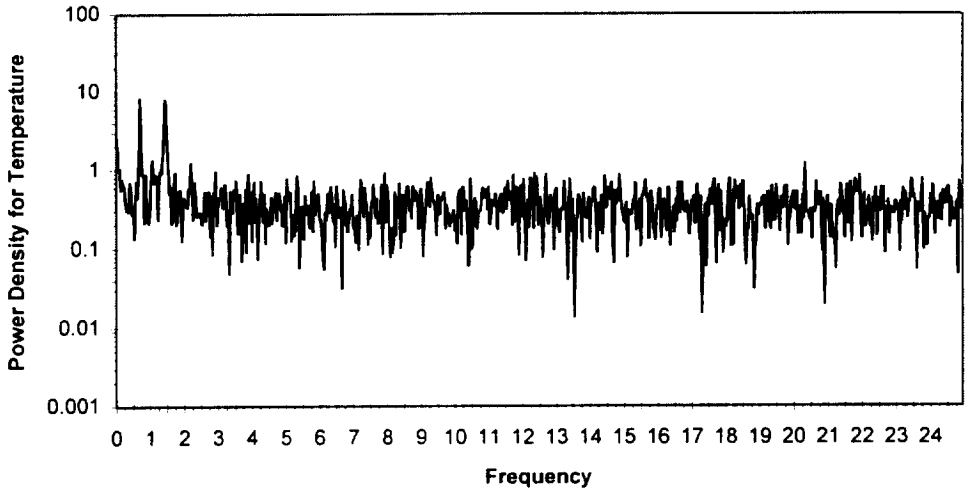

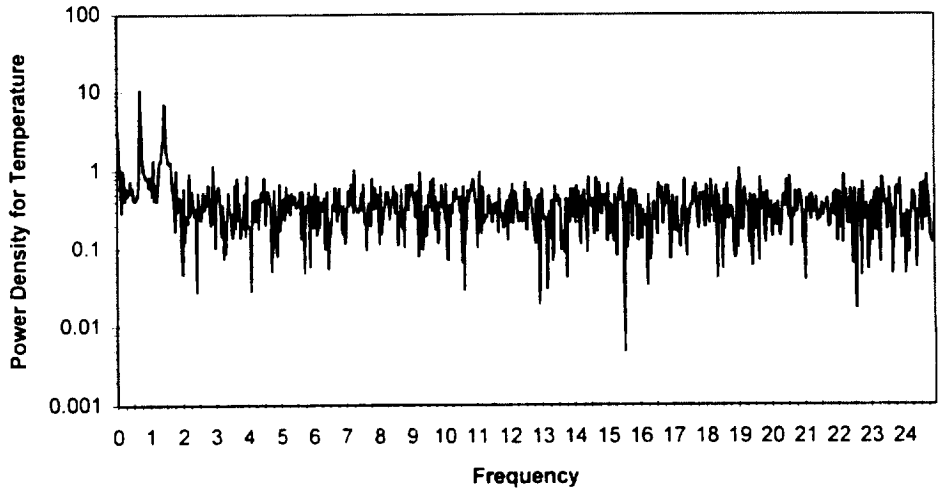

Power Spectrums for the Second Observed Oscillation of the Diameter 3.0, Aspect Ratio 1.5, Bond Number 89.3 Case

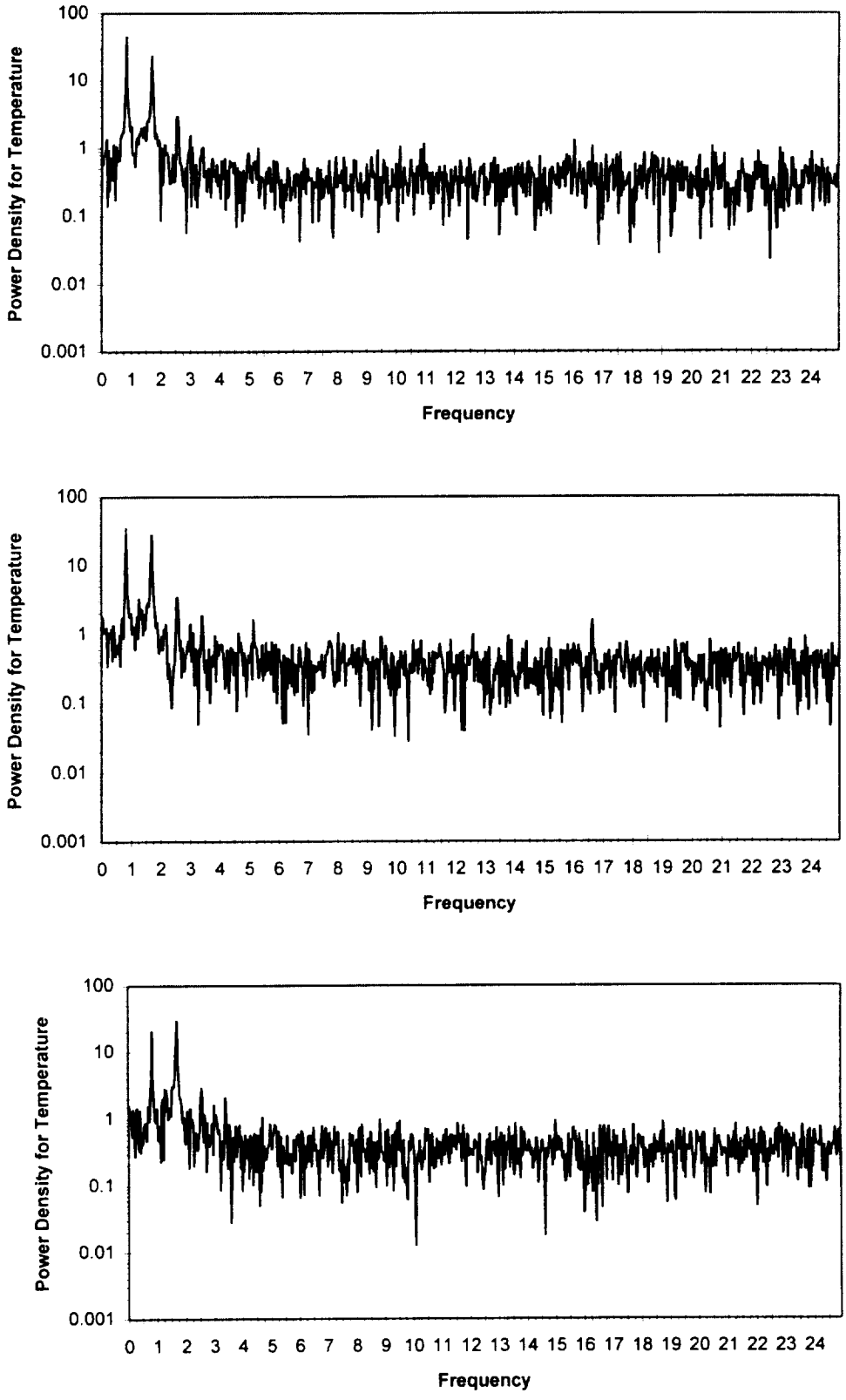

Power Spectrums for the Third Observed Oscillation of the Diameter 3.0, Aspect Ratio 1.5, Bond Number 89.3 Case

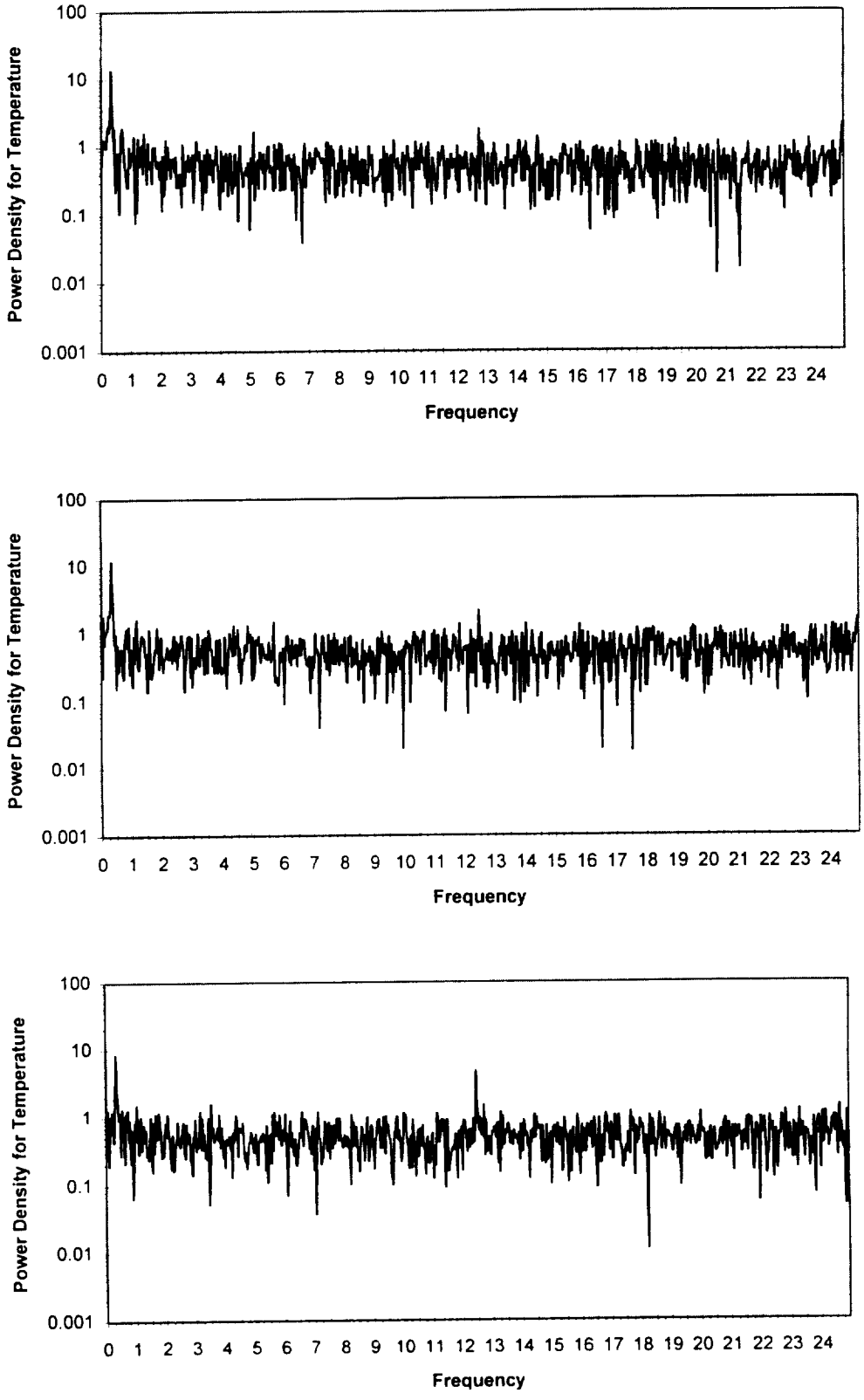

Power Spectrums for the Second Observed Oscillation of the Diameter 3.0, Aspect Ratio 2.0, Bond Number 211.7 Case

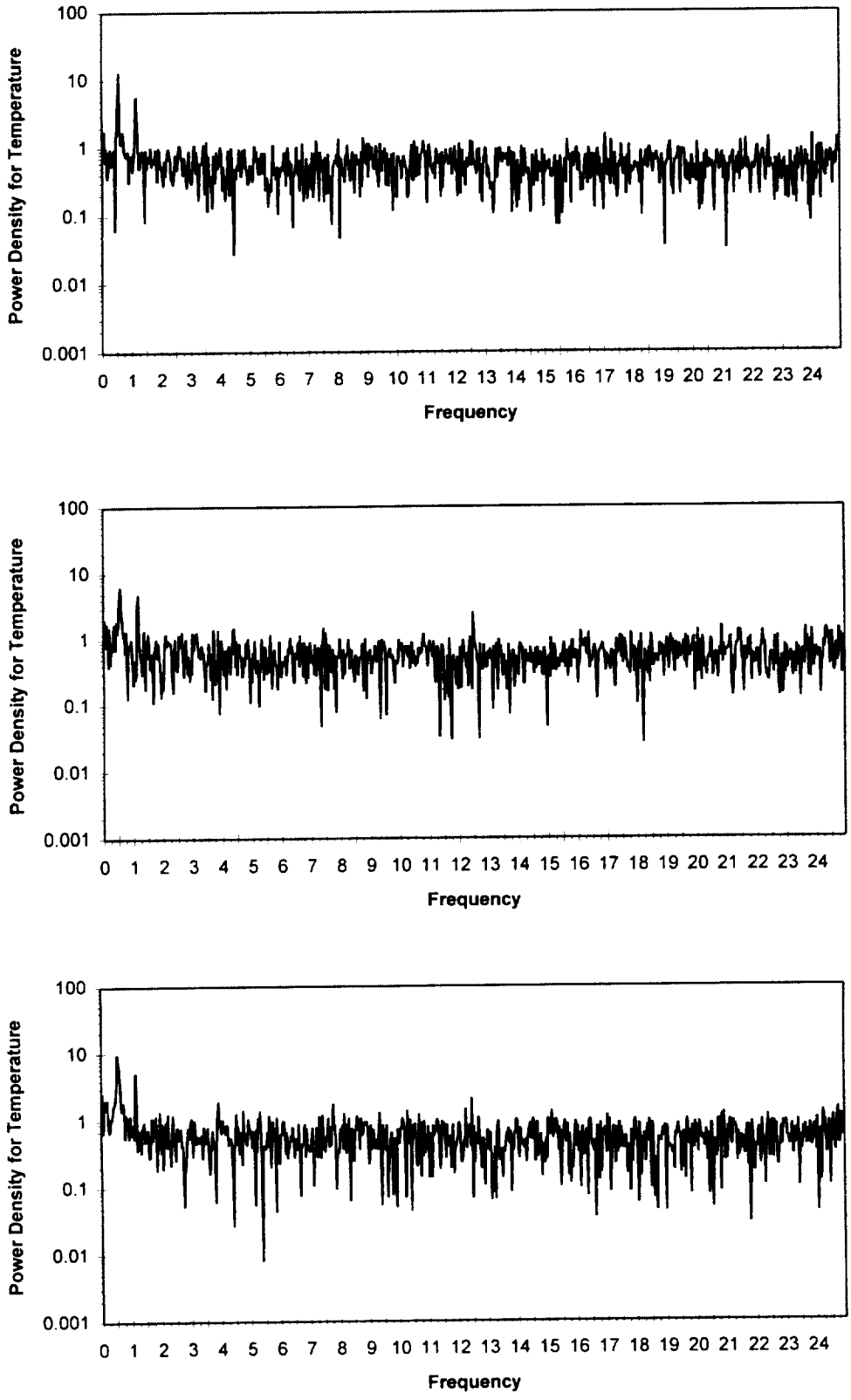

Power Spectrums for the Third Observed Oscillation of the Diameter 3.0, Aspect Ratio 2.0, Bond Number 211.7 Case